Titre: Title:	Study of aerodynamics of cooling in film blowing
Auteur: Author:	Zhijie Zhang
Date:	2007
Type:	Mémoire ou thèse / Dissertation or Thesis
Référence: Citation:	Zhang, Z. (2007). Study of aerodynamics of cooling in film blowing [Thèse de doctorat, École Polytechnique de Montréal]. PolyPublie. https://publications.polymtl.ca/8002/

UNIVERSITÉ DE MONTRÉAL

STUDY OF AERODYNAMICS OF COOLING IN FILM BLOWING

Zhijie ZHANG

DÉPARTMENT DE GÉNIE CHIMIQUE
ÉCOLE POLYTECHNIQUE DE MONTRÉAL

THÈSE PRÉSENTÉE EN VUE DE L'OBTENTION
DU DIPLÔME DE PHILOSOPHIAE DOCTOR
(GÉNIE CHIMIQUE)
OCTOBRE 2007

Library and Archives Canada

Published Heritage Branch

395 Wellington Street
Ottawa ON K1A 0N4
Canada

Bibliothèque et Archives Canada

Direction du Patrimoine de l'édition

395, rue Wellington
Ottawa ON K1A 0N4
Canada

Your file Votre référence
ISBN: 978-0-494-37141-1
Our file Notre référence
ISBN: 978-0-494-37141-1

UNIVERSITÉ DE MONTRÉAL

ÉCOLE POLYTECHNIQUE DE MONTRÉAL

Cette thèse intitulée:

STUDY OF AERODYNAMICS OF COOLING IN FILM BLOWING

présentée par: ZHANG Zhijie

en vue l'obtention du diplôme de: Philosophiae Doctor

a été dûment acceptée par le jury d'examen constitué de:

M. BERTRAND François, Ph.D., président

M. LAFLEUR Pierre G., Ph.D., membre et directeur de recherche

M. DUBOIS Charles, Ph.D., membre

M. VLACHOPOULOS John, Ph.D., membre

ACKNOWLEDGEMENTS

My sincere appreciation and thanks to my director, Professor Pierre Lafleur for showing me how to be thorough and independent, and for his knowledge, guidance, experience, and financial support. I would also like to express my deep thanks to Professor Francois Bertrand for providing me with helpful counsel and contribution to this work.

I would like to thank all my fellow graduate students for their support and friendship. My special thanks to the staff of the department of chemical engineering at ÉCOLE POLYTECHNIQUE DE MONTRÉAL for their understanding and cooperation during my several years in the department. I also thank Karen Stoeffler, a Ph.D. candidate, for her help in translating the 'resume' and 'condense' in French. I am indebted to my Chinese friends, Wei Li, Gang Li, Yunli Fang and Jianhong Zhang for their encouragement, useful suggestions and help.

I would like to express my sincerest appreciation to my parents and sisters for their love, support and encouragement. Finally, I wish to express my many thanks to my husband, Cheng Xing for his love, care, passion, understanding and patience.

RÉSUMÉ

Le présent travail concerne la simulation numérique et expérimentale du refroidissement à l'air dans le procédé de film gonflé. Le refroidissement à l'air est en effet un processus complexe, dont dépend la productivité de la ligne de production, et qui affecte de plus la stabilité et la forme de la bulle. Ultimement, l'étape de refroidissement affecte donc le taux de production et les propriétés finales du film.

Une technique de dynamique des fluides computationnelle (DFC), mettant en œuvre un groupe de renormalisation (RNG) modèle k-ε, est utilisée avec le logiciel FLUENT pour analyser numériquement l'aérodynamique autour de l'anneau de refroidissement dans le procédé de film gonflé. Un système de caméras en ligne développé dans notre laboratoire est utilisé pour étudier expérimentalement les instabilités dynamiques de la bulle.

Les résultats, qui permettent de comparer les caractéristiques et la performance du flux produit par des anneaux de refroidissement à une ou deux lèvres, suggèrent que le design de l'anneau de refroidissement affecte directement le transfert de chaleur, et détermine de nombreuses conditions frontières liées à l'efficacité de refroidissement. Une fenêtre d'opération pour le coefficient de transfert de chaleur et la vitesse maximale de l'air a été établie. Les relations entre l'inertie thermique et l'aérodynamique du refroidissement ont été explorées pour différentes géométries de bulles. L'effet du nombre de Reynolds sur le taux de transfert de chaleur dans la solution numérique est aussi reporté.

Une bonne corrélation entre la stabilité de la bulle et la pression interne a été obtenue. La combinaison des mesures expérimentales et des solutions numériques a indiqué que différents taux de refroidissement induisent d'importantes variations de la stabilité de la bulle pour différents taux de gonflement (BUR : blow-up ratio) et

d'étirement (TUR : take-up ratio). Une augmentation du taux de refroidissement peut déstabiliser les bulles de faible BUR, mais stabilise au contraire les bulles de haut BUR en raison de la forme différente des bulles produites. La stabilité de la bulle dépend de la distribution de pression statique le long de sa surface, et la minimisation du gradient de pression engendre une stabilisation. Les bulles à haut TUR soutiennent plus de force due à l'aérodynamique agissant sur la surface de la bulle, résultant dans une fenêtre d'opération plus large.

Finalement, une simulation numérique utilisant un groupe de renormalisation k-ε et le logiciel FLUENT a été effectuée pour analyser l'effet du mouvement et du transfert de chaleur de l'air de refroidissement au film polymère sur les instabilités de la bulle.

ABSTRACT

The present work involves an experimental study coupled with numerical simulation of air cooling dynamics in the film blowing process. The blown film cooling is a very complex process. It does not only limit achieving higher productivity, but also affects the stability and shape of the bubble in film blowing production lines. Ultimately, the cooling process affects both the production rate and the final film properties.

A Computational Fluid Dynamics (CFD) technique using a ReNormalization Group (RNG) k-ε model and FLUENT software was employed to analyze numerically the aerodynamics in the air-ring cooling system of a film blowing process. An in-line scanning camera system developed in our lab was used to study experimentally the detailed dynamics of bubble instabilities.

The results, obtained by comparing the characteristics and performance of flow produced by both single- and dual lip air-rings; suggest that the air-ring design directly affects the heat transfer rate. Furthermore, various boundary conditions led by the air flow rate were shown to be equally important for the cooling efficiency. An operation window for the heat transfer coefficient and the maximum air velocity function was established in this study. The relationship between thermal inertia and cooling air aerodynamics for different bubble geometries was also explored. The effect of Reynolds number on the heat transfer rate was numerically obtained and reported.

A good correlation between the bubble instability and the pressure inside the bubble was obtained. A combination of the experimental results and numerical simulations indicated that various cooling rates resulted in important variations in the dynamics of bubble instabilities for different Blow-Up-Ratios and Take-Up-Ratios, respectively. Increasing the cooling rate can destabilize the low BUR bubbles, but

stabilize the high BUR ones due to the formation of different bubble shapes. It was found that bubble instabilities depend on the static pressure distribution along the bubble surface, and that minimizing the pressure gradient can stabilize the bubbles. Bubbles with the high TURs were found to sustain greater force due to the aerodynamics on the bubble surface. This broadens the stable window of operation.

Finally, a numerical simulation was performed to analyze the effects of momentum and heat transfer from the cooling air to the polymer film on bubble instabilities.

CONDENSÉ EN FRANÇAIS

Le procédé de film gonflé est une technologie flexible utilisée pour la production de masse de films polymères minces. Dans plusieurs lignes de production de film gonflé, le flux d'air de refroidissement limite la productivité. De plus, il affecte la stabilité et la forme de la bulle fondue, ainsi que la morphologie du film final. Ultimement, le processus de refroidissement affecte donc à la fois le taux de production et les propriétés finales du film. Bien que de nombreuses études numériques et expérimentales aient été menées pour étudier les jets d'air produits par l'anneau de refroidissement, les effets de l'aérodynamique restent mal compris en raison de la complexité des processus impliqués, de difficultés dans la mesure expérimentale des variables d'intérêt, et du manque de données fiables utilisées dans les études numériques. Le présent travail concerne la méthodologie qui peut être utilisée pour acquérir une meilleure compréhension et pour valider le système de refroidissement de la bulle dans le procédé de film gonflé.

Dans cette thèse, une méthode de dynamique des fluides computationnelle (CFD), impliquant un groupe de renormalisation (RNG) modèle k-ε couplé avec un traitement des parois amélioré, est utilisée avec le logiciel FLUENT pour analyser numériquement l'aérodynamique autour de l'anneau de refroidissement du procédé de film gonflé. La sensibilité à la taille du maillage a été testée dans chaque simulation. La validation du modèle a été effectuée en comparant les résultats numériques et expérimentaux de la vitesse maximale de l'air de refroidissement autour de la surface de la bulle. La variation des coefficients de transfert de chaleur, de la vitesse et de la distribution de pression statique le long de la surface de la bulle, ainsi que le profil du flux de l'air de refroidissement a été examiné en fonction des conditions du procédé telles que le taux de gonflement (BUR : blow-up ratio), le taux d'étirement (TUR : take-up ratio), la forme de la bulle et le débit de l'air de refroidissement.

L'analyse des simulations, pour l'aérodynamique de l'air de refroidissement externe produit par un anneau de refroidissement à deux lèvres, et l'effet du montage opératoire sur l'efficacité de refroidissement, suggère que différentes formes de bulles obtenues à un même BUR induisent des différences significatives sur le profil d'écoulement de l'air et sur le coefficient de transfert de chaleur. Pour les bulles à long cou, le coefficient de transfert de chaleur est plus grand à l'intérieur de l'anneau de refroidissement et plus petit en dehors de cet anneau, en raison de l'effet Venturi. La région de recirculation réduit le taux de transfert de chaleur et est responsable de la présence d'une valeur maximale sur les profils de coefficient de transfert de chaleur. Une fenêtre d'opération pour le coefficient de transfert de chaleur et la vitesse maximum de l'air a été établie. Les résultats des simulations montrent que cette fonction est valide principalement à faible BUR et en dehors de l'anneau de refroidissement.

Les résultats, par l'intermédiaire d'une comparaison entre les caractéristiques et la performance du flux produit par des anneaux de refroidissement à une ou deux lèvres, suggèrent que le design de l'anneau de refroidissement a un impact important. Alors qu'un anneau à deux lèvres répand le transfert de chaleur sur une large surface de la bulle, un anneau à une lèvre concentre son action à l'intérieur de l'anneau : en conséquence, la majeure partie de la déformation du film à lieu a température réduite. Les prédictions numériques montrent aussi que les conditions frontières imposées par différents débits d'air ont une influence significative sur le taux de transfert de chaleur. Le flux du jet de refroidissement sur la surface de la bulle se déplace en aval en fonction de la variation du nombre de Reynolds. Le nombre de Nusselt dans l'anneau de refroidissement dépend de Re^n, la corrélation étant indépendante du BUR et des paramètres de l'anneau. Cette corrélation simple pourrait permettre d'améliorer le design de filière en prédisant le flux et le transfert de chaleur dans l'anneau de refroidissement.

Un système de caméras en ligne a été développé dans notre laboratoire afin d'étudier les différents types d'instabilité de la bulle dans le procédé de film gonflé. Une analyse détaillée de la dynamique de chaque type d'instabilité de la bulle a été menée en fonction du temps et des différentes conditions de procédé. De plus, un manomètre situé sur la filière a été utilisé pour enregistrer a pression interne de la bulle correspondant à la variation du rayon lors des oscillations de la bulle.

Les observations expérimentales ont permis de vérifier que la pression interne de la bulle peut fournir un avertissement quant à l'instabilité du procédé. Les signaux d'avertissement dépendent du BUR de la bulle. Les variations périodiques du diamètre de la bulle analysées en utilisant la caméra vidéo correspondent aux perturbations de pression pour un BUR de 1, les amplitudes des deux modes d'oscillation doivent être réduites à un minimum afin d'avoir une bulle stable. Cependant, la pression interne moyenne minimale avec la variation de rayon minimale indique que la bulle stable apparaît pour un BUR supérieur à 1. De ce fait, une bonne corrélation entre l'instabilité de la bulle et la pression interne a été obtenue.

Les résultats, dans lesquels les instabilités de la bulle ont été capturés quantitativement, montrent que le taux de refroidissement est l'un des paramètres qui affecte le plus les instabilités de la bulle. Augmenter le taux de refroidissement peut déstabiliser les bulles de faible BUR, mais stabilise les bulles de fort BUR en raison de la forme différente de la bulle. Différentes formes de bulle, produites à différents taux de refroidissement, ont montré d'importantes différences dans la dynamiques des instabilités de la bulle pour un BUR constant. Les bulles à haut TUR ont soutenu plus de force en raison de l'aérodynamique agissant sur la surface de la bulle, résultant dans une fenêtre d'opération plus large d'un point de vue de la stabilité.

La combinaison des mesures expérimentales et des simulations numériques ont indiqué que les forces aérodynamiques jouent un rôle dominant sur la dynamique des instabilités de la bulle. Les instabilités de la bulle dépendent de la distribution de pression statique le long de la surface de la bulle, et la minimisation du gradient de pression peut stabiliser les bulles.

Dans le présent travail, le fait bien connu qu'il existe un équilibre entre les forces aérodynamiques agissant sur le transfert de chaleur et les instabilités de la bulle est également vérifié, puisque les gains dans un domaine réduisent l'efficacité des autres domaines. Les résultats présentés illustrent la complexité des mécanismes de refroidissement de la bulle et donnent des explications partielles sur le fait qu'augmenter le débit du produit ne peut pas être réalisé par une simple accélération du flux de l'air de refroidissement.

TABLE OF CONTENTS

LIST OF TABLES

LIST OF FIGURES

LIST OF APPENDICES

CHAPTER 1

INTRODUCTION

1.1 Description of the Process

The science and technology history of the film blowing process can be traced back to 1915 (Ghaneh-Fard, 1996). Tubular film extrusion is one of the most important polymer processing operations, and has been extensively used for the production of biaxially oriented thin polymeric films. Several polymers are used for film blowing, such as ethylene copolymers, polyvinyl chloride (PVC) and nylon. However, the most widely used materials are polyolefins ranging from low-density polyethylene (LDPE), linear low-density polyethylene (LLDPE), high-density polyethylene (HDPE) and metallocene polyethylene (mPE) to propylene (PP). Only in 2000, the market for polyolefin films represented around 11 of the approximately 49 billion pounds total polyolefin market in United State and Canada (Kamal, 2002). Blown film can be used either in tube form (e.g. for plastic bags and sacks) or the tube can be slit to form a sheet. Typical applications include industrial packaging, consumer packaging, laminating film, barrier film for the packaging of medical products and agricultural film. It is estimated that production and consumption of film will grow at an average annual rate of 6%, resulting in $20.8 billion worth of film produced in Northern America by 2007 (Mooner, 2003). The ever increasing demand for high production rates and high quality films has led to significant developments in materials and equipment, which continue to widen the range of applications and markets for blown film.

Figure 1 shows the schematic of a typical film blowing process. To achieve biaxial stretching, molten polymer extruded through an annular die is inflated along the radial direction, and simultaneously stretched along the axial direction. Air is introduced via a hole in the centre of the die to blow up the tube into a bubble and increase its volume. In most blown film extrusion lines, spiral mandrel dies are used in order to minimize the thickness variations. The tube of film then continues upwards until it passes through nip rollers where the tube is flattened to create what is known as a 'lay-flat' tube of film. The stretching along the axial direction is achieved by controlling the velocity of the nip rollers and the mass flow rate at the die. Radial and axial stretching occurs simultaneously resulting in an increase in the bubble radius and a decrease in the film thickness. The complex dynamics of sustaining such a bubble is accomplished by cooling the polymer melt using turbulent air jets. The temperature of the polymer melt is around 453 – 525 K at the die and it drops by 80-100 K before it reaches the freeze-line. The temperature of the film further drops before it is wound up as lay-flat tubing.

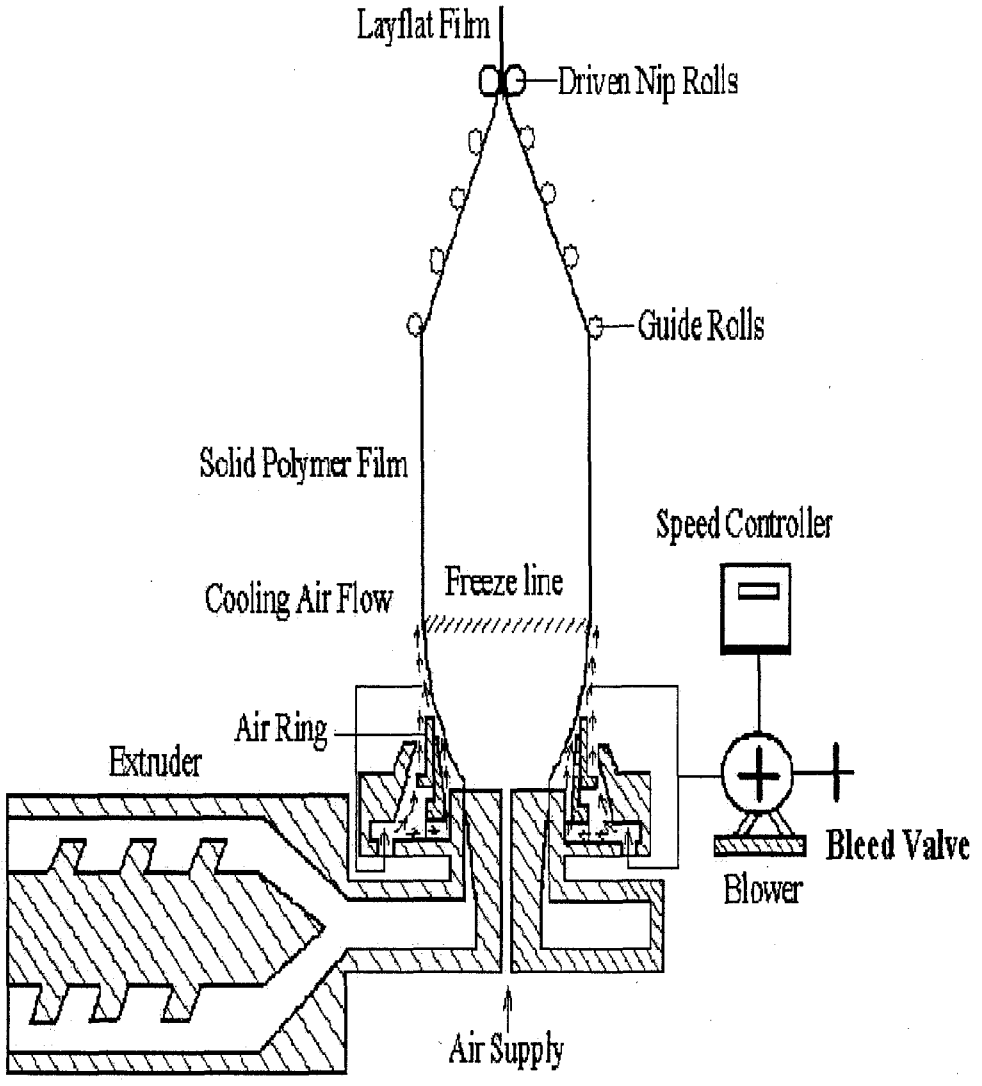

Figure 1.Schematic of the film blowing process (not to scale)

1.1.1 Terminology

Some of the terminology that is part of the film blowing industry's language and used in this dissertation are described as following:

- Blow-Up Ratio(BUR)

  The BUR is defined as the ratio of the final film radius (R_f) to the die radius (R_0), i.e. R_f/R_0. Its value ranges from 0.8 to 4.

- Take-Up-Ratio(TUR)

  The TUR, sometimes called the drawdown ratio (DR), is defined as the ratio of the take-up velocity (V_f) of the nip roller and the extrudate velocity at the exit (V_0), i.e. V_f/V_0; Its value ranges from 10 to 60.

- Frost-Line-Height (FLH)

  The FLH, the position at which solidification starts, is used as an indicator of the cooling effect by external air directed at the molten bubble, and it strongly affects the bubble shape.

- Machine Direction (MD)

  The MD is the tangential direction of the bubble surface (perpendicular to the circumferential plane). This is the direction along which the polymer flows from the die to the nip rollers. Stretching in the MD is primarily due to the DR.

- Transverse Direction (TD)

  Azimuthal direction is referred to as TD. It is also known as the Circumferential Direction (CD). The stretching along this direction is primarily due to the excess air pressure and it is quantified by BUR.

1.1.2 The Dynamics of tubular film forming

The process involves the inflation, stretching and cooling of the thin film. Figure 2 presents a sketch of an axisymmetric thin tubular film with an intrinsic coordinate system having unit vectors in the direction of flow m (meridional), in the tangential t and normal n direction.

Mass conservation gives:

$$Q = 2\pi RhV_m = Const. \tag{1.1}$$

The tangential velocity V_t is always zero. The normal velocity V_n is so small that it can be neglected without error. By differentiating Equation (1.1) with respect to the meridional coordinate m, we obtain the rate of strain tensor (1.2), which can be written as:

$$\varepsilon = \begin{bmatrix} \varepsilon_m & 0 & 0 \\ 0 & \varepsilon_n & 0 \\ 0 & 0 & \varepsilon_t \end{bmatrix} \tag{1.2}$$

Where

$$\varepsilon_m = dV_m/dm \tag{1.3}$$

$$\varepsilon_n = (V_m/h)(dh/dm) \tag{1.4}$$

$$\varepsilon_t = (V_m/R)(dR/dm) \tag{1.5}$$

From continuity, we obtain the following Equation:

$$\varepsilon_m + \varepsilon_n + \varepsilon_t = 0 \tag{1.6}$$

By combining Equations (1.3-1.6), we obtain:

$$\frac{dV_m}{dm} = -\frac{V_m}{h}\frac{dh}{dm} - \frac{V_m}{R}\frac{dR}{dm} \tag{1.7}$$

The equilibrium of forces in the normal direction for the thin membrane assumption is (Tanner, 1985):

$$\frac{\Delta P}{h} = \frac{\sigma_m}{\rho_m} + \frac{\sigma_t}{\rho_t} \tag{1.8}$$

The force balance on any z plane gives:

$$-\pi R^2 \Delta P + 2\pi R h \sigma_m \cos\theta = F_t = const. \tag{1.9}$$

Where F_t is the total force exerted on the thin force, it does not include the weight of the film nor the cooling air drag on the film. This assumption does not introduce a significant error. For symbol definitions of equations 1.1 to 1.9 see nomenclature of chapter 1 (section 1.3) below.

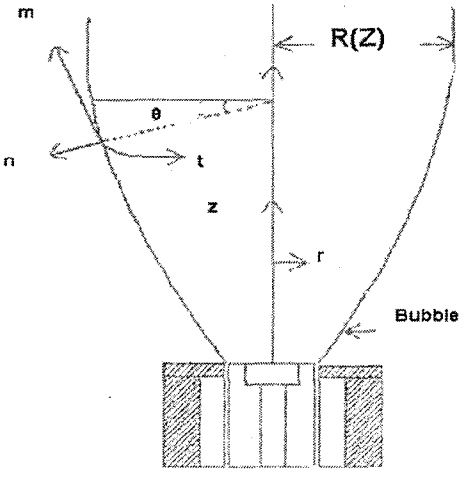

Figure 2. Molten zone of the bubble and intrinsic coordinate system (Sidiropoulos, 2000)

1.1.3 Key Influencing Factors

During the film blowing process, many parameters, as shown in Figure 3, influence the properties of blown films in a complex way. In many film blowing production lines, cooling acts as the major output-limiting factor. Typical output rate for a LDPE blown film line averaged 5-7 lb/hr/inch of die circumference in the 70's. Today on a dual lip air-ring running LLDPE, output rates are approaching 16 lb/hr/inch. Using blends of LDPE with LLDPE and adding internal bubble cooling (IBC), rates can exceed18 lb/hr/inch (Butler, 2000). Accelerating the flow of cooling air seems to be a good way to increase output rate further. However, the cooling of the film blowing process is very complex; it involves many factors such as fluid rheology, heat transfer, bubble instability, and free surface kinematics. The final film properties depend on stresses, deformation rates and thermal history encountered throughout the process. Accelerating the flow of cooling air to increase output can lead to bubble instability, and consequently, to bubble deformation and an unacceptable product. Therefore, the goal of the study, presented in this dissertation, is to understand the effect of cooling aerodynamics on the dynamics of the film blowing process, to improve the cooling efficiency, and to optimize the process.

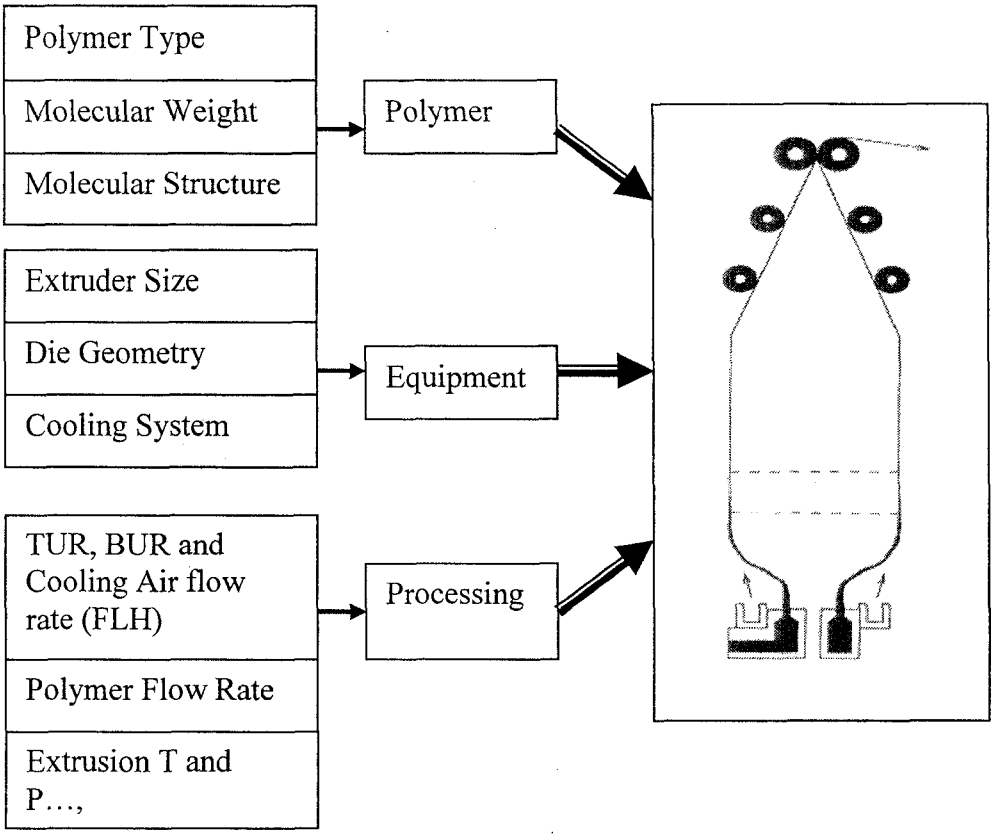

Figure 3 .Some critical process control parameters

1.2 Objectives of the Dissertation

The main objective of this thesis is to improve our understanding of the effects of the air cooling aerodynamics on film blowing. To achieve this goal, the following sub-goals were set:

- To gain an effective theoretical description of the aerodynamics of cooling in the film blowing process, through the investigation of the different boundary conditions.

- To examine extensively the effects of impinging jets on heat transfer from the melt to the cooling air, through comparing the characteristics and performance of flow produced by both single- and dual lip air-rings, as well as, under various processing conditions.
- To detect bubble instabilities induced by varied cooling air flow rates, at different TURs and BURs, and to correlate the bubble instability to the aerodynamic forces.
- To explore the relationship between the bubble instability and the heat transfer rate, under different air cooling conditions.

1.3 Nomenclature for chapter 1

Q: volumetric flow rate

h: film thickness

R: bubble radius

θ: slope of bubble profile

V: film velocity

ρ: curvature of bubble

Δ p: inflation pressure

F_T: total force on the shell

σ: total stress

CHAPTER 2

REVIEW OF THE LITERATURE

There is no polymer-processing operation more important than tubular film extrusion; it has been the subject of numerous experimental and theoretical investigations.

2.1 Air cooling in film blowing

Various process variables (BUR, TUR, inflation pressure, melt temperature, and cooling air flow) have been identified and reported to influence film properties by Huck and Cleg (1961), Han and Kwack(1983), Butler and Patel(1992), Simpson and Harrison (1992), Liu, Bogue and Spruiell (1995) and Debbaut et al (1998). The extensive experimental studies on the kinematics and dynamics of film blowing for various polymers include those by: Han and Park (1975b) on HDPE, LDPE and PP, Gupta (1980) on PS, Winter (1983) on LDPE and HDPE, Kanai and White (1984) on LDPE, LLDPE, HDPE, Tas (1994) on LDPE, Ghaneh-Fard (1997) on LDPE, HDPE, LLDPE and PP, and Kim (2004) on LmPE, LLDPE and LDPE. In their investigations, they have shown that many process variables and polymer characteristics are strongly interdependent. This makes it difficult to predict film properties using simple relationships. This complexity in predicting film properties is the result of several mechanisms that combine to influence the final film properties.

The "thin film" theoretical analysis for the steady blowing of an isothermal Newtonian film first received attention by Pearson (1966), and later in more detail in a series of papers by Pearson and Petrie (1970a, 1970b and 1970c). The thin membrane

approximation based on their approach has provided a theoretical framework for most subsequent studies and is described in a number of publications, including the ones by: Han & Park (1975a), Kanai & White (1985), Tanner (1985), Cao & Campbell (1990) and many others. A good review was provided by Sidiropoulos (1995). Improving on the isothermal assumption, Petrie (1975) proposed a non-isothermal rheological model. Ast (1976) was the first one to solve the energy equation. Wagner (1976), Cao (1990) and Campbell (1992) introduced non-linear, non-isothermal, viscoelastic models. However, the effect of cooling air flow rate on the bubble forming has not been considered in these simulations. The aerodynamics of the cooling air plays an important role in heat transfer and dynamics in the blown-film process, and thus the process analysis excluding the air cooling effect must be taken into account in the simulation.

The actual heat transfer mechanism influenced by the air cooling flow rate was considered by Zippenfeld (1971), Petrie (1974) and Menges et al (1975). In their investigations, they have recognized that the effect of the cooling air flow rate on heat transfer plays a predominant role on predicting the temperature dependent rheological properties of the melt, its crystallization and degree of orientation, as well as, the ultimate properties of the film. By measuring the temperature and velocity profiles of the cooling air, they have proposed correlations to determine the heat transfer coefficient between the cooling air and the bubble, as follows:

$$\text{Zippenfeld model: } h = 7.11(V_{\max})^{0.78} \tag{2.1}$$

$$\text{Menges and Predohl model: } h = 3.3(V_{\max})^{1.5} \tag{2.2}$$

$$\text{Petrie model: } h = 4(V_{\max})^{1.5} \tag{2.3}$$

Later on, a new formula was proposed by Kanai and White (1984), for the region below the FLH as follows:

$$\text{Kanai and White model: } h = 0.043 K_{air} (\mathrm{Re})^{0.78} / L \tag{2.4}$$

Where h is the heat transfer coefficient, V_{max} is the maximum air velocity around the bubble surface, and L is a function of V_{max}. In order to determine h, required by all above expressions, an air velocity distribution model was developed by Cao (1990):

$$u = U\varepsilon^{1/2} \exp(-\beta\varepsilon) \tag{2.5}$$

Where ε is the normalized distance from the bubble surface, U is the local maximum velocity, and β is the distribution index. The parameters U and β are obtained by solving mass and energy balance equations for the cooling air. The results show that the heat transfer coefficient is a function of cooling air velocity; axial distance and bubble shape, etc.

In a related study, Nagarajan and Campbell (1995) proposed an experimental procedure, using rigid models made of aluminium, similar to the shapes observed in the blown film process. They determined the heat transfer coefficient by means of an RdF micro foil heat flow sensor. Their typical curve of heat flux distribution shows that the heat transfer coefficient varies in a random fashion along the axis of the bubble. Although their investigation was limited by some of the assumptions, it provided an experimental method to measure the heat-transfer coefficient.

Constant Temperature Anemometry (CTA, also called hot wire anemometry) was the only equipment, used in the previous studies, to measure air-velocity in the film blowing process. Strater and Dealy (1985 and 1987) used a Disa constant temperature

hot wire anemometer to measure local air velocity in the vicinity of the bubble. They concluded that these velocity distributions are of the general type associated with wall jets; they were unable, however, to make measurements within 5 mm of the bubble surface. Campbell et al (1992) also used a TSI constant temperature anemometer to measure the mean velocity across the flow. They showed that the superposition of stream functions method was not in agreement with the measured data. Hauck et al (1999) analyzed and optimized the cooling conditions, for blown film extrusion lines. The cooling air stream was determined using a hot wire anemometer. However, the only comparison they made was between the measured and the calculated maximum air velocities, at different blow up ratios, and mean temperatures, for processing of LDPE. This is not sufficient to fully understand the aerodynamics of airflow.

A constant inflation pressure was traditionally applied to blown film simulation in all previous analyses (Pearson and Petrie, 1970; Petrie, 1974; Han and Park, 1975; Wagner, 1976; Kanai and White, 1985). Cao and Campbell (1987) however demonstrated that the pressure on the outer surface of a solid, with the general shape of a blown film bubble, varies locally. At the same time, they introduced the momentum balance in terms of the Reynolds equation and the macro balances of mass and kinetic energy to obtain an expression for the pressure on the outer surface of the bubble. The entrainment of air into this tubular wall jet was not taken into account and the effect of backflow is more complicated than assumed. In an effort to minimize these complications, taking the air-ring effect into account, Cao and Campbell (1989) worked out an approximate solution (Equ.2. 6) for the inflation pressure by using a momentum macro balance (a diagram of the air flow over the bubble surface is illustrated as in Figure 4):

:

$$\frac{d\theta}{dz} = \frac{\frac{P_H}{rP_L} - \frac{\Delta P_i}{P_L \cos\theta}}{1 - \frac{\tilde{C}}{rP_L}} \tag{2.6}$$

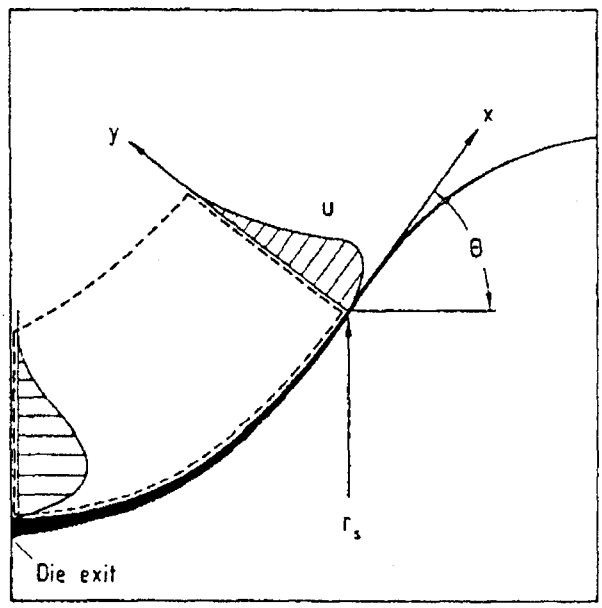

Figure 4. Diagram of the airflow over the bubble surface (Cao and Campbell, 1989)

Where ΔP_i is the pressure difference between the inner surface and the outer surface of the bubble, P_L and P_H are forces in the machine direction (MD) and the transverse direction (TD), respectively. R_L and R_H are the curvatures in the MD and TD directions, given by:

$$R_L = -\frac{1}{\cos\theta \dfrac{d\theta}{dz}} \qquad R_H = \frac{r}{\cos\theta} \tag{2.7}$$

The axial distance from the die exit z, is related to the arc length x according to the relationship: $\cos\theta dx = dz$. The integral constant $\widetilde{C}$ is proportional to the momentum of air at the air-ring exit, and it can be decomposed as a product of the square of the air flow rate, Q, and a scaling factor C, $\widetilde{C} = CQ^2$. The scaling factor is a function of the geometric structure of the air-ring. This equation predicts the pressure outside of the bubble as a function of the airflow rate the bubble shape, and the geometric structure of the air-ring. Although the validations demonstrated a quantitative difference between the prediction and the experimental data, this approach provided for the first time a semi-quantitative formula, which can be directly used in the blown film dynamic analysis, to determine the effect of the airflow on the bubble shape, and the local stress in the film.

Campbell et al. (1992) considered the effect of cooling air velocity on the blown-film formation. They dealt with the aerodynamic aspect of the process by assuming axisymmetric laminar jet flow and introducing a full aerodynamic analysis of the cooling air. They employed two approaches. In the first approach, the macro-balances of mass and energy are used to simulate the air flow around the bubble. In the second approach, they used the method of superposition of stream function to predict velocity and pressure distributions of the airflow. Experimental observations revealed that the method of superposition of stream functions produced one correct stream that coincides with the model contour. In contrast, another method leads to fairly good predictions for the pressure distribution and yields a qualitative agreement between the experiment and the prediction for the velocity distribution. It is of interest to compare the surface pressure obtained using the mass and energy macro balances with the pressure calculated using the momentum balance by Cao et al. (1989). The method of momentum

balance produces a better prediction over the method of mass-energy balances. The pressure distribution seems, always, to be under predicted by the mass and energy balances.

Because the typical Reynolds number, based on the air-ring clearance and the air velocity, exceeds 10^4, (Wolf et al, 1997), the cooling air jet flow regime is classified as turbulent, which is an unstable state of flow that is, always, three dimensional and time dependent. Therefore, a turbulent regime analysis is required for the predictions of air velocity and temperature distributions in the vicinity of the bubble. Wolf et al. (1997) extended Campbell's (1992) work by using the finite element method (FEM) to solve the equations of turbulent airflow for jets impinging on a blown film bubble. They treated cooling air as a turbulent jet flow and simulated airflow around the bubble with the commercially available software FIDAP, using a standard k-ε model. Their results have shown that the air mass flow has the strongest influence on cooling, in the examined processing window, and that the bubble shape is responsible for the occurrence of vortices.

Hauck and Michaeli (1999) carried out an experimental study of velocity and temperature profiles of the air stream and the air pressure along the bubble. They proposed a 1/7 power turbulent analytical model to obtain a theoretical description of the cooling air. The experimental investigations show a significant influence of the cooling air-ring geometry on the cooling characteristics of the blown film extrusion line.

Akaike, Tsuji and Nagano (1999) developed the Abe-Kondo-Nagano model to analyse numerically heat transfer from the surface of the molten polymer to the cooling air. The model was then used to simulate the bubble shape, under the air pressure and thermal boundary conditions estimated from the numerical analysis of the cooling air.

This was the first attempt to associate numerical simulation of air-cooling with the shape of the bubble. The film bubble shape predicted by using the heat transfer coefficient obtained from this model, agrees well with the experimental results. Thus it was confirmed that the effect of the cooling air holds the key to the processability and film properties.

Sidiropoulos and Vlachopoulos (1998, 2000, 2001 and 2002) carried out numerical simulation of aerodynamics for cooling air in the blown-film process, with the renormalization group (RNG) k-ε turbulent model and a commercial software (FLUENT), and published a dozen of papers to examine the aerodynamics of the cooling air produced by both single- and dual lip air-ring designs. They studied the effect of air–ring design, and the operational set-up on the cooling efficiency, and on the heat transfer rate, at different air cooling flow rates. Their results indicated that such a finite volume numerical technique can be a useful tool to study Internal Bubble Cooling (IBC), and fine-tuning of a new or existing installation. Their numerical simulation revealed that the Coanda effect has a significant influence on local heat flux, the air-ring airflow is dominated by the Venturi and Coanda effects, and the air flow patterns are very sensitive to minor air-ring design modifications. They found that the acceleration of the lower jet through the gap between the bubble and the forming cone caused a negative gauge pressure that stabilized the bubble. They also found that there was a recirculation flow region formed below the upper jet before it attached to the bubble. The size of the recirculation region, the distribution of the surface pressure and heat transfer below this recirculation region depended on the flow rates of the two jets, the design of the dual lip air-ring, and the shape of the bubble.

Gregory et al. (2004) developed a simple model to predict the heat transfer coefficient which can be used in blown film simulations. Their experimental results show that the heat transfer coefficient goes through a maximum as the bubble expanded,

which is confirmed by the cooling air velocity distribution around the bubble, measured by means of a hot wire anemometer. They also suggested that the effect of the 3D boundary layer thickness on the bubble radius growth should be incorporated in the simulation. Their calculations based on the corrected boundary layer thickness show excellent agreement with the experimental results.

2.2 Bubble instability

Though cooling air produced by the cooling jets exiting from the air-ring is one of the key factors which stabilize or destabilize the bubble in the film blowing process, little information is available in the literature due to the complexity of the cooling airflow. Yeow (1975) was the first to try a theoretical investigation of the bubble instability using a linear hydrodynamic stability analysis for a Newtonian film under isothermal conditions. He predicted the transition from stability to instability in the neutral-stability curve for different FLH. Cain and Denn (1988) extended Yeow's analysis to that of a Newtonian and viscoelastic upper-convected Maxwell fluid. They found that both the number of steady-state solution branches and stability depended on the processing conditions, i.e. axial velocity at the solidification point, dimensionless tension, a parameter relating inflating pressure to thickness, and fluid viscosity. Yoon and Park (1999) used the mathematical approach of Cain and Denn to evaluate the detailed effects of specific processing conditions on bubble instability. They reported that there was an optimum FLH that resulted in the widest stable region for a fixed amount of air and a given thickness reduction.

Ghijsels et al. (1990) demonstrated experimentally that a low tension bubble induced by a small axial take-up force becomes sensitive to surrounding air flows and gravity forces, resulting in bubble instability. Sweeney and Campbell (1993) carried on a statistical analysis and found that there is a strong level of interaction between various process parameters, including cooling air, which affect bubble stability. Ghaneh-Fard et

al. (1996) studied the stability behavior of four different polyolefins. Special attention was given to the effect of the FLH on the bubble instability. They reported that the air drag force, led by air cooling at low TURs, acting on the bubble surface makes the bubble sensitive to helical instability. Butler (2000) presented experimental results, considering process variables, such as melt temperature, FLH, BUR , and film thickness, to determine the influence of bubble stability on maximum output rate. Laffague and co-workers (2002) developed a new system using an in-line scanning camera with seven mirrors to study the stability when an LLDPE resin was processed. They concluded that the new device can capture quantitatively characteristics of all bubble instabilities. Furthermore, they found that LLDPE instabilities are enhanced by increasing the TUR, BUR, and FLH. Kim et al (2004) extended Laffague's work to investigate dynamics and criteria of bubble instabilities for three commercial film-grade polyethylenes, and at a broad range of TURs, BURs and FLH. A graphical quantification approach to determine the stable zone in the bubble stability map was presented in their study.

The numerical investigations by Feron et al, (1997) focused on the aerodynamics produced by dual lip air-rings. They noted that the occurrence of vortices led by the angle-of-attack, together with the bubble shape, was responsible for the unstable behaviour in the bubble. Sidiropoulos and Vlachopoulos (1998, 2000 and 2002) numerically investigated the flow fields produced by different dual lip air-ring settings compared to sinle-lip air-rings. In their papers, they noted that vortices produced between the bubble and the forming cone can cause a negative static pressure around the bubble, which was assumed to stabilize the bubble. More recently, Gao et. al. (2005) experimentally measured the velocity field in the region above the forming cone, and the pressure distribution on the bubble surface for a rigid model bubble with a BUR of 2.5. They demonstrated that there is a region of negative static pressure on the bubble surface below the forming cone that stabilizes the bubble.

Wortbery and Spirgatis (2004) carried out a numerical investigation of cooling air flow using RNG k-ε turbulence model and predicted the bubble instability in the cooling region which influences the local heat transfer. They aimed at achieving a better understanding of the interaction of air-ring lips, bubble shape, and the development of typical transient flow patterns of cooling air. They suggested the air flow from the air-ring up-to the frost line can be divided into three regions of interest, where the various characteristics and performance of flow in each region produce different effects on the bubble instability and heat transfer from the melt to the cooling air. They concluded that the development of temperature fluctuations in the bubble is responsible for the formation of film thickness profiles in the extrusion direction.

2.3 Summary of the literature review

A brief survey of the literature pertaining to film blowing was presented in this chapter. Additional references to relevant works are cited as and when they are required. The principle objective of this survey is to make sure that the present work is new and presents an improvement over previous studies. Another objective is to understand the background, and the critical issues in the field. To our knowledge, though there have been numerous experimental and theoretical investigations on the film blowing process, there are no numerical analyses to predict a detailed description of the air cooling flow pattern in the real computational domain (bubble shape induced by various cooling air flow rate). There are no simulations to study the characteristics and performance of heat transfer for different air-ring designs under different BURs, and different bubble shapes. An accurate estimate of heat transfer is required to establish the relationship between thermal inertia and cooling air aerodynamics for different bubble geometries. Bubble instability involving the role of aerodynamics forces and cooling effects is not well understood. No quantitative investigation of the relationship between bubble instability and the air cooling flow rate, under different BURs, and TURs, as well as, bubble shape,

was found in the literature. Hence, the proposed work is a new and important contribution.

2.4 Nomenclature for chapter2

h: heat transfer coefficient

Vmax: maximum air velocity around the bubble surface

Kair: constant in Kania model

Re: Reynolds number

ε: normalized distance from the bubble

ΔP_i: the pressure difference between the inner and the outer surface of the bubble

P_L, P_H: forces in machine direction and transverse direction

R_L, R_H: the curvatures in machine direction and transverse direction

z: axial distance from the die

$\widetilde{C}$: model constant

C: scaling factor

Q: air flow rate

CHAPTER 3

METHDOLOGY OF RESEARCH

To achieve our objectives, two research methodologies were used in this dissertation: a simulation investigation (CFD), and an experimental investigation.

3.1 CFD techniques

The science of computational fluid dynamics is made up of many different disciplines from the fields of mathematics and computer science. It can be structured into two parts, generating or creating a solution, and analyzing or visualizing the solution. In order to generate a CFD solution, three processes must be accomplished, namely: geometry definition and grid generation as well as numerical simulation.

3.1.1 Turbulence modeling

The turbulent flow of the cooling air around the bubble is governed by the Navier-Stokes equations. In this work, the RNG k-ε model (Yakhot. 1986) of Fluent was used, which is an improved version of the standard k-ε model, that has been shown to be better suited to the treatment of flow in the regions where the Reynolds number is small (e.g. near the walls). Another advantage of this model is that it calculates the effective inverse turbulent Prandtl number as a function of μ_{mol}/μ_{eff}, which is consistent with experimental evidence, and allows heat transfer to be accounted adequately in low Reynolds number regions.

Using the effective viscosity (μ_{eff}) defined in the RNG k-ε model, the mean momentum equation for a two-dimensional flow can be written as:

$$\frac{\partial(\rho U_i)}{\partial t}+\frac{\partial(\rho U_i U_j)}{\partial x_j}=\frac{\partial}{\partial x_j}\left[\mu_{eff}\left(\frac{\partial U_i}{\partial x_j}+\frac{\partial U_j}{\partial x_i}\right)\right]-\frac{\partial p}{\partial x_i} \tag{3.1}$$

The turbulent transport of energy equation is given by:

$$C_p\left(\frac{\partial(\rho T)}{\partial t}+\frac{\partial(\rho U_i T)}{\partial x_i}\right)=\frac{\partial}{\partial x_i}\left[\alpha_h \mu_{eff} C_p \frac{\partial T}{\partial x_i}+U_j \mu_{eff}\left(\frac{\partial U_i}{\partial x_j}+\frac{\partial U_j}{\partial x_i}\right)\right] \tag{3.2}$$

However, the turbulent models based on the k-ε elements do not take account any wall effect, and are inadequate for the investigation of the momentum and heat transfer near the wall. The enhanced near wall treatment in the Fluent was employed at the solid surface in this study. More details about RNG k-ε model and Enhanced Wall Treatment can be found in the FLUENT user's guide

3.1.2 Simulation methodology

Owing to the symmetry of the bubble with air-ring geometry, a 2D axi-symmetric coordinate system was considered. All computational results, presented in this study, were obtained using the commercial CFD code FLUENT 6.2.16.

A no-slip velocity was imposed along the bubble surface. During the simulations, the temperature profile along this surface was gradually decreased according to the experimental data. Since this boundary condition is not a constant, it was programmed in Fluent as a User Defined Function (UDF). The air was assumed to be an ideal gas and the ambient temperature was set to 298K. The bubble shape was fixed in correspondence to the one measured experimentally. The frost line height was set to 120-300 mm in this work. The cooling air was assumed to enter the domain with a predetermined velocity (U), ambient temperature (T), kinetic energy of turbulence (k), and dissipation rate (ε). The k and ε are calculated from the following expressions:

$$k = \frac{3}{2}(U_i I)^2 \tag{3.3}$$

$$\varepsilon = C_{\mu}^{3/4} \frac{k^{3/2}}{0.07D} \tag{3.4}$$

Where D is a hydraulic diameter of the inlet, the turbulence intensity, I, is defined as the ratio of the root-mean square of the fluctuation velocity to the mean flow velocity:

$$I = \frac{\overline{(u_i')^2}^{1/2}}{U_i} \times 100\% \tag{3.5}$$

The definitions reported in reference (Incropera, 1985) were used to calculate dimensionless Nu and Re numbers. The bubble radius was selected as a l_{Re} value in the definition ($Re=\rho V l_{Re}/\mu$) of Re number.

A second order upwind scheme was applied for the solution of the momentum equation and the transport equations for the turbulence variables (kinetic energy and dissipation rate). Each simulation was run on a pentium4 PC and took between 40 and 60 minutes. Convergence criteria were set in Fluent to ensure that the results were fully converged. For each of the finite volumes, solution of Equation (3.1) gives local values for pressure and velocity; solution of Equation (3.2) gives local values of temperature. The flow streamlines and heat transfer to the wall are calculated from the resulting velocity field and temperature derivative, respectively.

3.2 Experimental methodology

In this study, experimental methodology consisted of running film blowing extrusion under different process conditions, measurement of some parameters used as boundary conditions for the simulation, and capturing quantitatively bubble instabilities.

3.2.1 Blown film extrusion

A 45mm Killion single screw extruder with a helical film die (D_0 = 63.5mm, h_0 = 1.5mm with double lips) was used. The extrusion temperature profile was set as 150/170/180/180/180°C from the hopper to the die. The flow rate of the polymeric resin was maintained at 2.5 ±0.1 kg/hr. The properties of the Low Density Polyethylene, (LDPE) used in this study, are summarized in Table1. The melt index, density and heat capacity were determined by the resin supplier by means of the ASTM-D1238, D792 and C177 methods, respectively. The DSC melting point was supplied by the DOW Chemical Co.

Table 1. Properties of the LDPE used

Properties	**Melt Index** (g/10min)	**Density** (g/cm^3)	**Heat capacity** (J/kg*K)	**Melting point** (K)
Values	0.88	0.9239	2300	385

3.2.2 Air-ring settings

The single- and dual lip air-rings, as schematically shown in Figure 5, were used in this study. In the single lip air-ring design, the air stream flow from the lower lip jets onto the bubble surface through a flow deflector, to steer the flow away from the bubble. This results in a reduction of the pressure at the base of the bubble, and allowing higher flow rates to be used. A dual lip air-ring is set by lowering the adjustable part of a single lip ring and the flow in this setting is split into a lower jet and an upper jet.

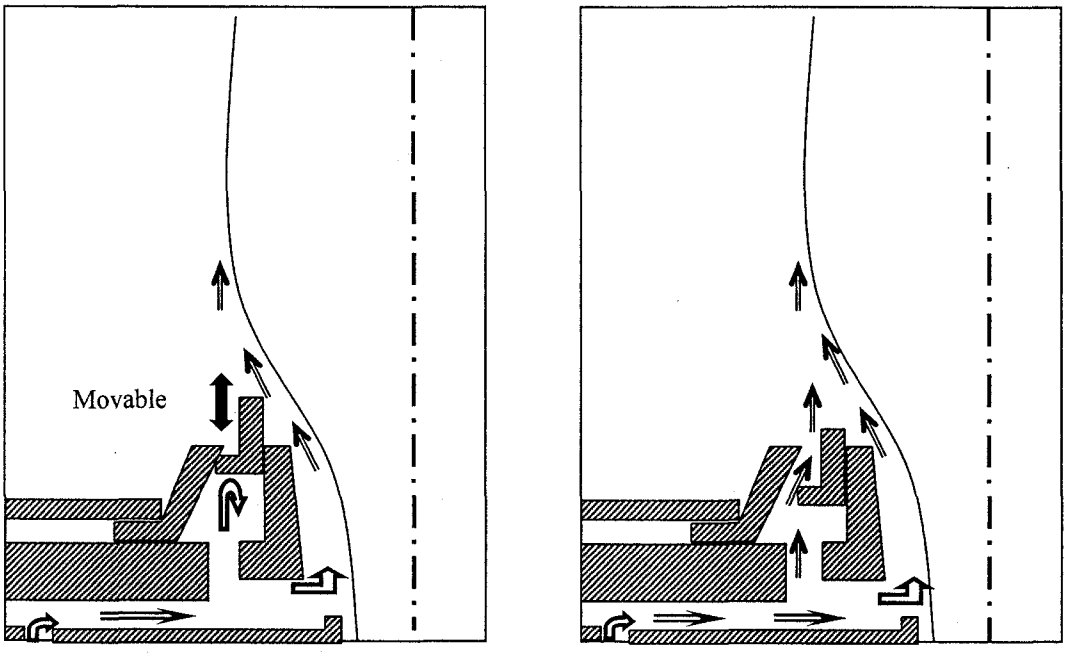

Figure 5.Schematics of different type air-ring (left: single lip, right: dual lip)

3.2.3 Measurements

The volumetric airflow rate through the air-ring was measured by multiplying the air velocity by the wetted area. The air velocity was obtained with a FMA-905-V air velocity transducer made by the OMEGA Co., and calibrated in a NIST-traceable wind tunnel. The temperature at the bubble surface was measured as a function of vertical distance from the die by an infrared pyrometer (IRCON 3400). The pressure inside the bubble was measured using a manometer mounted on the die. The bubble diameter profile was determined by a video camera. The screw rotation and nip rolls rotation

during the processing were stopped, and the bubble was immediately solidified by cooling air. The thickness was then measured on the frozen bubble using a micrometer.

Bubble instabilities were experimentally measured using the in-line scanning camera system developed by Laffague et al. (2002), as shown schematically in Figure 6. This system can provide four parameters as output: 1). Eccentricity, d, 2) Rotation angle, α, 3) Radii of the left and right sides of the bubble (R_{Left} and R_{Right}), and 4) Ratio of the two radii, the relationships between these parameters and geometrical variables are presented as follows:

$$\alpha = \arctan(Y_c / X_c) \tag{3.6}$$

$$d = \sqrt{X_c^2 + Y_c^2} \tag{3.7}$$

$$\text{Radius ratio} = R_{Left} / R_{right} \tag{3.8}$$

This system gives continual information for the transition between stable and unstable zones. The cooling flow rate was increased or decreased gradually in order to generate unstable bubbles. Detailed dynamics of bubble instabilities were investigated as a function of time, at various flow rates of the cooling air, for different TURs and BURs.

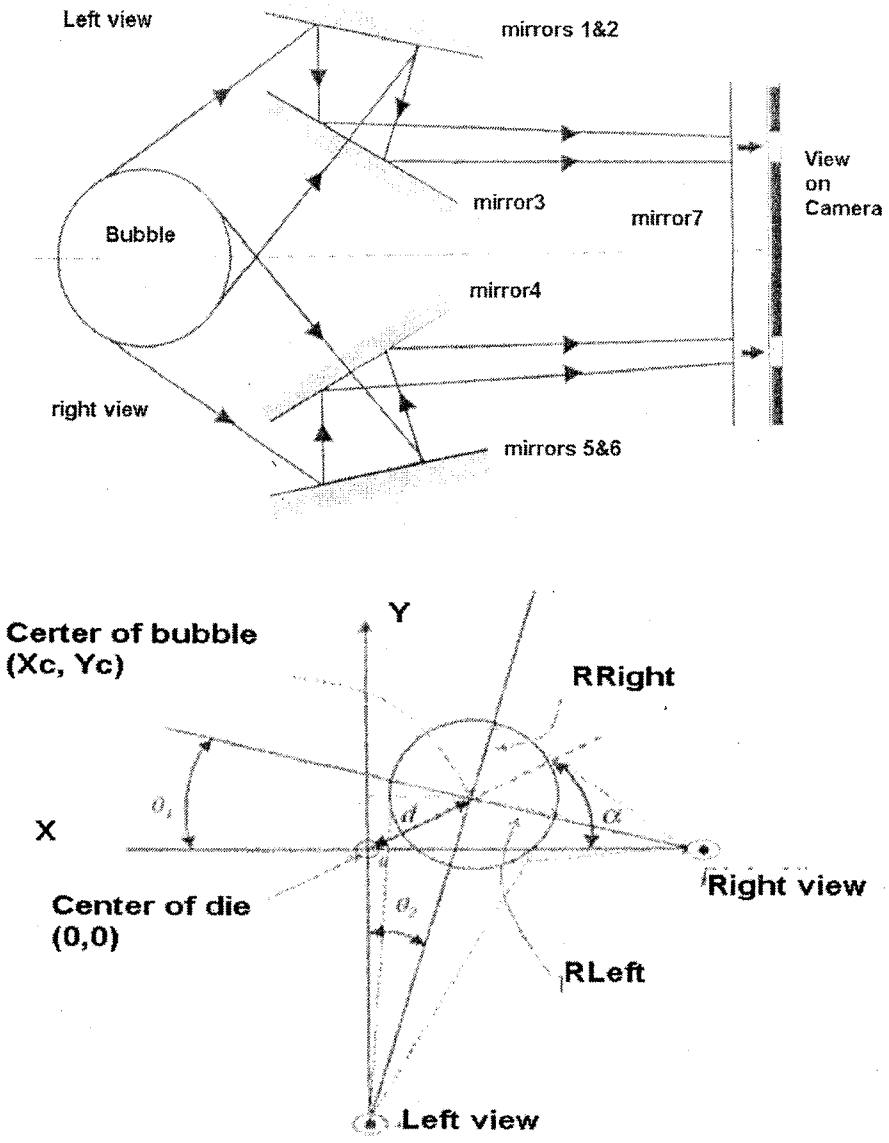

Figure 6. Schematic of the bubble instability measurement system (above) and equivalent geometry of the system (bottom)

3.3 Nomenclature for chapter3

U, $\overline{V}$ mean velocity

p: pressure

μ: viscosity

ρ density of air

μ_{eff} effective viscosity

μ_{mol} molecular viscosity,

Cμ turbulence model constant

α_h inverse turbulent Preandtl number

T: temperature

t: time

k: kinetic energy of turbulence

ε : dissipation rate

I: turbulence intensity,

$$y^+ = \frac{y}{\mu_{mol}}\sqrt{\rho\tau_w}$$

y: the distance from the wall to the cell center

τ_ω: the wall shear stress.

C_p: heat capacity

D: hydraulic diameter

Q: heat flow

z: Axial distance

d: eccentricity of the bubble

α : rotation angle of the bubble

R_{Left} and R_{Right} : radii of the left and right sides of the bubble

CHAPTER 4

GENERAL DISCUSSION

4.1 Presentation of publications

The following publications are presented as appendices to this thesis:

- PEER-REVIEWED CONFERENCE PAPER (Appendix A), Z., Zhang, and P., G., Lafleur, (2005) "Study of aerodynamics of cooling in film blowing", ANTEC 2005, Proceedings of the 63rd SPE Annual Conference, p173-177
- PEER-REVIEWED CONFERENCE PAPER (Appendix B), Z., Zhang, and P., G., Lafleur, (2006) "The effect of cooling air aerodynamics on bubble instability in blown film", ANTEC 2006 Proceedings of the 64th SPE Annual Conference, p840-844
- INTERNATIONAL PEER-REVIEWED PUBLICATION (Appendix C) Z., Zhang, P., G., Lafleur, and F., Bertrand, (2006)" Effect of aerodynamics on film blowing process", International Polymer Processing, XXI, 5, p527-536
- INTERNATIONAL PEER-REVIEWED PUBLICATION (Appendix D) Z., Zhang, and P., G., Lafleur (2007) "A Study of heat transfer in the Blown film Process", Journal of Plastic Film and Sheeting (accepted for publication).
- INTERNATIONAL PEER-REVIEWED PUBLICATION (Appendix E) Z., Zhang, and P., G., Lafleur (2007)" Investigation of blown film instability induced by air cooling", Polymer Engineering and Science (Submitted)

4.2 Links between publications

Two conference papers in Appendix A&B were presented at the 63rd and 64th SPE Annual Technical Conference (ANTEC2005 in Boston, MA and ANTEC 2006 in Charlotte, NC, U.S.A). They contain the preliminary results for the heat transfer rate between the cooling air and the bubble surface, the flow pattern around the bubble using the simulation analysis, and the bubble instability data obtained using the in-line scanning camera system. Overall, it was found that the bubble instability system can capture quantitatively the main characteristics of DR bubble instability. It was found out that various cooling air flow rates have varied influence on the bubble instability, for different BUR bubbles. Furthermore, the heat transfer coefficient was found to depend on the bubble shape and the BUR. The simulation results, predicted maximum air velocity around the bubble surface, in good agreement with the experimental result.

The paper entitled "Effect of aerodynamics on film blowing process" is devoted to study the aerodynamics of cooling air and its influence on the heat transfer, and on bubble instabilities, using a combination of experimental measurements and numerical simulation. Employing a dual lip air-ring, we established a window of operation for the heat transfer coefficient and the maximum air velocity. We also, explored the relationship between thermal inertia and cooling air aerodynamics for different bubble geometries. At the same time, we analyzed the effect of various cooling rates on the dynamics of bubble instabilities for different BUR bubbles under the same TUR. We observed that the bubble instabilities depend on the static pressure distribution along the bubble surface, and that minimizing the pressure gradient can stabilize the bubbles.

The paper entitled "Study of heat transfer in the blown film process" aims at studying heat transfer, through comparing the characteristics and performance of flow

produced by both single- and dual lip air-rings. Employing numerical simulation, we gave a detailed description of fluid flow patterns, and heat transfer coefficients, under different processing conditions. The result of calculations indicated that the heat transfer rate critically depends on the air-ring design. The various boundary conditions led by the air flow rates, were found to be equally important for the cooling efficiency. In addition, the effect of Reynolds number on heat transfer predicted numerically was also reported.

In the article entitled "A Study of the blown film instabilities induced by air cooling", we discussed the bubble instabilities induced by the cooling air flow rate, at different TURs and BURs. We established a good correlation between the bubble instability and the pressure inside it. We found that varying the cooling air flow rate, at different TURs and BURs, produced significant differences in the dynamics of bubble instability. The bubble with the higher TUR sustained greater force caused by the aerodynamics acting on the bubble surface, resulting in broadening of the range of stable operation. A numerical simulation was performed to analyze the effects of the momentum and heat transfer, from the cooling air to the polymeric film on bubble instabilities.

4.3 Synthesis

To achieve a better understanding and validation of the bubble cooling system in the blown film process, numerous experimental and numerical investigations were performed to study cooling jets produced by air-ring systems in film blowing extrusion, the effects of aerodynamics on the heat transfer, the stability and shaping of the molten bubble. The following text provides an overview of the progression of the project and its key findings.

In this dissertation, a Computational Fluid Dynamics (CFD) technique using a renormalization group (RNG) k-ε model coupled with the enhanced wall treatment and FLUENT software was employed to numerically analyze the aerodynamics of the air-ring cooling system in the film blowing process. Topology refinements were examined using different grid sizes (coarse, intermediate, and fine grids) generated with the help of GAMBIT from Fluent corresponding to the various bubble shapes, blow-up ratios, as well as, air-ring set-ups. Pressure and heat transfer coefficients were computed for the three mesh sizes to assess the influence of grid size on the solution. The adequate resolution was employed to ensure that the mesh near the wall was fine enough to take into account the viscous sublayer ($y^+ \approx 1$). Validation of the modeling was performed by comparing the numerical and experimental results for velocity profile of the cooling air around the bubble surface. A good agreement was obtained, especially for the maximum velocity near the air-ring close to the bubble.

4.3.1 Heat transfer

The heat transfer process between the bubble and the cooling air affects significantly the temperature dependent rheological properties of the melt, its crystallization, and degree of orientation upon cooling. The heat transfer coefficient is an effective parameter to describe this process, and the determination of the heat transfer coefficient between the cooling air and the bubble is critical in this study. The simulation analysis, for the heat transfer coefficients of the external cooling air produced by a dual lip air-ring was examined in detail under different bubble shapes at the same BUR. Heat transfer coefficient profiles along the bubble surface, for three bubbles (Bubble1: long neck, Bubble3: short neck and Bubble2: intermediate), are presented in Figure 7. The heat transfer coefficient went up through a maximum, at a location around z = 14mm, and then decreased. Another smaller peak appeared at z = 90mm for Bubble2 and

Bubble3, while the profile of the heat transfer coefficient decreased gradually for Bubble1. Close to the air-ring, the heat transfer coefficient was highest for bubble1, and lowest for bubble3. Away from the air-ring the situation is reversed.

Flow patterns of cooling air are shown in Figure 8 for the three different bubble shapes, and can be used to explain variations of the heat transfer coefficients. The recirculation flow region between the bubble surface and the air-ring gate, as can be seen in the zoom-in sections, reduces the heat transfer rate. The finishing points of vortex are located in the first peak of heat transfer coefficient profiles, which indicates the recirculation flow region is responsible for the presence of the heat transfer coefficient maximum at a position around 14mm from the die exit. Velocity vectors pattern, shown in Figure 9, also gives an explanation, in which we can see higher velocities near the lower-lip jet region for Bubble1 where the heat transfer was calculated to be the highest.

The well-known Venturi effect, which is caused by the air accelerating from the main part of the air-ring (z = 90mm) at the gap formed by the bubble surface and the air-ring provides an explanation to why the second peak in the heat transfer coefficient was the highest for Bubble3. Furthermore, Figure 9 shows that the upper lip of the air-ring injects large volumes of air; the vertical and stream-wise velocity components are simultaneously enhanced by the conjoined flow parallel to the bubble surface, resulting in high Reynolds stresses, and produce high heat transfer rates for Bubble3.

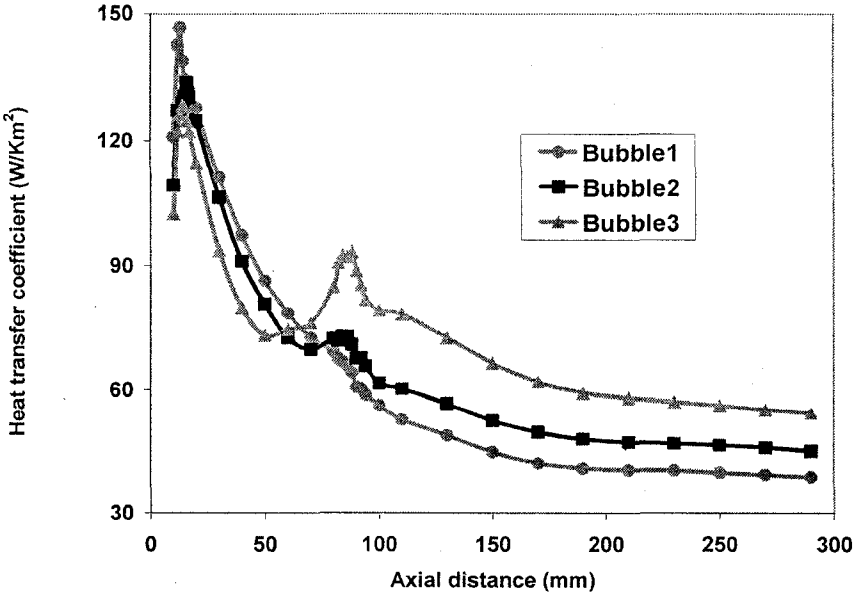

Figure 7.Heat transfer coefficient at different bubble shapes (BUR=2.5)

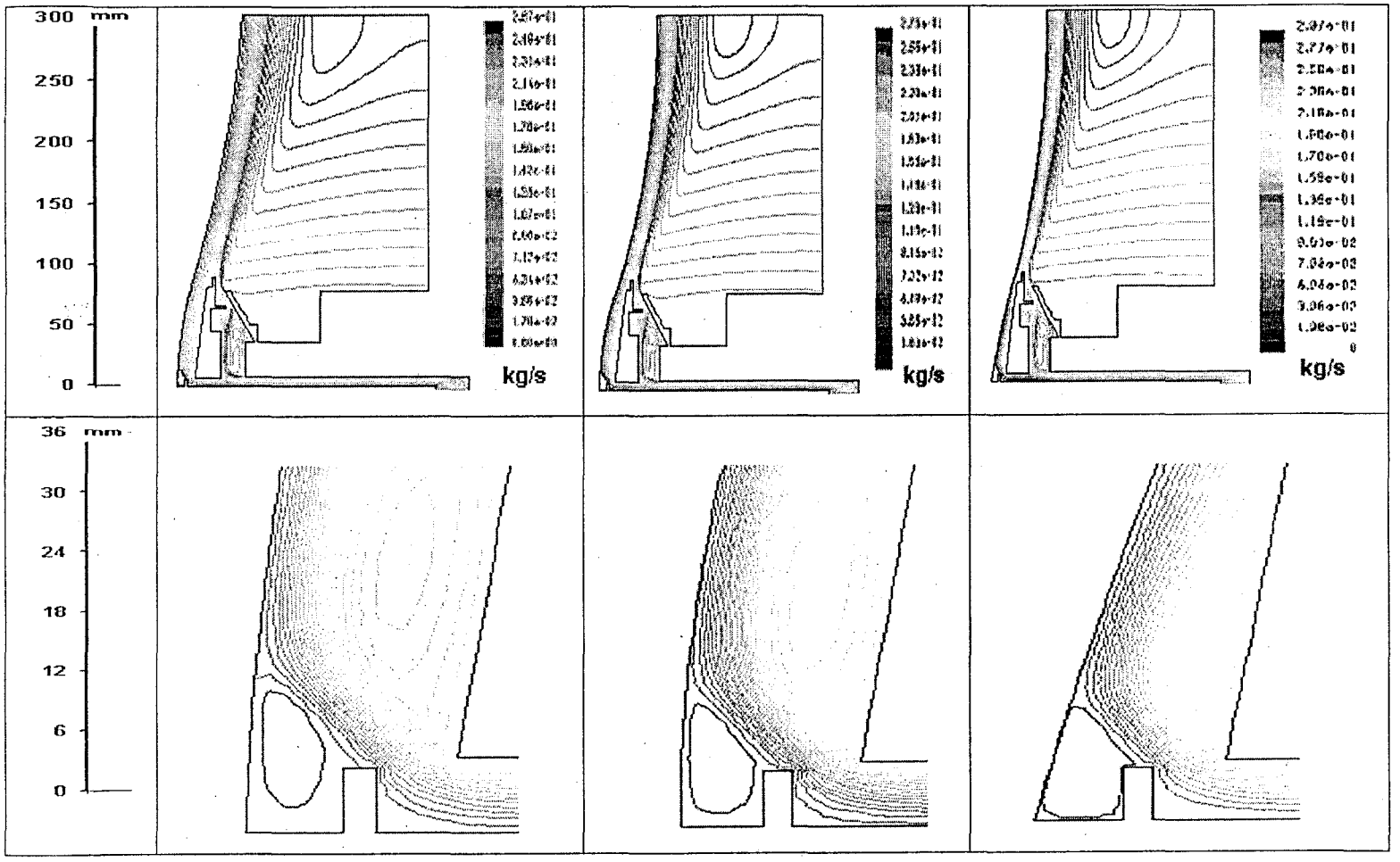

Figure 8.Cooling air streamlines and partial zoom-in of flow abound bubbles (BUR=2.5)

(left:Bubble1; middle:Buble2; right:Bubble3)

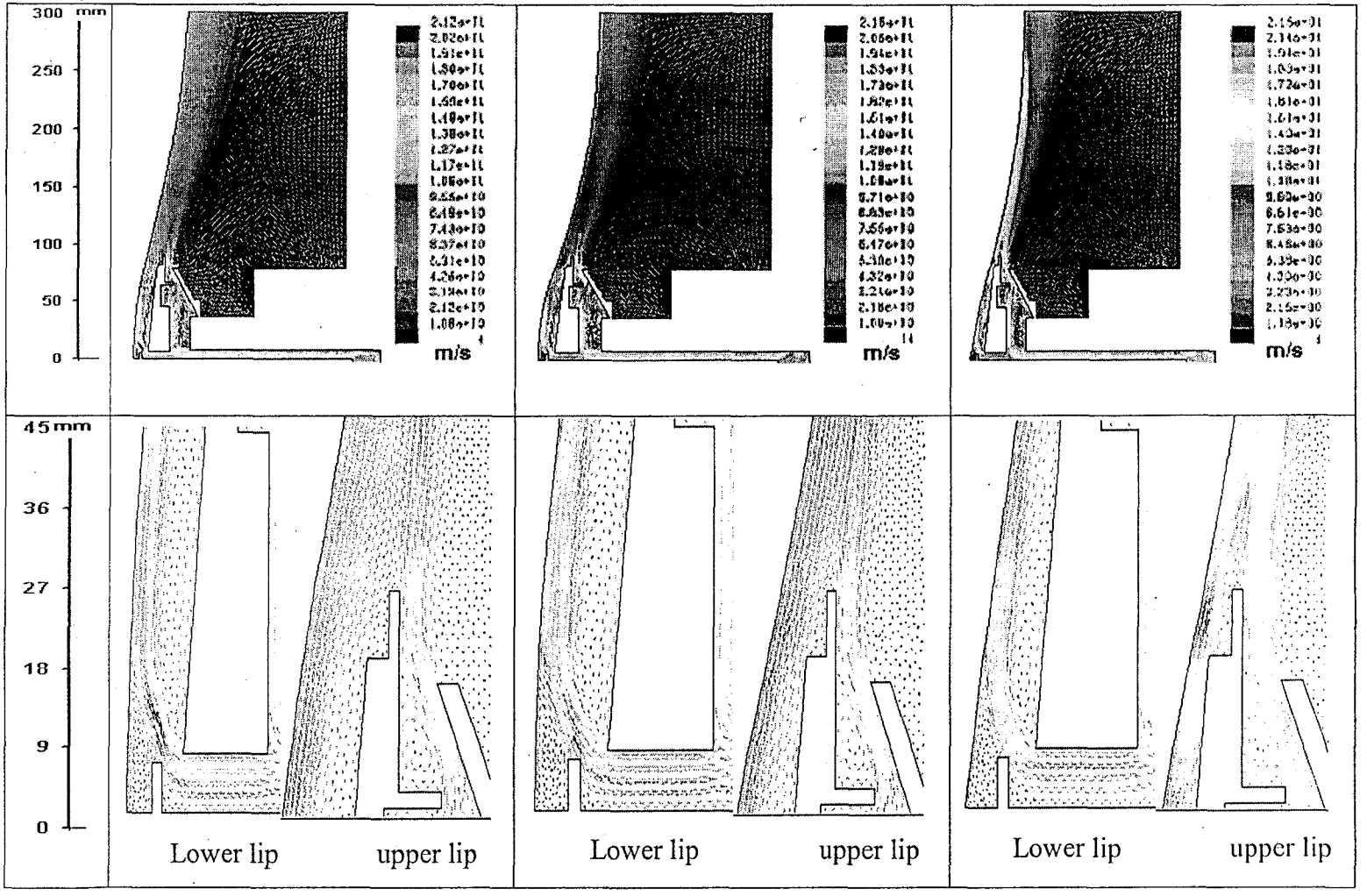

Figure 9.Velocity vectors pattern and partial zoom-in of flow around the bubble surface (BUR=2.5)

(left:Bubble1; middle:Bubble2; right:Bubble3)

Since the heat transfer coefficient is an essential parameter to describe heat transfer between the bubble surfaces and cooling air, several correlations to evaluate it have been proposed in the literature (Equation 2.1-2.5). Numerical analysis was carried out for heat transfer between the bubble and the cooling air as well as the velocity of the cooling air around the bubble at different BUR conditions for single- and dual-lip air rings. The simulation inside the air ring indicated that variation of the maximum velocity (Vmax) around the bubble was independent of the heat transfer coefficient, for both air rings, and under low and high BUR. Therefore, correlations of the form $h = aV_{\max}^{b}$ (a and b are model constants) were considered not suitable for predicting flow and heat transfer inside the air-ring.

Outside the air-ring the maximum velocity profile exhibits the same trend as the heat transfer coefficient; their relationship is almost linear on a logh\logVmax plot as shown in the Figure 10 and 11. The regression coefficient R^2 decreased from 0.98 to 0.86 with a BUR increasing from 1 to 3 for dual lip air ring, indicating that the function ($h = aV_{max}^{b}$) is a better fit for low BURs. The same trend was reported by Gamache et al (2004). However, this result is definitely different for the flow produced by the single lip air-ring, for which the regression coefficient R^2 on the log\log plot is almost constant for different BURs, indicating that $h = a\ V_{max}^{b}$ is adequate for various BUR bubbles produced by the single lip air-ring. The values of the constants in the function depend on the BUR, i.e. $h = 16.6\ V_{max}^{0.56}$, for high BUR, but $h = 3V_{max}^{1.4}$ for low BUR bubbles. The function for low BURs is nearly coincident with Menges and Predohl model (1975). Therefore, the air-ring design directly affects the aerodynamics phenomena in the film blowing process. In order to demonstrate further this conclusion, the characteristics and performance of flow produced by both single- and dual lip air-rings were investigated using various boundary conditions (i.e. different temperature profiles at the same airflow rate, the same temperature profile or same bubble shape at different air flow rates). The simulation and experimental results show significant differences in the heat transfer rate between single- and dual lip air-rings, which means a dual lip air-rings spread the heat

transfer action over a broad area on the bubble surface, Single lip air-rings, on the other hand, concentrate their cooling action inside the air-ring.

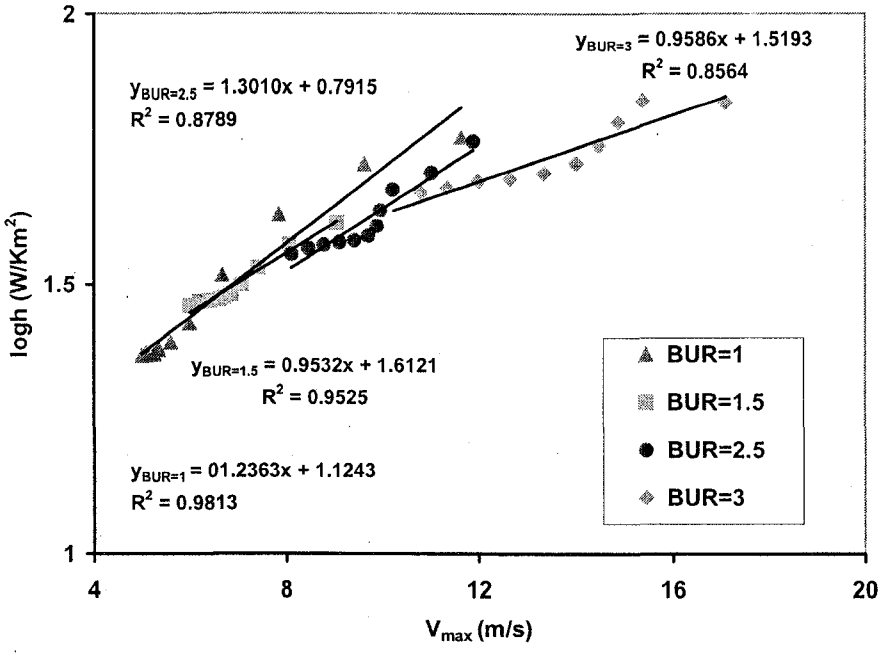

Figure. 10 Linear regression log (h) versus Vmax outside the dual lip air ring at different BUR

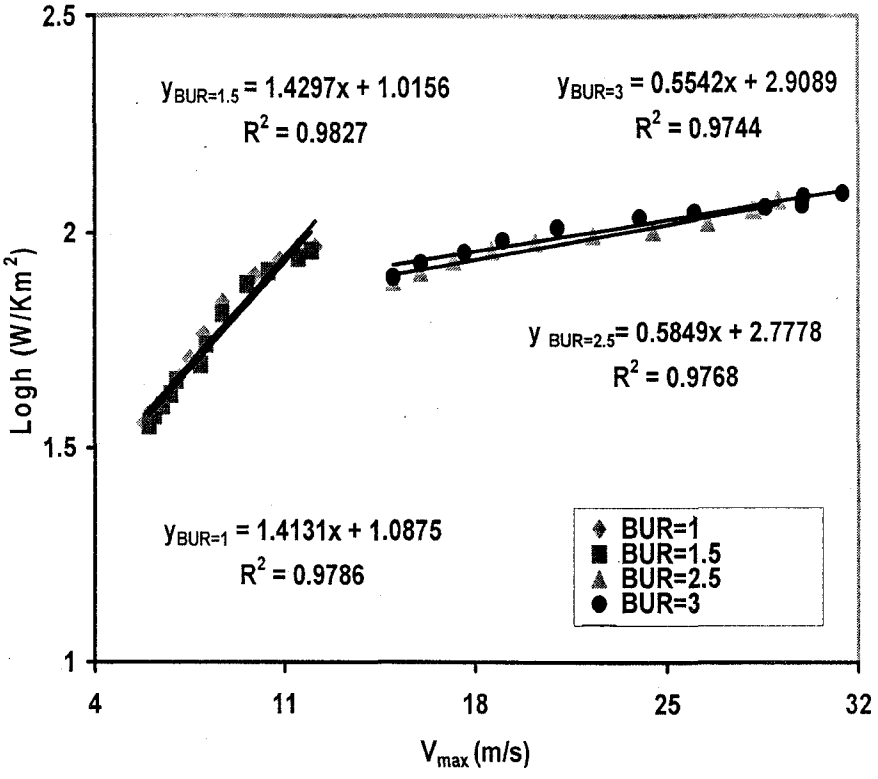

Figure. 11 Linear regression log (h) versus Vmax outside the single lip air ring at different BUR

At the bubble surface, the flow can be defined into two regions: an inner layer (between the bubble surface and the maximum air velocity position), and an outer jet (between the maximum air velocity position and infinity), as illustrated in Figure 12. The maximum velocity just outside the inner layer is considered as the effect of the heat transfer in the function $h = a V_{max}^{b}$. However, the heat transfer between the bubble and cooling air is also affected by the turbulent characteristics in the outer layer that propagates into the inner layer. All approaches employing in the form ($h = a V_{max}^{b}$) seem to be passive considering this point. There is more discrepancy in predicting the

relationship under circumstances such as those for the flow produced by a dual lip air-ring at the high BUR.

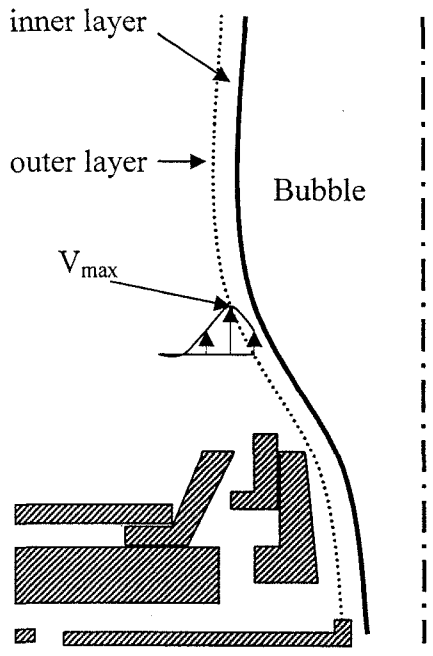

Figure 12. Impinging jet nomenclature

Table 2. Influence of Reynolds number on the heat transfer rate

AD (mm)	Single lip air-ring						Dual lip air-ring					
	BUR=1			BUR=3			BUR=1			BUR=3		
	$Nu*10^{-2}$	$Re*10^{-4}$	logNu/logRe	$Nu*10^{-2}$	$Re*10^{-4}$	logNu/logRe	$Nu*10^{-2}$	$Re*10^{-4}$	logNu/logRe	$Nu*10^{-2}$	$Re*10^{-4}$	logNu/logRe
30	4.84	4.96	0.57	4.97	4.86	0.57	3.64	2.65	0.58	3.57	2.69	0.56
40	4.23	4.88	0.56	4.23	4.88	0.56	2.94	2.46	0.56	2.83	2.50	0.56
50	3.91	4.69	0.56	3.99	4.59	0.56	2.59	2.32	0.55	2.54	2.19	0.55
60	3.68	4.44	0.55	3.58	4.60	0.55	2.37	2.06	0.55	2.31	2.00	0.55
70	3.36	4.06	0.55	3.52	4.23	0.55	2.22	1.79	0.55	2.12	1.74	0.55
80	3.20	3.62	0.55	3.24	3.98	0.55	2.03	1.54	0.55	1.98	1.24	0.56
90	2.99	3.27	0.55	3.12	3.73	0.55	1.89	1.21	0.56	1.80	0.88	0.57
110	2.32	2.96	0.53	2.69	2.19	0.56	1.43	1.35	0.52	1.39	0.91	0.54
130	2.02	2.57	0.52	2.62	3.28	0.54	1.19	1.23	0.51	1.19	1.25	0.51
150	1.70	2.23	0.51	2.47	3.37	0.53	1.03	1.20	0.49	1.14	1.31	0.50
170	1.35	2.07	0.49	2.27	3.61	0.52	0.90	1.37	0.47	1.13	1.19	0.50
190	1.13	1.97	0.48	2.16	4.64	0.50	0.81	1.31	0.46	1.21	1.53	0.50
210	1.02	1.88	0.47	2.35	4.73	0.51	0.82	1.33	0.46	1.48	1.81	0.51
230	0.97	1.71	0.47	2.48	4.89	0.51	0.86	1.33	0.47	1.64	2.87	0.50
250	0.92	1.60	0.47	2.56	4.81	0.51	0.87	1.32	0.47	1.72	2.95	0.50
270	0.86	1.44	0.47	2.56	4.60	0.52	0.87	1.29	0.47	1.82	2.87	0.51
290	0.80	1.38	0.46	2.44	4.35	0.51	0.84	1.29	0.47	1.89	2.39	0.52

The characteristics of flow appear to be uniquely determined by the Reynolds number. Heat transfer rate can be effectively correlated to the Reynolds number. In order to generalize the results, the heat transfer rate is expressed in terms of the Nusselt number. The Nusselt number and the Reynolds number, obtained from the simulation, along the axial distance are listed in Table 2 corresponding to the various BURs. The variations of Reynolds number seem random along the downstream for both air-ring settings at various BURs. However, these variations are a function of the Nusselt number. Inside the air-ring, the function is totally independent of the BUR and the air-ring settings, expressed approximately as follows:

$$Nu = \mathrm{Re}^{0.56} \tag{4.1}$$

Outside the air-ring, the constant n in the function $Nu = \mathrm{Re}^{n}$ depends on the variation of the BUR. An exception appears at z = 90-110 mm. This is attributed to the combined effect of the Venturi effect and the mixing jetting from the upper lip.

Contours of velocity magnitude inside the air-ring plotted on cross-sections of the simulation domain in Figure13, exhibited a complex behavior of the impinging flow and its related phenomena that affects the cooling performance. The simulation results indicate that the flow configurations are noticeable differences at the same inlet air flow rate, and for different air-ring settings. The curvature of the streamlines at the entrance of the lower lip is observed for the single lip air-ring only. For the dual lip air-ring, a small recirculation pattern is observed at the separation flow point. The flow in this setting is split into two jets, resulting in a lower downstream air velocity than that for the single lip air-ring. For the recirculating flow zone after the air-ring gate, the size of the vortex cone is larger with a higher air velocity for single lip air-ring, when the flow attaches to the bubble surface. Since the recirculation flow region has significant

influence on the heat transfer rate, such varied flow configurations for the single- and dual- lip air-rings can explain why the single air-ring is concentrating its cooling action inside the air-ring.

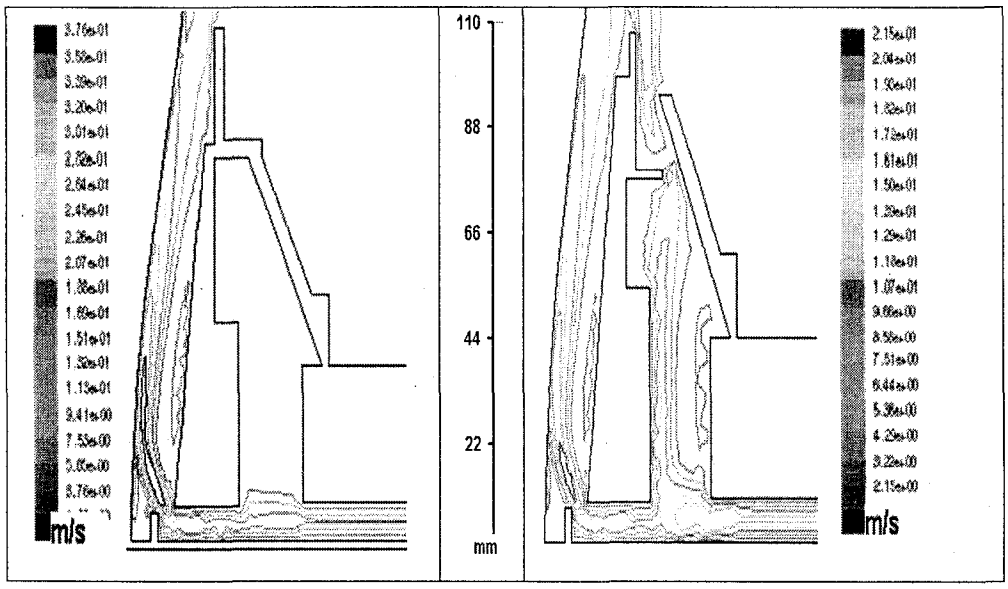

Figure 13 .Contours of velocity magnitude inside the air-ring (left: single lip air-ring, right: dual lip air-ring)

Velocity vectors of the cooling air are shown in Figure14 for flow generated by different air-rings at different BURs. For low BURs, the heat transfer rate is lightly enhanced for dual lip air-rings, due to the conjoined flow from the upper lip. For high BURs, the behavior of the impinging flow appears pronouncedly complex. The heat transfer rate is enhanced by the Venturi effect due to the increase in bubble diameter as compared to the BUR of 1, for both of air-ring settings. The degree of enhancement depends on the gap formed by the bubble surface and the air-ring. As also shown in Figure 14, the higher velocity region becomes wider with increasing the distance from the die, for both air-rings. A larger inner layer, observed for the flow pattern produced by the dual lip air-ring, indicates that the distance between the maximum air velocity and the bubble surface increased with the volume of air injected by the upper lip of the air-

ring. The larger the inner layer, the more important the effects of turbulence characteristic of the outer layer on the heat transfer. On the other hand, the Reynolds number is increased by a combination of the Venturi effect and the mixing jet for the dual lip air-ring, resulting in a downstream flow seems to be transition. This combined effect is enhanced with increasing the BUR. This is the reason why the fit is not good for the relationships between the heat transfer coefficient and the maximum velocity, cited in the literature ($h = aV_{max}^{b}$), at high BURs for the dual lip air-ring.

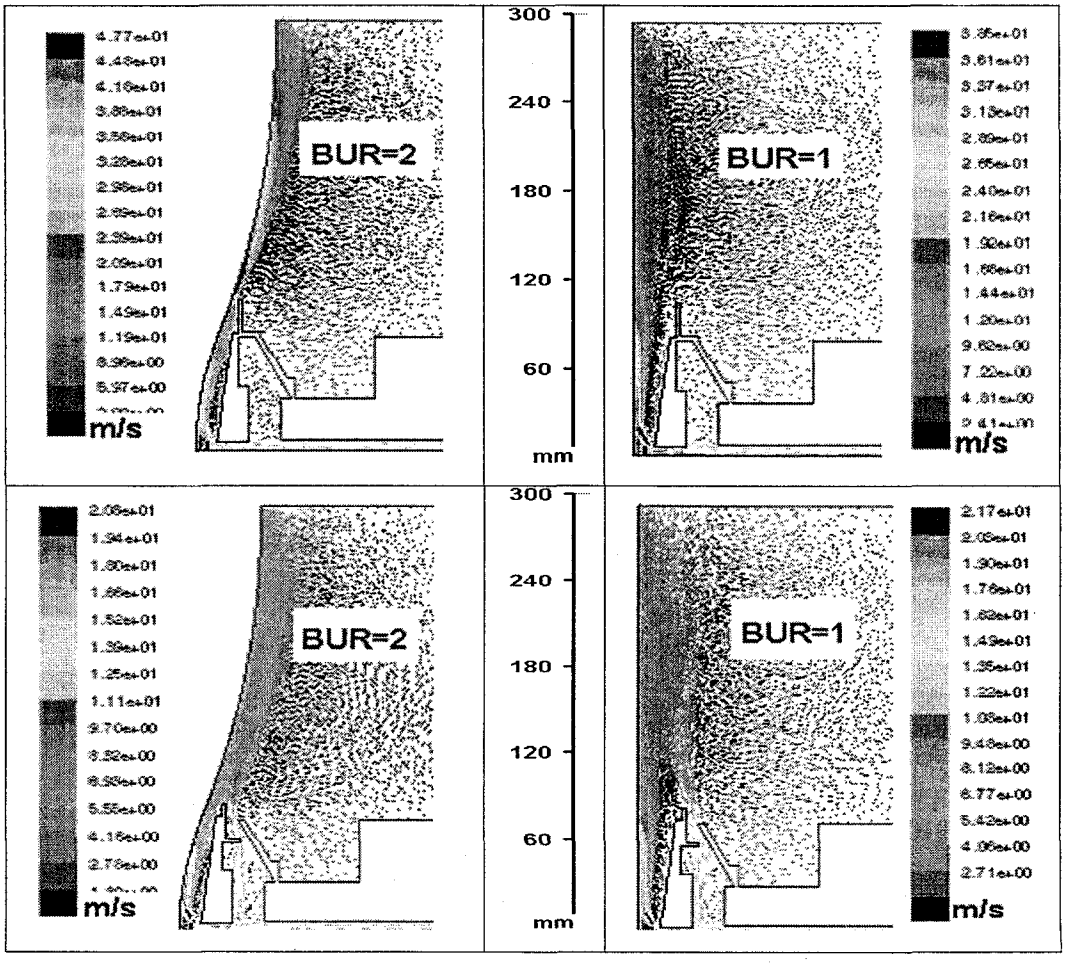

Figure 14.Velocity vectors in the simulation volume at different BURs (top: single lip air-ring, bottom: dual lip air-ring)

4.3.2 Bubble instability

The bubble instability depends on many parameters in the film blowing process with aerodynamic forces being one of them. To investigate the relationship between bubble instability and the aerodynamics of cooling jets is our other main objective. An in-line scanning camera system was used to study the detailed dynamics of bubble instabilities as a function of time, for the dual lip air-ring system, in film blowing extrusion. Draw Resonance (DR) is considered in this study, which is characterized by the radius variation of the bubble. The radius variation (ΔR) is defined as follows:

$$\Delta R = (R_r - R_s) * 100 / R_s \tag{4.2}$$

Where R_r is the observed radius and R_s is the set radius. A radius variation of ±2.5% is the criterion proposed by Laffague et al. (2002) for differentiating various instabilities. This criterion was confirmed by Kim et al. (2004), based on their experimental data for various operating conditions with different polymers.

First of all, the main characteristics of bubble instabilities caused by the air flow rate were captured quantitatively at a constant TUR. The experimental results show that the cooling rate is the most important effect on bubble instabilities. For a BUR of 1, when the air flow rate was varied up to 3.61 l/s, a typical stable bubble was observed with a radius variation of less than 1%. Increasing the flow rate to 4.03 l/s, variation of the radius increased up to around 4 % with periodic oscillations, and exceeded the critical value of 2.5%. With another increase of 0.19 l/s, the variation of the radius dramatically changed and showed oscillations greater than 20%. The situation is reversed for a bubble with a BUR of 2. When the flow rate was set to 1.63 l/s; the radius variation exceeded the critical value of 2.5% with periodic oscillations. The bubble showed typical draw resonance instability with a long-neck shape. An increase of air

flow rate can change the bubble shape from long-neck to short-neck. At the same time, the radius variation decreased to around 2.5 %. The air flow rate was then increased to 2.10 l/s, stabilizing the bubble. A further increase of air flow rate would result in a bubble sitting down on the air- ring and collapsing. Therefore, increasing the air cooling rate can destabilize the low BUR bubbles, but stabilize the high BUR ones due to the production of different bubble shapes.

Although the air flow rate for different BUR bubbles play an opposing effect on the bubble instability, the combination of experimental data and simulation show that bubble instabilities depend on the static pressure distribution along the bubble surface, and that minimizing the pressure gradient can stabilize the bubbles. Static pressure and pressure gradient distributions along the bubble surface, obtained from the numerical analysis, are presented in Figures15 and 16. For a BUR of 1, the unstable bubble shows more pressure variation than the stable one. It is reasonable that the higher flow rate of cooling air can produce the higher pressure gradient around the bubble surface, and then destabilizes the bubble. For a BUR of 2, the complexity of the aerodynamics acting on the bubble surface produces a different effect from the one presented for a BUR of 1. A higher flow rate generated a lower static pressure gradient on the bubble surface, resulting in a stable bubble. The first peak, in the pressure profile, was higher for the smaller flow rates than for the greater ones. Another peak appeared at z = 70 mm for the unstable bubble, while the pressure profile increased gradually for the stable bubble. This is the reason why the unstable bubble has a long neck. On the other hand, the aerodynamics of cooling air determines the shape of the bubble. Varying the flow rate caused a variation of static pressure on the bubble surface, and then changed the bubble shape. As a result, the static pressure was re-distributed with the changing bubble shape. The acceleration due to the narrow gap between the air-ring and the film produced another big vortex, as shown in the Figure17, which resulted in a negative pressure in the pressure profile. The negative pressure region from z = 50mm to z = 90mm seems to be responsible for the bubble sitting down on the air-ring. Part of the air stream

emerging through the lower lip is forced to travel close to the bubble surface via the flow deflector. The vortex created between the flow deflector and the base of the film, presented in Figure 17, corresponds to the initial negative pressure in the static pressure profile, as shown in the Figure16. This local negative static pressure caused by the vortex helps to stabilize the bubble by avoiding high speed airflow to act on the initial stage of the bubble. However, such a recirculation flow region between the bubble surface and the air-ring gate reduced the heat transfer rate.

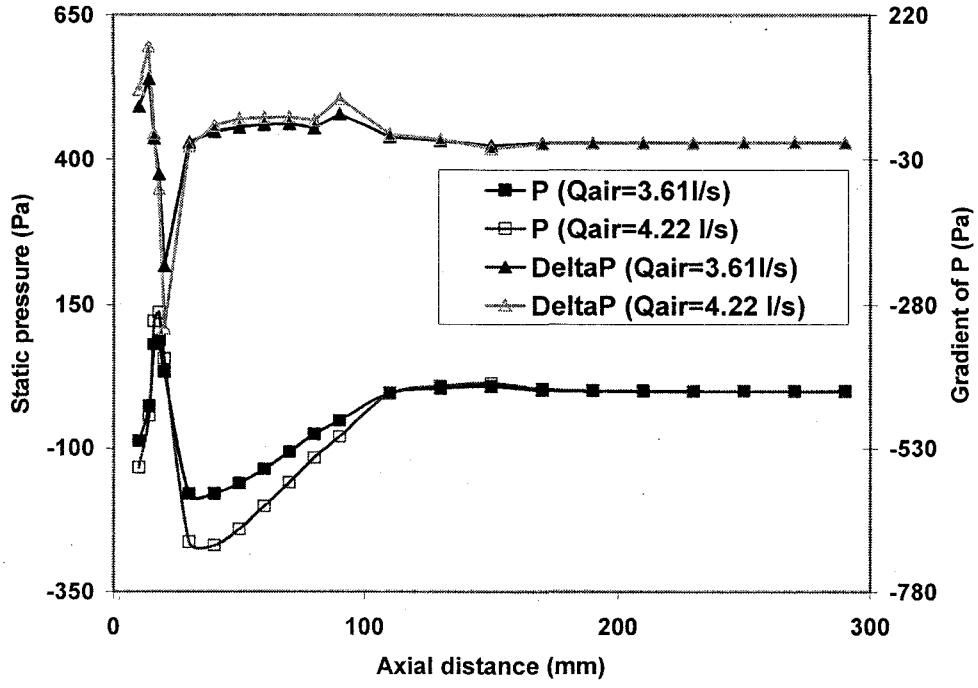

Figure 15. Pressure Gradient and pressure profile around the bubble surface for different air flow rates (BUR=1)

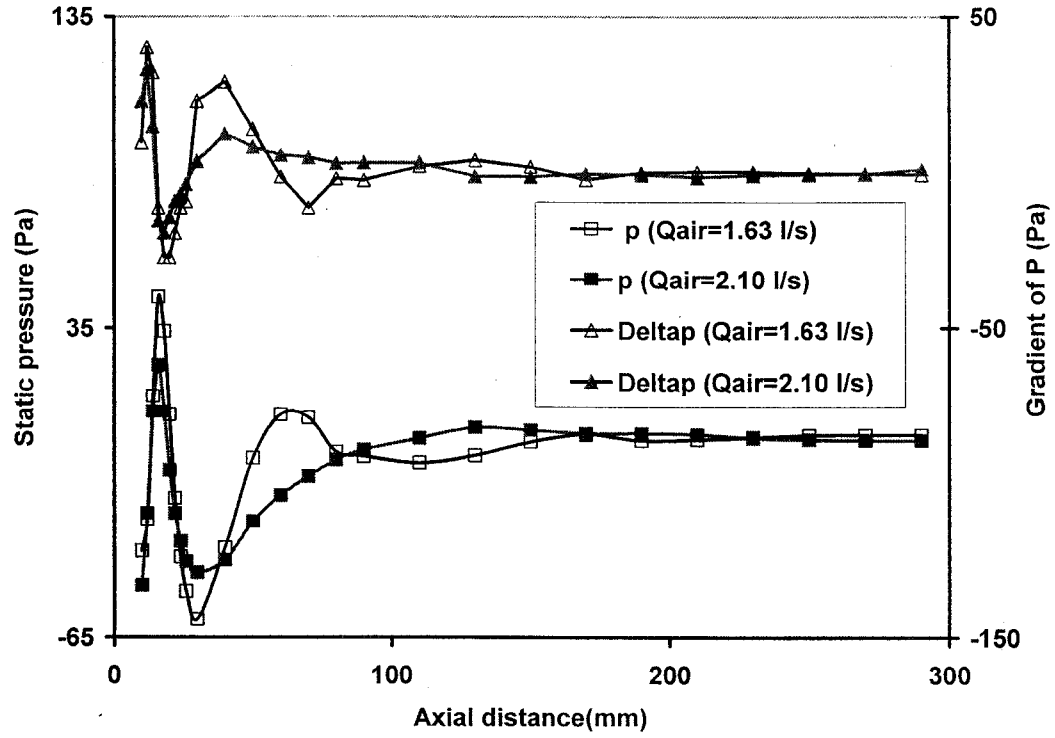

Figure 16. Pressure Gradient profile around the bubble surface for different air flow rates (BUR=2)

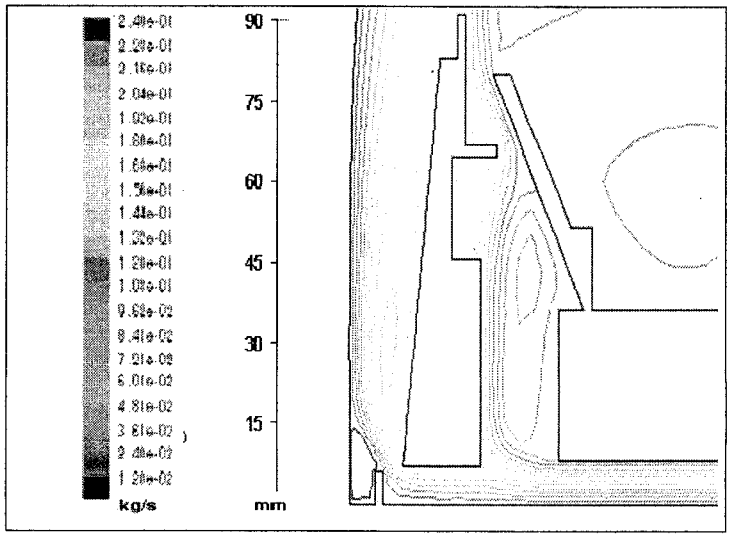

Figure 17.Cooling air streamlines around the bubble inside the air-ring

As the experimental observations provided in the publications, the bubble instabilities depend on a strong level of interaction between various process parameters including TUR, BUR and the cooling air flow rate used. The detailed experimental procedure used in our study is summarized in Table 3.

Table 3.Experimental Design

BUR	1					1.75					2				
TUR	20	30	40	50	60	20	30	40	50	60	20	30	40	50	60
Air flow rate	Vary gradually to affect transition of the bubble from stable to unstable														

The results, which examined the instability for a BUR of 1at keeping value of the increasing air flow rate as a constant rate of 0.11l/s for each step, indicated that the cooling jets, for different TUR bubbles, play a significant role in the dynamics of instability. While TUR was set at a low value of 20, with increasing the air flow rate from 4.77 l/s to 5.10 l/s (i.e. 3steps), the radius variation of the bubble showed a gradual change from 1.2% to 4.1%, among which a typical DR instability was observed with a radius variation of more than 2.5% when the air flow rate was increased from 4.99 to 5.10 l/s. At a TUR of 40, however, a typical stable bubble was maintained with a radius variation of less than 1% when the air flow rate was increased from 6.46l/s to 6.68l/s. With another increase of 0.11l/s, the radius variations went up to around 4.6 % with periodic oscillations, and exceeding the critical value of 2.5%.

Table 4 shows other effects of the air cooling rate on bubble instabilities. The value of the air flow rate producing bubble DR instability increased up to a TUR of 40 and then decreased.

Since DR instability can cause film gauge and layflat variations because of different expansions in the Transverse Direction (TD). These variations are minimized through process optimization. When TUR was set at 40 (see Table 4), a minimal radius variation of 0.28% was obtained at the most stable state (RVMS), while the air flow rate was at a maximum.

Table 4.Radius variation as a function of air flow rate at different TURs and a BUR=1

TUR	20	30	40	50	60
Air flow rate at DR (l/s)	4.99	5.34	6.79	6.56	6.12
RVMS* %	1.2	1	0.28	0.38	1
Air flow rate at MS (l/s)	4.49	4.74	6.45	5.69	6.05
Average thickness of film (μm)	106.5	67	44.5	38	29

*RVMS: the radius variation at the most stable state

As was discussed earlier, the effect of the air cooling rate on the instability for a bubble with a BUR of more than 1 was different from that with a BUR of 1, and the average diameter of a long-neck bubble to short-neck shaped is decreased with increasing the air flow rate. A further increase of the air flow rate would result in a bubble sitting down on the air-ring and collapsing for a BUR of 2. However, the average diameter of the bubble increased somewhat and the shape remained virtually unchanged with further increasing air flow rate, as compared to the results when keeping air flow rate at 2.28l/s for a BUR of 1.75 as shown in the Figure18. Meanwhile, a change in the radius variation with increasing of air flow rate shows an equivalent tendency as a BUR of 1 comparing with a BUR of 2.

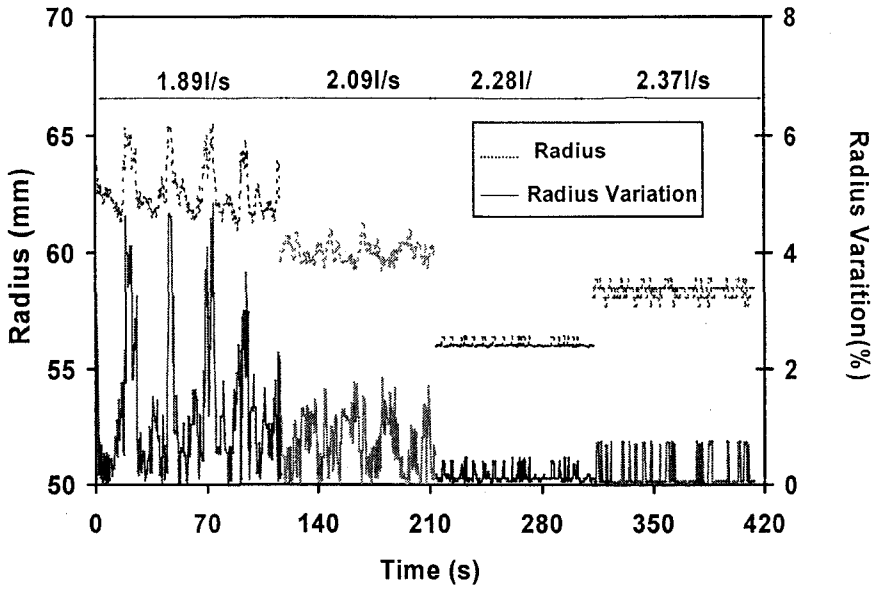

Figure 18. Radius and radius variation response at different air flow rates (BUR=1.75, TUR=30)

The detailed shape of a bubble with a BUR of 2, under different TURs, at the DR critical point (i.e. the radius variation of 2.5%), were found to be different as shown in Figure19. It was observed that the bubble at a TUR of 20 was more notably short-necked and inflated within a shorter distance, or narrow region of altitude. As the value of TUR was increased, so did the angle formed by the film at the position of inflation. All of this implies that a bubble at higher TUR presents a wider operating window, considering the variation in the air flow rate. The same observation was found for a BUR of 1.75. Additionally, the air flow rate producing DR instability attains a maximum at a TUR of 50 for a BUR of 1.75. However, at a TUR of 40, a corresponding maximum was found for a BUR of 2.

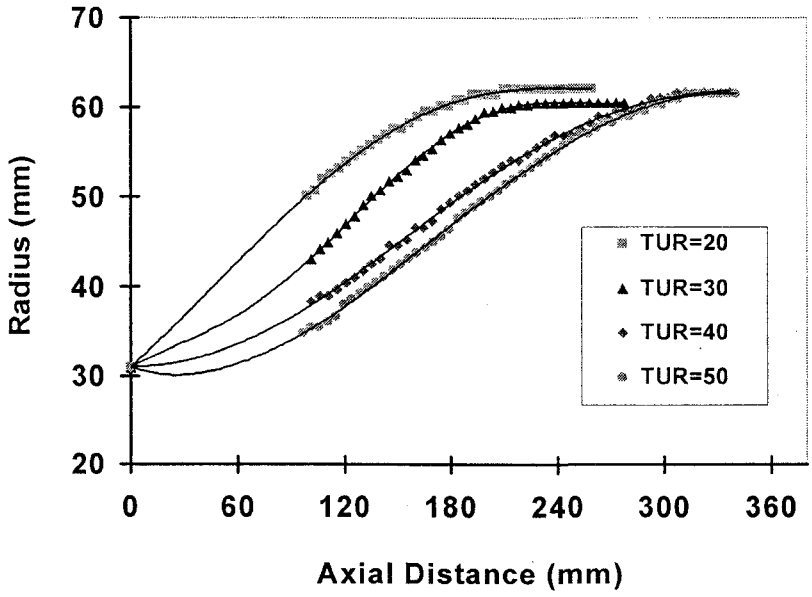

Figure 19.Bubble shape at the instability critical point (BUR=2)

When capturing bubble instability, an on-site manometer on the die was employed to monitor instantaneously the inside bubble pressure corresponding to the radius variation. A good correlation between the bubble instability and the pressure inside the bubble has been obtained. These experimental observations verified Huang's (1988) report that the pressure and the bubble radius varied with the same period and in phase. When the DR instability occurred, 10% variations of pressure were observed, larger than those corresponding to stable bubbles. This observation is adequate mainly at low BURs. For a high BUR bubble, we found that the lowest average internal pressure with the minimal radius variation indicated that a stable bubble appears. The increase in the bubble volume as the bubble expanded from a long-neck to short- neck shape corresponded to a decrease in the average internal pressure of the bubble. Figure20 exhibits the corresponding profiles of the pressure inside the bubble. The value of the average pressure inside the bubble was 67.5 ± 0.9Pa, at the air flow rate of 1.89l/s (instability behavior, as shown in the Figure18). The standard deviation of the inside

pressure was approximately 1.26%, i.e. in percentage smaller than 10%, which is obtained in draw resonance for a BUR of 1. However, when the air flow rate was increased to 2.28l/s, the bubble showed a minimal radius variation, at the lowest average internal pressure. The same phenomena were observed at larger BUR values of 2 and 2.5. After air flow rate stabilizing the bubble, the pressure went up dramatically to 75.8±1.4Pa for a BUR of 1.75. That pressure dropped down suddenly for high BURs because of the bubble attaching itself to the air-ring and collapsing. This observation demonstrates that the dynamics of the air flow inside the bubble plays the same major role in this type of instability for high BUR bubbles.

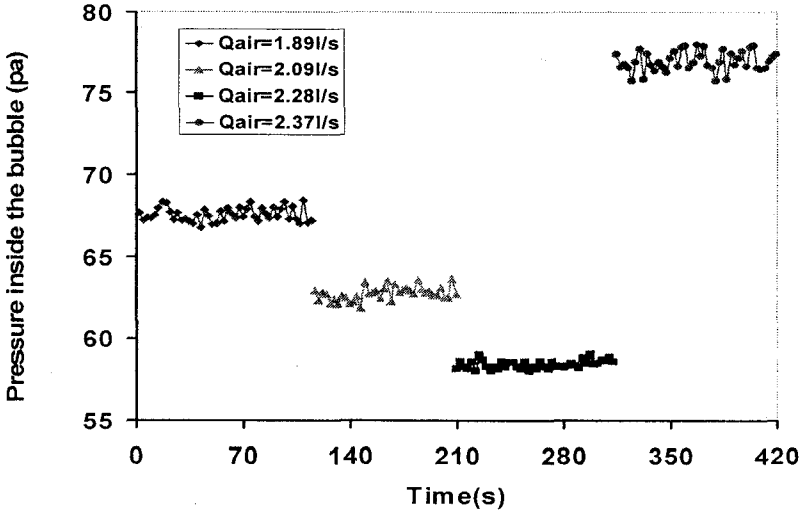

Figure 20. Pressure profiles inside the bubble (BUR=1.75, TUR=30)

The bubble instabilities depend on a strong level of interaction between various process parameters including TUR, BUR, and the cooling air flow rate used. This is most likely due to the effect, the different factors and interactions have on the momentum transfer from the cooling air to the polymer film, and on the heat transfer from the polymer film to the cooling air. The static pressure numerically along the bubble surface was used for the analysis of the momentum transfer influence on the bubble instability, which was shown that the bubble instabilities depend on the static

pressure distribution along the bubble surface, and that minimizing the pressure gradient can stabilize the bubbles. This result was obtained under the conditions of a fixed TUR and a constant amount of inflation air for different BURs. For different TURs, the difference in static pressure numerically along the surface between the stable and unstable (i. e. 2.5% of radius variation) bubble for a BUR of 1 are presented in Figure21. Certain general trends in the data are clear; From a TUR of 20 to 40, the bubble with the high TUR shows a smaller variation of pressure, resulting in less susceptibility to instability induced by aerodynamics acting on the surface of the bubble. After a TUR of 40, a smaller difference in the static pressure was obtained with the increasing of TUR. This can be simply explained by noting that the film thickness (see table 4 and the same results for a BUR of 2) turns to be a key influencing factor for the bubble instability, when the thickness reduction is at a certain value. Similar results were obtained by Yeow (1976), who predicted that the film blowing process is always stable unless the thickness reduction is larger than 10^4. At a BUR higher than 1, static pressure distribution of a stable bubble at high TUR produces instability at the lower TUR, (at the same static pressure distribution, the bubble is stable at the high TUR, however instable at the lower TUR) implying that the bubble with a high TUR is capable of sustaining greater force caused by the aerodynamics acting on the surface of the bubble. Since the shape of the bubble is determined by the air cooling rate, under these circumstances, increasing the TUR broadens the possible operating conditions in the range of a stable operation.

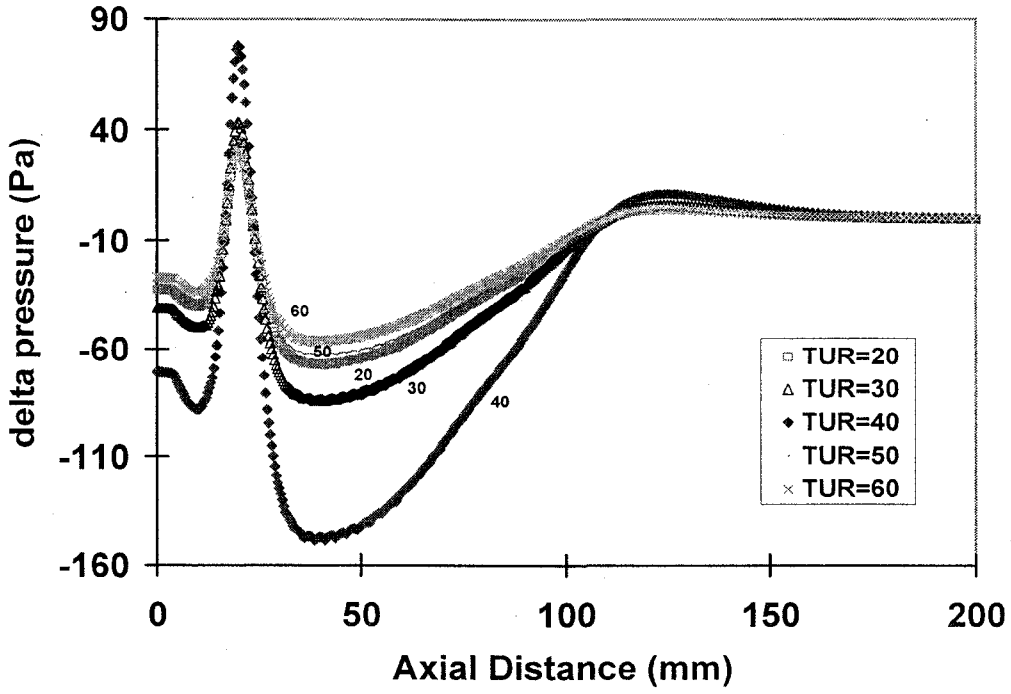

Figure 21.Delta pressure profiles around bubble surface at different TUR (BUR=1)

In the present work, a well known fact was also verified. Namely, there is a relationship between the aerodynamic force's influence on heat transfer and on bubble instabilities; gains made in one area reduce the effectiveness in the other. The effect of heat transfer between the polymer film and the cooling air is speculated to be the contribution to the re-instability after the minimum internal pressure was attained as seen in Figure18. The radius of the bubble is increasing somewhat with the almost same shape when the increasing of air flow rate from 2.28 to 2.37l/s, and such a slight changing in radius produces significant effect on the aerodynamics of cooling air. Figure 22 presents corresponding heat transfer coefficient profiles along the bubble surface obtained from the numerical analysis. It can be seen that, the heat transfer coefficient was higher when the air flow rate was set at 2.28l/s than at 2.37l/s inside the air-ring ($z \leq$ 90mm), resulting in an increased temperature of the polymeric film. Since the heat

transfer happened mainly inside the air-ring (see Figure 22), the temperature inside the bubble increased. This is the reason why the average internal pressure of the bubble is re-increased for an air flow rate of 2.37l/s. Increasing the film temperature caused an increase in radius variations. This result is in agreement with the observation of Han and coworkers (1975 and1977).

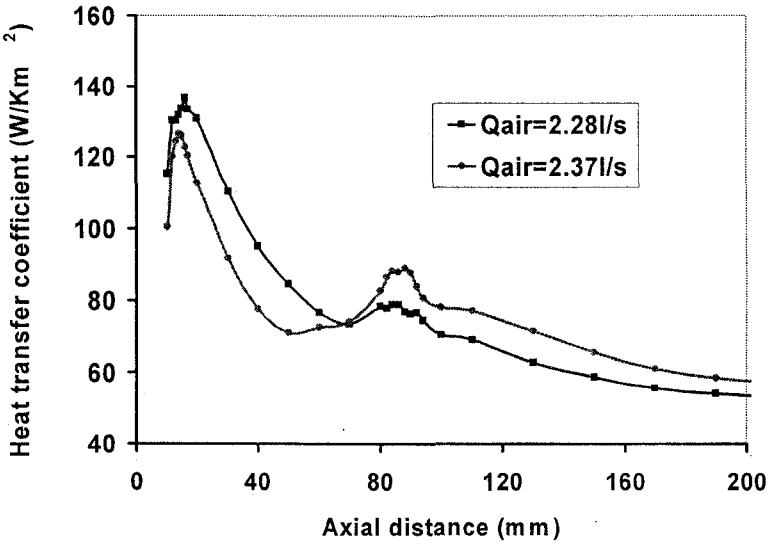

Figure 22. Heat transfer coefficient at different air cooling rate used

4.4 Nomenclature for chapter4

$$y^+ = \frac{y}{\mu_{mol}}\sqrt{\rho\tau_w}$$

y: the distance from the wall to the cell center

τ_ω: the wall shear stress.

μ_{mol}: molecular viscosity,

ρ: density of air

Vmax: Maximum velocity

Q: air flow rate

h: heat transfer coefficient

p: static pressure

Δp: gradient of pressure gradient

z: axial distance

k: kinetic energy of turbulence

ε : dissipation rate

a, b: constant

Re: Reynolds number

Nu: Nussult Nusselt number

ΔR: radius variation

R_r:, observed radius

R_s:set radius

CHAPTER 5

CONCLUSIONS AND RECOMMENDATIONS

5.1 Concluding Remarks

In the field of blown film technology, despite the rapid progress made in the technological development of materials, equipment and advances in modeling, the design and operation of the bubble cooling system is still an empirical process. The effects of aerodynamics on the blown film process are still not well understood because of the complexity of the process, experimental difficulties in measurement of relevant variables, and lack of relevant on-site data required for the numerical analysis. The present work proposes a methodology which can be used to achieve a better understanding and validation of the bubble cooling system, in the blown film process. The conclusions of the work in this dissertation are highlighted below.

The dual lip air-ring simulation suggest that a relationship between the heat transfer coefficient and the maximum velocity, like the one proposed in the literature ($h = aV_{max}^{b}$), is good outside the air-ring at low BURs. No simple correlation, however, could be used inside the air-ring to improve the die design by predicting the flow and heat transfer. Different bubble shapes at the same BUR produced significant differences in the air flow pattern and heat transfer coefficient. Vortices inside the air-ring could reduce the heat transfer rate. The heat transfer coefficient was higher for long neck bubbles inside the air-ring, and lower outside the air-ring, because of the Venturi effect.

Comparing the numerically obtained characteristics and performance of flow, produced by both single- and dual lip air-rings, at different processing conditions, show

significant differences. A dual lip air-ring spreads the heat transfer over a broad area on the bubble surface. A single lip air-ring, on the other hand, concentrates its cooling action inside the air-ring, subsequently, most of the film deformation occurs at a reduced film temperature. The predicted results also illustrate that the boundary conditions led by the airflow rate have a significant influence on the heat transfer rate. The cooling jet flow on the bubble surface moves downstream with a variation in the Reynolds number. The Nusselt number inside the air-ring depends on Re^n, the correlation between them is independent of the BUR, and the air-ring settings. Such a simple correlation could be used to improve the die design, by predicting the flow behavior and the heat transfer inside the air-ring.

The bubble instability depends on many parameters in the film blowing process with the aerodynamic forces being one of them. The combination of experimental measurements and numerical simulations indicated that the cooling rate plays a predominant role in the dynamics of bubble instabilities, for different Blow-Up-Ratios and Take-Up-Ratios. Increasing the cooling rate can destabilize the low BUR bubbles, but stabilize the high BUR ones due to the formation of different bubble shapes. Bubble instabilities depend on the static pressure distribution along the bubble surface, and minimizing the pressure gradient can stabilize the bubbles. Different bubble shapes, produced by different cooling rates, showed important differences in dynamics of bubble instability, for a constant BUR. Bubbles with high TUR sustained more force caused by the aerodynamics acting on the bubble surface, resulting in a broader range of stable operation. Additionally, a good correlation between the bubble instability and the pressure inside the bubble has been obtained.

In the present work, a well known fact was also verified. Namely, there is a balance between the aerodynamic force acting on the heat transfer and on bubble instabilities; gains made in one area reduce the effectiveness in the other. This gives a

partial explanation to why an increase in product output can not be achieved simply by accelerating the flow rate of the cooling air.

5.2 Recommandations for future work

1. Most air-cooling processes have been, predominantly, based on empirical correlations requiring expensive and time-consuming testing. Detailed models and numerical simulation provides a possibility to understand the performance of flow, the relative importance of various film blowing cooling system and mechanisms when the airflow is considered turbulent. At the present time, the validation of the simulation results is based on the evaluation of the maximum air velocities around the bubble surface. For future work, we propose carrying on an extensive study to validate the modeling, by comparing the CFD (Computational Fluid Dynamics) and the EFD (Experimental Fluid Dynamics) results, as follows:

- To use, non-intrusive, accurate Laser Doppler Velocimetry (LDV) and Particle Image Velocimetry (PIV) measurement techniques to capture the global structures in the flow field instantaneously and quantitatively, for experimental validation of the simulation results.
- Comparing the experimental with the simulation results predicted by the k-ε model and other turbulent models (e.g. a model sensitive to flow separation, k-ω-based SST model), in order to obtain a more effective theoretical description of air-cooling in the film blowing process.

2. The bubble instabilities are strongly influenced by TUR, BUR bubble geometry and air cooling flow rate. In this present work, the effect of air cooling on the bubble instabilities at various processing conditions has been investigated. A more detailed study on the issue, using graphical 3-D approach with TUR, BUR and air cooling flow rate may help increase our understanding of the subject.

3. Model developed can be extended to analyze non-axisymmetric instabilities. In order to do this, Radius, R in the parameterization should be a function of both MD and AD. Using a non– axisymmetric analysis, helical instability and other modes of bubble collapse can be studied

REFERENCES

1. Akaike, O., Tsuji, T., and Nagano, Y., "Simulation Of Blown Film Process Taking Account Of Cooling air Effect", International Polymer Processing, XIV p168, (1999)
2. Ast, W., "Extrusion Von Schlauchfolien. Theoretische Und Experimentale Unter-suchungen des Abkuhlvorgandes", Ph. D. thesis, IKT Stuttgart, (1976)
3. Butler, T.I., and Patel, R. P. "Blown Film Bubble Forming and Quenching Effects on Film Properties", TAPPI PL&C, p409, (1992)
4. Butler, T.I., Lai, S., Patel, R. P. and Spuria, J. E., " Blown Film Frost Line-Freeze Line Interactions", SPE ANTEC Tech. Papers, p15, (1994)
5. Butler, T. I., " Blown Film Bubble Instability Induced by Fabrication Conditions", SPE ANTEC Tech. Papers, 1, p156, (2000)
6. Cain, J. J., and Denn, M. M., "Multiplicities and Instabilities in Film Blowing", Polymer Engineering and Science. 28, p1527, (1988)
7. Campbell, G., Obot , N., and Cao, B., "Aerodynamics in the Blown Film Process", Polymer Engineering and Science, n32, v11, p751, (1992)
8. Cao, B., "Application Of Phase Space Kinetic Theory to Polydisperse Polymer Melts", PhD thesis, Clarkson University, Potsdam, NY, (1984)
9. Cao, B., and Campbell, G, "Air-ring Effect on Blown Film Dynamics", International Polymer Processing, IV, p114, (1989)
10. Cao, B., Sweeney, P., and Campbell, G. A., "Simultaneous Surface and Bulk Temperature Measurement of Polyethylene during Film Blowing", Journal of Plastic Film and Sheeting, v6, p117, (1990)
11. Cao, B. and Campbell, G. A., " Viscoplastic-Elastic Modeling of Tubular Blown Film Processing", AIChE Journal 36, p420, (1990)
12. Debbaut, B., Goublomme, A., Homerin, O., Koopmans, R., Liebman, D., Meissner, J., Schroeter, B., Reckmann, B., Daponte, T., Verschaeren, P., Agassant, J. F., Vergnes, B., and Venet, C., " Development of High Quality

LLDPE and Optimized Processing for Film Blowing", International Polymer Processing, XIII, p262, (1998)

13. Durst, F., Martinuzzi R., Sender, J., and Thevenin, D., "LDA Measurements of Mean velocity, RSM value, and Higher-order Moments of Turbulence Intensity Fluctuations in Flow Fields with Strong Velocity Gradients", In Pro. Sixth Intl Symposium on LDA, Lisbon, Portugal, p5.1.1, (1992)
14. Faitweather, M., and Hargrave, G. K., "Experimental Investigation of an Axi-symmetric, Impinging Turbulent Jet. 1. Velocity field; Experiments in fluids, 33, p464, (2002)
15. Fluent Inc., "Fluent User's Guide", Version 6.1 (1998)
16. Fluent Inc., "Gambit Use's Guide", Version 2.1 (1998)
17. Freon, B., Wolf, D. and Wortberg, J., "Optimized Cooling and Gauge Tolerances in Blown Film Extrusion", Polymer Engineering and Science, v37, n5, p876 (1997)
18. Han, C. D. and Park, J. K., "Studied on Blown Film Extrusion: II Analysis of the Deformation and Heat Transfer Process", Journal of Applied Polymer Science, v19, p3277, (1975a)
19. Han, C. D. and Park, J. K., "Studied on Blown Film Extrusion: I Experimental Determination of Elongational Viscosity,", Journal of Applied Polymer Science, v19, p3257, (1975b)
20. Han, C. D. and Park, J. K., "Studied on Blown Film Extrusion: III Bubble instability", Journal of Applied Polymer Science, v19, p3291, (1975c)
21. Han, C. D., and Shetty R., " Melt Strength and Film Bubble Instability of LEPD/LLDPE Blends", Ind. Eng. Chem. Fundam., 16, p49, (1977)
22. Han, C. D., and Kwack, T. H., "Rheology-Processing-Properties Relationships in Tubular Blown Film Extrusion, II High Pressure Low-Density Polyethylene", Journal of Applied Polymer Science, v28, p3399, (1983)

23. Hauck, J., and Michaeli, W., "Investigation into the Cooling Characteristics of Blown Film Extrusion Lines", Journal of Reinforced Plastics and Composites, v18, n10, p895, (1999)
24. Huang, T. A., "Instrumentation Development for Sensing Models of Bubble Motion of a Blown-Film Process", Advances in Polymer Technology, v8, n1, p65, (1988)
25. Huck, N. D., and Cleg, P. L. "The Effect of Extrusion Variables on the Fundamental Properties of Tubular Polyethylene Film", Plastics, London, 26, p114, (1961)
26. Incropera, F. P. and DeWitt, D .P., "Fundamental of Heat and Mass Transfer", 2nd ed., New York : Wiley, (1985)
27. Gamache, E., Agassant, J-E., Demay, Y., and Lafleur, P.G., PPS-20 (2004)
28. Gamache, E., "Evaluation de la Birefringence en Ligne et Modelisation du Procede de Soufflage de Gaine Multicouche" : PhD thesis, Ecole Polytechnique de Montréal, (2005)
29. Gao, N., Li, S., and Ewing, D, " Investigation of the Cooling Jets Used in the Blown Film Manufacturing Process", Proceeding of International Mechanical Engineering Congress, p473, (2003)
30. Gao, N., Li, S., and Ewing, D, " Investigation of the Cooling Jets Used in the Blown Film Process", International Polymer Processing XX, p68, (2005)
31. Ghaneh-Fard, A., "Study of the Film Blowing Process and on-line Measurements of Birefringence", Ph.D. Thesis, Ecloe Polytechnique de Montreal, Canada, (1996)
32. Ghaneh-Fard, A., Carreau, P. J., and Lafleur, P .G., " Study of Instabilities in Film Blowing", AICHE, Journal, v.42, n5, p1388, (1996)
33. Ghaneh-Fard, A., Carreau, P. J. and Lafleur, P. G., "Study of Kinematics and Dynamics of Film Blowing of Different Polythylenes", Polymer Engineering and Science, 37(7) p1148 (1997)

34. Ghijsels, A., Ente, J. J. S. M., and Raadsen, J., "Melt Strength Behavior of PE and its Relation to Bubble Stability in Film Blowing", International Polymer Processing, V, p284, (1990)
35. Gregory, A., Campbell, N., Sara, G., Campbell, W. and Burl, L., " An Investigation into the Cooling of Blown Film", SPE, ANTEC Tech. Papers p49, (2003)
36. Gregory, M., "Feature Article: Air-rings-Make Them Work for You, Not Against You" Plastics Technology, online http://www.ptonline.com/articles/199904fa3.html, (1999)
37. Gupta, R.K., "A New Non-Isothermal Rheological Constitutive Equation and its Application to Industrial Film Blowing Process", Ph.D. thesis, Dept. of Chemical Engineering, University of Delaware, Newark, (1980)
38. Gupta, R. K., Metzner, A. B. and Wissbrun, K. F., " Modeling of Polymeric Filml-Blowing Process", Polymer Engineering and Science, 22 p172, (1982)
39. Kamal, M., "Processing-Structure-Property Relationships in Polyolefin Films" Polymer Technology Symposium: Polymer films and fibers, p7, (2002)
40. Kanai, T. and White, J. L., "Kinematics, Dynamics and Stability of the Tubular Film Extrusion of Various Polyethylene", Polymer Engineering and Science, 24 p1185, (1984)
41. Kanai, T. and White, J. L., "Dynamics, Heat transfer and Structure Development in Tubular Film Extrusion of Polymer Melts: A Mathematical Model and Predictions", Journal of Polymer Engineering, 5 p136, (1985)
42. Khonakdar, H. A., Morshedian, J., and Nodehi, A. O., "Mathematical and Computational Modeling of Heat transfer and Deformation in Film Blowing Process", Journal of Applied of Polymer Science, v86, p2115, (2003)
43. Kim, S., Fang, Y., Lafleur, P. G., and Carreur P. J., "Dynamics and Criteria for Bubble Instabilities in a Single Layer Film Blowing", Polymer Engineering and Science, v44, n2, p283, (2004)

44. Knittel, R., "A Review of the Blwon Film Process", SPE ANTEC Tech. Papers, p92, (1996)
45. Laffague, J., Parent, L., Lafleur, P. G., Carreau, P. J., Demay, Y. and Agassant, J. F.," Investigation of Bubble Instabilities in Film Blowing Process", International Polymer Processing, XVII , p347, (2002)
46. Lam, S. H., " On the RNG Theory of Turbulence", Physics Fluids A, 4, p1007, (1992)
47. Liu, C. C., Bogue, D. C., and Spruiell, J. E., "Tubular Film Blowing part1. On-line Experimental Studies", International Polymer Processing, X, p226, (1995)
48. Luo, X., and Tanner, R., " A Computer Study of Film Blowing", Polymer Engineering and Science, 25, p620, (1985)
49. Menges, G., and Predohl, W. O., " Certain Aspects of Film Blowing of Low-Density Polyethylene" , Polymer Engineering and Science v15, n5, p394, (1975)
50. Menter, F. R., "Two-equation Eddy-viscosity Turbulence Models for Engineering Applications", AIAA Journal, v.32, n.8, p1598, (1994)
51. Micic, P., Bhattacharya, S. N. and Field, G., " Transient Elongational Viscosity of LLDPE/LDPE Blends and its Relevance to Bubble Stabiltiy in the Film Blowing Process", Polymer Engineering and Science, v38, n10, p1685, (1998)
52. Minoshima, M. and White, J. L., "Instability Phenomana in Tubular Film and Melt Spinning of Rheologically Characterized HDPE, LDPE, LLDPE", Journal of Non-Newtonian Fluid Mechanics, v19, p275, (1986)
53. Moore, "An Analysis of the North American Plastic Film Business", Plastics Information Direct online http://www.amiplastics.com/ami/pidproduct.asp?pf_id=PC02&dept_id=210 (2003)
54. Nagarajan , G., and Campbell, G. A., " Experimental Determination of Heat Transfer Coefficient in Blown Film Process", : SPE ANTEC Tech. Papers, p162, (1995)

55. Obijeski, T. J., and Pruitt, K. R., "Improving the Output and Bubble. Stability of Thick Gauge Blown Film", SPE ANTEC Tech. papers, p150, (1992)
56. Pearson, J. R. A., "Mechanical Principles of Polymer Processing", Pergamon, Oxford, (1966)
57. Pearson, J. R. A, and Petrie, C. J. S., "A Fluid Mechanical Analysis of the Film-Blowing Process", Plastics &Polymers, p85, (1970a)
58. Pearson, J. R. A, and Petrie, C. J. S., "The Flow of a Tubular Film. Part1. Formal Mathematical Representation", Journal of Fluid Mechanics, 40, p1, (1970b)
59. Pearson, J. R. A, and Petrie, C. J. S., "The Flow of a Tubular Film. Part2. Interpretation of the Model and Discussion of Solutions", Journal of Fluid Mechanics, 42, p609, (1970c)
60. Petrie, C. J. S., " Mathematical Modeling of Heat Transfer in Film Blowing", Plastics and Polymers, v42, p259, (1974)
61. Petrie, C. J. S., "A comparison of Theoretical Predictions with Published Experimental Measurements on the Blown Film Process", AIChE Journal, 21, p275, (1975)
62. Petrie, C. J. S. " Tubular Film Blowing – Myths and Science", Online, http://citeseer.ist.psu.edu/626099.html , (2002)
63. Sidiropoulos, V., "Comparison of Experiments with a Model Of the Blown Film Process", Master Thesis, MaMaster University, Hamilton, Canada, (1995)
64. Sidiropoulos, V., Tian, T. T., and Vlachopoulos, J, "Computer Simulation of Film Blowing", TAPPI Journal v79, n8, p113, (1996)
65. Sidiropoulos, V., and Vlachopoulos, J., " The Aerodynamics of Cooling of Blown Film Bubbles", : SPE ANTEC Tech Papers part 1(of 3), p108, (1998)
66. Sidiropoulos, V., Wood, P.E., and Vlachopoulos, J., " The Aerodynamics of Cooling of Blown Film Bubbles", Journal of Reinflorced Plastics and Composites, 18, p529, (1999)

67. Sidiropoulos, V., and Vlachopoulos, J., "The Effect of Dual-Orifice Air-ring Design on Blown Film Cooling", Polymer Engineering and Science, v40, n7, p1611, (2000)
68. Sidiropoulos, V., and Vlachopoulos, J., " An Investigation Of Venturi and Coanda Effect in Blown Film Cooling", International Polymer Processing XV, p40, (2000)
69. Sidiropoulos, V., and Vlachopoulos, J., "Numerical Study of Internal Bubble Cooling (IBC) in Film Blowing", International Polymer Processing XVI, p48, (2001)
70. Sidiropoulos, V., and Vlachopoulos, J., "The Aerodynamics of Cooling of Blown Film Bubbles", Journal of Reinflorced Plastics and Composites. v21, n7, p629, (2002)
71. Sidiropoulos, V., and Vlachopoulos, J., " Temperature Gradients in Blown Film Bubbles", Advances in Polymer Technology, v24, n2, p83, (2005)
72. Simpson, D., and Harrison, I., " The Use if Deformation Rates in the Scale-up of Polyethylene Blown Film Extrusion", Journal of Plastic Film & Sheeting, v8, p192, (1992)
73. Strater, K. F., and Dealy, J. M, "Two-way Air Flow Boots Blown-film Cooling", Plastics engineering, Oct., p37, (1985)
74. Strater, K. F., and Dealy, J. M., "Countercurrent Cooling of Blown Film", Polymer Engineering and Science v27, n18, p1380, (1987)
75. Sweeney, P. A., and Campbell, G. A., " Real Time Video Techniques in the Analysis of Blown Film Instabiltiy", International Polymer Processing, VII, p229, (1992)
76. Sweeney, P. A., and Campbell, G. A., " Blown Film Stability", SPE ANTEC Tech. papers, p146, (1993)
77. Tanner, R. I., "Engineering Rheology", Claredon Press, Oxford , (1985)
78. Tas, P. P. "Film Blowing: From Polymer to Product", Ph.D.Thesis, Dept. Mech. Eng. Eindhoven University of Technology, The Netherlands., (1994)

79. Vlachopoulos, J., "The Symbol of Excellence in Blown Film", Modern Plastics, May p43, (2001)
80. Wagner, M. H., "Ein Rheologisch-Thermodynamisches Prozessmodell Des Folien-Blasverfahrens", Ph.D. Thesis, IKT Stuttgart, (1976)
81. Waller, P., "Extrusion Troubleshooter: What to Do When the Bubble Won't Behave", Plastics Technology, online http://www.ptonline.com/articles/200212ts1.html, (2002)
82. White, J. L. and Yamane, H., " Rheological Investigation of Molecularly Characterized Commercial High Density, Low Density and Linear Low Density Polyethylene Melts", Pure and Applied Chemistry., 59(2), p193, (1987)
83. Wilcox, D. C., "Reassessment of the Scale Determining Equation and Advanced Turbulence Models", AIAA Journal, v.26, n11, p1299, (1988)
84. Winter, H. H., "A Collaborative Study on the Relation Between Film Blowing Performance and Rheological Properties of Two Low-Density and Two High-Density Polyethylene Samples", Pure & Appl. Chem., 55(6), p934, (1983)
85. Wolf, D., Feron, B., and Wortberg, J., "Numerical Analysis of Cooling Air Systems in Film Blowing", International Polymer Processing, XII, p38, (1997)
86. Wortberg, J., and Spirgatis, J., "Experimental and Numerical Studies of Blown Film Cooling", SPE, ANTEC Tech. Papers, p210, (2004)
87. Yakhot, V., Orszag, S. A., "Renormalization Group Analysis of Turbulence, 1. Basic Theory", Journal of Science Computing. v1, p3, (1986)
88. Yeow, Y. J.: "Stability of Tubular Film Flow: A Model of the Film-blowing Process", Fluid Mech. 75, p577, (1976)
89. Yoon, K. S., and Park, C. W., "Stability of a Blown Film Extrusion Process", International Polymer Processing , XII, p342, (1999)
90. Zippenfeld, T., " Possibilities for Increasing Production from Air Cooled Film Blowing Equipment", Kunstsoffe, 16, p147, (1971)

APPENDICES

APPENDIX A: STUDY ON AERODYNAMICS OF COOLING IN FILM BLOWING

Conference paper-ANTEC 2005

Zhijie Zhang and P.G. Lafleur
Ecole Polytechnique de Montréal, CREPEC, Canada

Abstract

A numerical analysis using a renormalization group (RNG) k-ε model and Fluent software was performed on the air ring cooling system of the film blowing process. The calculations were in a good agreement with the experimental results to predict maximum air velocities along the bubble surface at different axial distance from the die. Outside of the air-ring, the simulation results indicated that the heat transfer coefficient function of the form, $h = aV_{max}^{b}$, is adequate mostly at low Blow-Up-Ratio (BUR). Different bubble shapes, for the same BUR, produced significant differences in the air flow pattern as well as heat transfer coefficient. In this work we want to study the correlation between thermal inertia and aerodynamics of cooling air under different bubble geometry.

Introduction

The air cooling system is an integral part of any tubular film extrusion line. Since the cooling power is limiting the polymer mass throughput, increasing airflow rate seems to be a good way to increase the final production rate. However, the properties of the film can be affected by a strong acceleration of the airflow around the bubble. Therefore, a major goal is the improvement of the air-cooling efficiency by studying the relationship between heat transfer and aerodynamics of cooling air.

Because the typical Reynolds number based on the air ring clearance and air velocity exceeds 10^4 [1], the cooling air surrounding the bubble gives rise to very complex turbulent flow, which is always time and space dependent with a very large number of spatial degrees of freedom. Several correlations have been proposed in the literature [2,3] for the evaluation of the heat transfer coefficient based on experimental results. Cao and Campbell [4,5] addressed the problem by introducing a full aerodynamic analysis (momentum and heat transfer) on the cooling air by using the method of superposition of stream functions as well as mass and energy balances. Wolf et al. [1] extended Campbell's [5] work by using the finite element method and a standard k-ε turbulent model to predict air flow for jets impinging on the blown film bubble. Sidiropoulos et al. [6, 7, 8] carried out numerical simulations of aerodynamics for cooling air in the blown-film processing with RNG k-ε turbulent model and commercial software (Fluent), in

their papers they also recognized the importance of Verturi and Coanda effects around the bubble in predicting the aerodynamics of cooling air. More recently, Campbell et al. [9] developed a relatively simple model to maximizing the heat transfer coefficient as the bubble expands.

Very few comparisons between experimental data and full aerodynamic numerical analysis simulation were reported in the literature. The primary objective presented in this paper is a detailed experimental investigation of the cooling-air velocity around the bubble with a conventional hot wire anemometer. The simulation results, using the RNG k-ε model with special wall treatment and commercially available software package (FLUENT), are shown and compared with the experiments. Also shown is the detailed simulation of heat transfer and aerodynamics during processing of different bubble shapes at the same BUR.

Experimental and simulation methodology

An experimental setup has been developed in our lab, which consists of a 45mm Killion single screw extruder with a helical film die (D_0 = 63.5mm, h_0 = 1.5mm with double lips). LDPE with some particular characteristics was used in this study. The determination of the air velocity was carried out with a FMA-905-V hot wire anemometer and bubble diameter profile was determined by video camera. The temperature at the bubble surface as a function of vertical distance from the die was measured by an infrared-pyrometer (IRCON 3400). Dual orifice air-ring was used to study the aerodynamics.

For the calculation of the aerodynamics around the bubble, Fluent software was used with the RNG k-ε model coupled with wall treatment. A no-slip boundary conditions was considered at the bubble surface with a fixed experimental temperature profile. The bubble shape and the frost line height were set according to the experiments. The ambient temperature was set to 25°C.

The cooling air enters the computational domain with a certain velocity, kinetic energy of turbulence (k), dissipation rate (ε) and temperature value. Kinetic energy (k) and dissipation rate (ε) were evaluated empirically [10, 11]. The errors introduced by these parameters into the simulation by the k- ε model, on the mean velocity flow pattern, were found to be insignificant. A sensitivity analysis shows that the mean flow velocity will exhibit changes of the order of 3% when varying k and ε. Fokema et al. [12] also confirmed this lack of sensitivity of the mean flow.

Results and Discussions

Fig.1 shows simulation and experimental results for air velocity distribution around the bubble at different height from the die for a BUR of 2.28. The predictions are in good agreement near the air-ring where the maximum experimental air velocity is 3.34 m/s at

a distance of 8.7 mm from the bubble surface and the calculated one is 3.35 m/s at a distance of 9.5 mm. Maximum velocities are reported in the literature at a distance of 5 mm from the bubble surface. The velocity distributions show the same trend and a good agreement between the simulations and the experiments.

Away from the surface of the die both measured and calculated velocity show a decrease in the maximum values but an increase of air velocity at higher distances from the bubble surface. In the simulations it was possible to locate the position of maximum velocity from the bubble surface. This was not possible with the experimental results because of the limitations of the measurement technique. The hot wire anemometry can not be used below a distance of 4 mm from the surface.

Heat transfer plays a predominantly role between bubble and cooling air on the temperature dependent rheological properties of the melt, crystallization and degree of orientation of the cooling polymer. The heat transfer coefficient is an effective parameter to describe the convective heat transfer process. The correlation ($h = aV_{max}^{b}$) has been proposed in the literature [3] for the evaluation of the heat transfer coefficient.

The numerical analysis was performed for heat transfer between bubbles and cooling air as well as velocity of cooling air around the bubble at different BUR conditions. The simulation inside the air-ring indicated that variation of maximum velocity around the bubble was independent of the heat transfer coefficient for both low and high BUR. Therefore, no simple correlation of the shape $h = a\ V_{max}^{b}$ can be used inside the air-ring to improve die design by predicting flow and heat transfer.

Outside the air-ring the maximum velocity profile exhibits the same trend as the heat transfer coefficient. The relationship is almost linear on a log\log plot. Figure 2 shows the logarithm of heat transfer coefficient versus the logarithm of maximum velocity. The regression coefficient R^2 decreases from 0.98 to 0.86 with a BUR increasing from 1 to 3, indicating a better fit for lower BUR. The same trend was reported by Gamache et al. [13].

Heat transfer coefficient profiles along the bubble surface obtained from the numerical analysis are presented in Fig.3 for three bubbles (Bubble1: long neck, Bubble3: short neck and Bubble2: intermediate). The heat transfer coefficients went up through a maximum at a location around z = 14mm and then decreased. Another smaller peak appeared on z = 90mm for Bubble2 and Bubble3, while the profile of heat transfer coefficient decreased gradually for Bubble1. Close to the air-ring, the heat transfer coefficient is the highest for bubble1 and the lowest for bubble3. Away from the air-ring the situation is reversed.

Flow pattern of cooling-air are shown in Fig.4 for the three different bubble shapes and can be used to explain variation of heat transfer coefficients. In order to get a clear view, partial zoom-in inside the air-ring at the first point of contact with the bubble are also

shown. The three shapes show vortices in the area between the bubble surface and the air-ring gate avoiding bubble instability led by the air stream from the lower lip jetting directly to the bubble surface. It is well known that the selection of air ring design always plays a critical role in determining cooling processing. However the vortex reduces the heat transfer rate and is responsible for the presence of the first heat transfer coefficient maximum at a position around 14 mm from the die exit. Velocity vector, shown in Figure 5, could also be used to provide a representation of not only direction but also magnitude of flow [14]. From the zoom-in sections we can see higher velocities near the lower-lip jet region for Bubble1 where the heat transfer was calculated to be the highest.

The second peak of heat transfer coefficient appearing in the heat transfer coefficient profile for Bubble2 and Bubble3 is due to the well-known Venturi effect. The Venturi is caused by the air accelerating from the main part of the air-ring (z = 90mm) at the gap formed by the bubble surface and the air-ring. The gap adjustment due to the bubble shape will affect the air velocity. Narrow gap (like the situation of Bubble3) tends to increase the Venturi effect by increasing the speed of air flow. This is the reason why the second peak in heat transfer coefficient was the highest for Bubble3.

Additionally, the upper lip of the air ring should inject large volumes of air, hopefully in parallel flow to the bubble surface to increase the cooling process. It was found out from Fig.5 that the speeds of air flow from the upper lip around Bubble3 was the highest explaining the high heat transfer coefficient outside the air ring.

Conclusions

A RNG k-ε model coupled with a finite element analysis (Fluent) of the aerodynamics of cooling air around the bubble in the film blown process was proposed in this investigation. The calculations were in a good agreement with the experimental results to predict maximum air velocities along the bubble surface at different axial distance from the die.

The simulations showed that a relationship between the heat transfer coefficient and the maximum velocity, like the one proposed in the literature ($h = aV_{max}^{b}$), is good outside the air-ring at low BUR.

Different bubble shapes at the same BUR produced significant differences in the air-flow pattern and heat transfer coefficient. Vortices inside the air-ring could reduce the heat transfer rate. The heat transfer coefficient was higher for long neck bubble inside the air-ring and lower outside the air-ring because of the Venturi effect.

References

1. B. Feron, D. Wolf and J. Wortberg, Polymer engineering and science, v37, n5. p 876 (1997)
2. B. Cao, P. Sweeney and G.A. Campbell, J. of plastic film ans sheeting, 6 p117, (1990)
3. G. Nagarajan and G.A. Campbell, ANTEC, p162, (1995)
4. B. Cao and G.A. Campbell, Intern. Polymer processing IV, p114, (1989)
5. G.A. Campbell, N.T. Obot and B.Cao, Polymer engineering and science, v32, n11, p751(1992)
6. V. Sidiropolos, P.E. Wood and J. Vlachopoulos, ANTEC, p108 (1998)
7. V. Sidiropolos and J. Vlachopoulos, Intern. Polymer processing XVI, p48(2001)
8. V. Sidiropolos and J. Vlachopoulos, , J. of reinforced plastics and composites, v21, n7, p629 (2002)
9. G. A. Campbell, N Ganesh, S.W. Campbell and L. Burl, ANTEC p49, (2003)
10. Fluent Inc., "Fluent User's Guide", Version 6.1 (1998)
11. Fluent Inc., "Gambit User' Guide", Version 2.1 (1998)
12. Fokema, M. D., Kresta, S. M. and Wood, P. E., Can. J. Chem. Eng. 72, 177 (1994)
13. E. Gamache, J-E. Agassant, Y. Demay and P.G. Lafleur, PPS-20 (2004)
14. T. S. Liu and J. P. Sullivan, Int. J. Heat Mass Transfer, v39, n17 p3695 (1996)

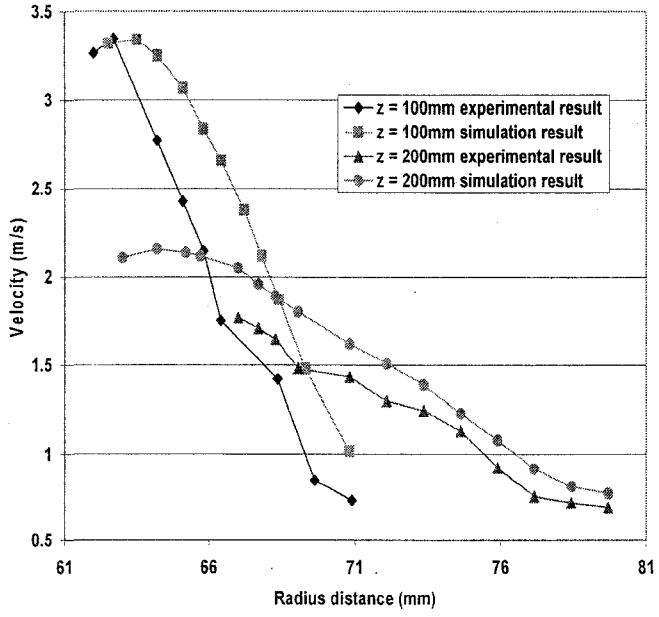

Fig.1 Comparison simulation with experimental results (BUR=2.28)

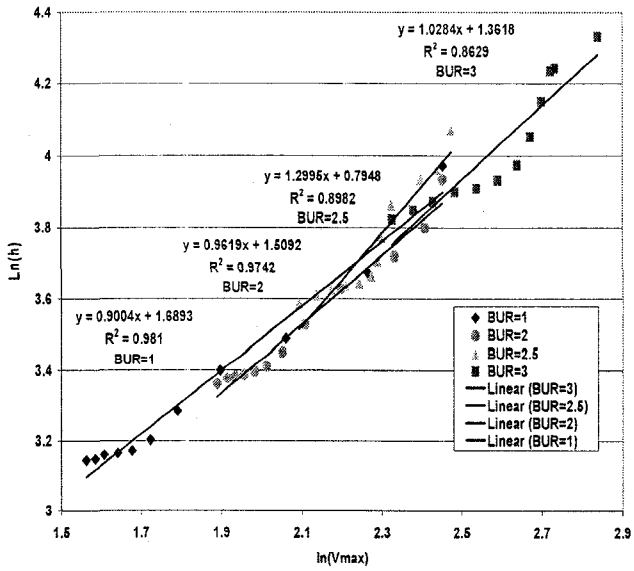

Fig.2 Linear regression ln(h) from Ln(Vmax) on the external air-ring at different BUR

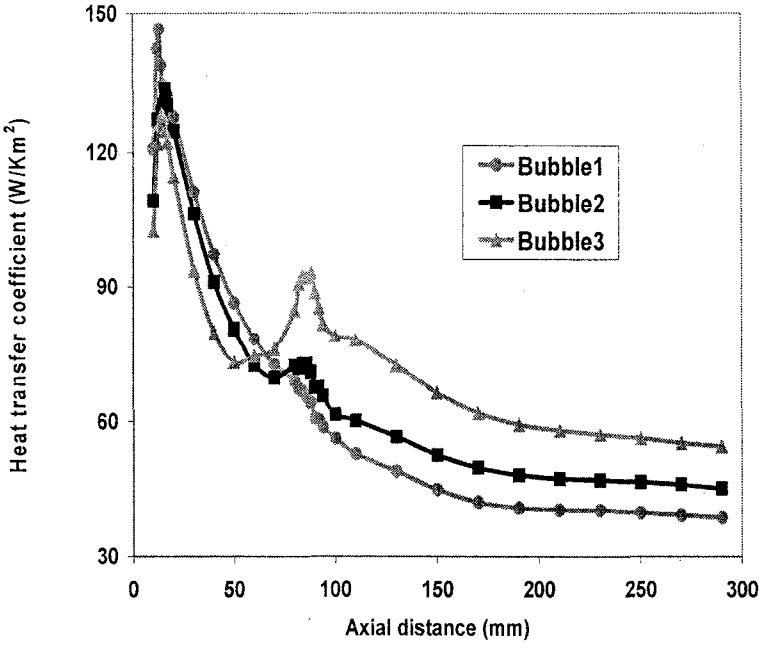

Fig.3 Heat transfer coefficient at different bubble shape (BUR=2.5)

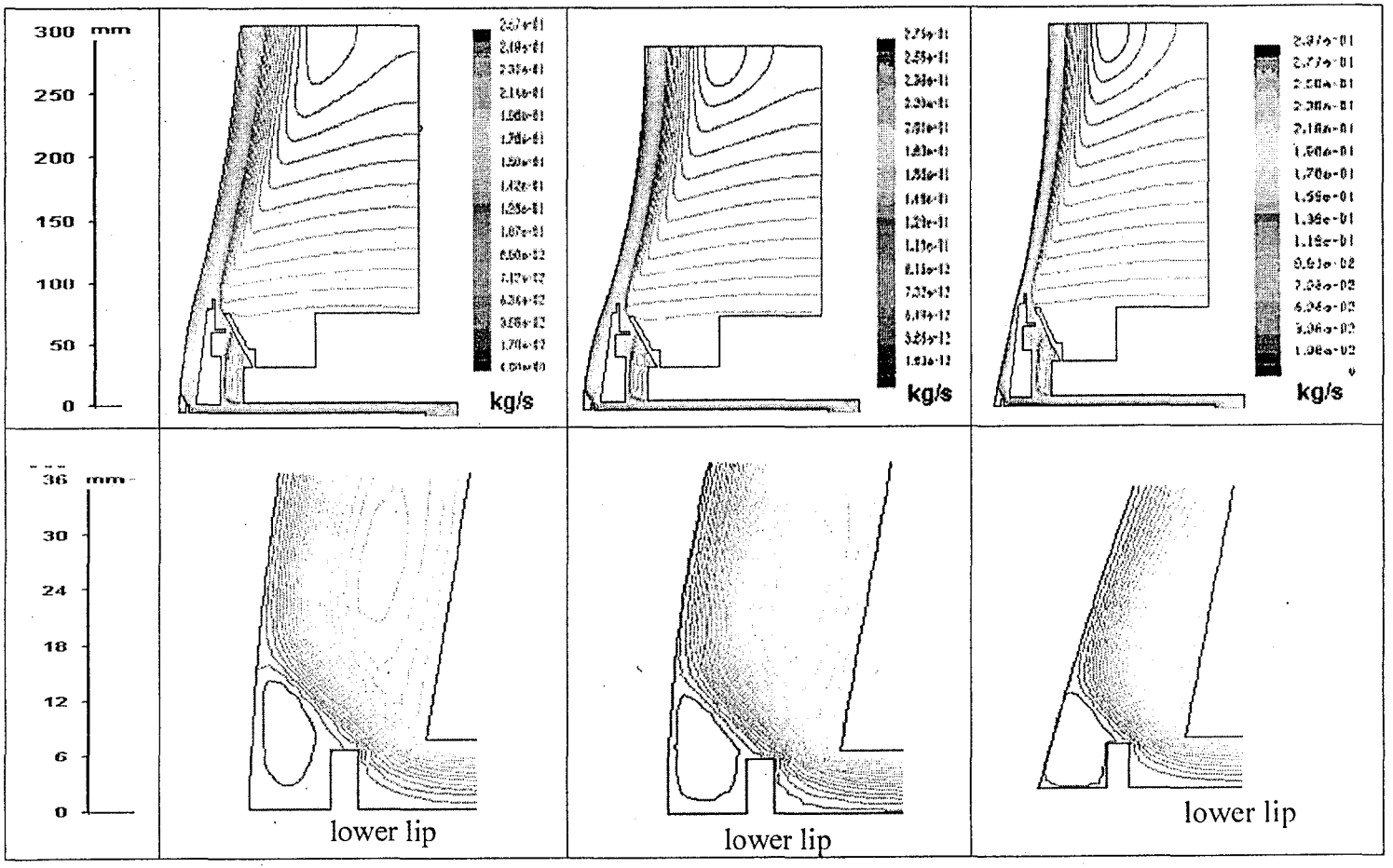

Fig 4 Cooling air streamlines and partial zoom-in of flow around different shape bubbles

(Left bubble1; middle bubble2; right bubble3)

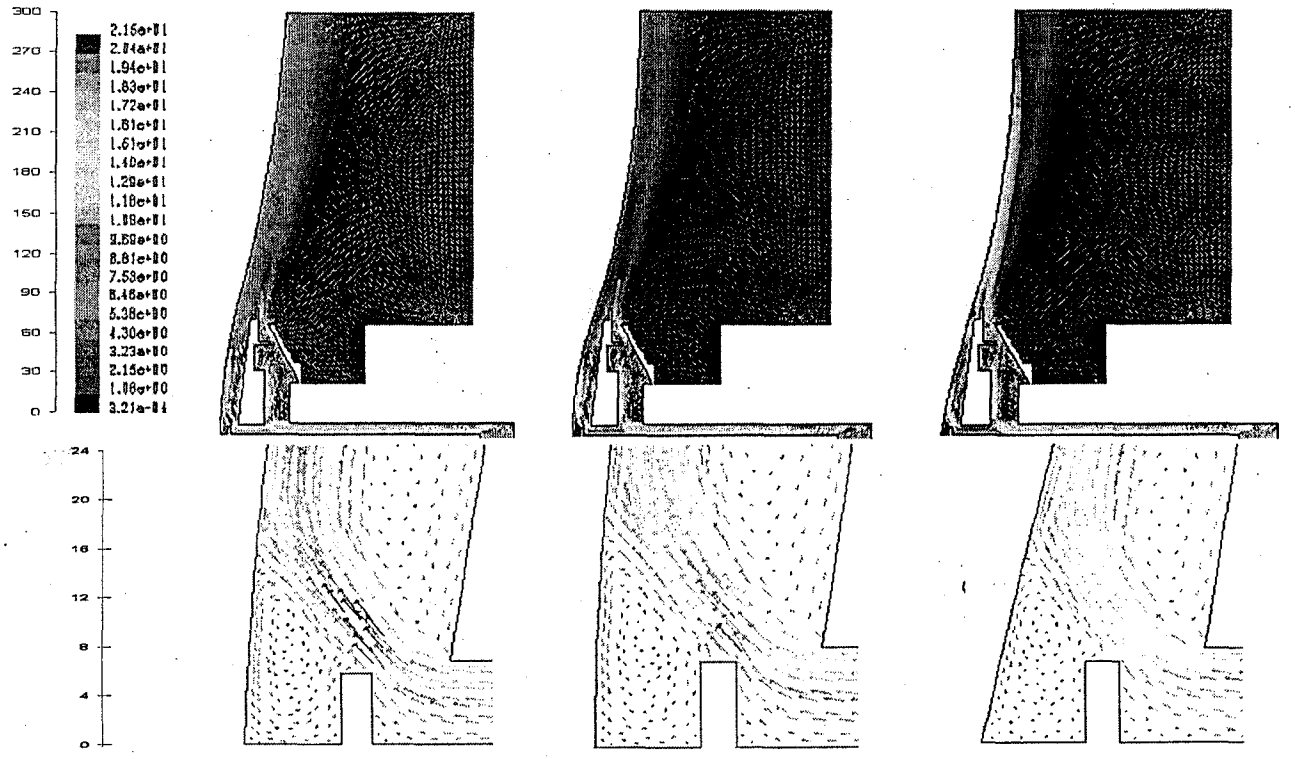

Fig.5 Velocity vector pattern and partial zoom-in of flow around different shape bubbles

(Left bubble1; middle bubble2; right bubble3)

APPENDIX B: THE EFFECT OF COOLING AIR AERODYNAMICS ON BUBBLE INSTABILITY IN BLOWN FILM

Conference paper- ANTEC 2006

Zhijie Zhang and P.G. Lafleur

Centre de Recherche En Polymères Et Composites (CREPEC), École Polytechnique de Montréal, Canada.

Abstract

A numerical analysis using a renormalization group (RNG), k-ε model and Fluent software was performed to predict the static pressure distribution around the bubble as well as the flow field of cooling air in the film blowing process. Bubble instabilities were experimentally studied using an in-line scanning camera system developed in our laboratory. The combination of experimental measurements and numerical analysis indicated that different bubble shapes led by various cooling rate produced significant differences in dynamics of bubble instability. When the gradient of static pressure along the axis of the bubble is minimized, the stability of the bubble increases.

Introduction

It is well-known that there are a number of different factors influencing bubble stability in the film blowing process. One of the key factors is the bubble cooling produced by the cooling jets exiting from the air ring. The impinging air cools the bubble reducing the temperature of the polymer from the die exit to the frost line height (FLH). At the same time, these jets also exert an aerodynamic force on the bubble surface that can either stabilize or destabilize the bubble.

One of the first studies on the shape and stability of the bubble formed in the film blowing process is the isothermal model presented by Petrie and Pearson [1, 2]. Petrie [3] later predicted the bubble shapes using a non-isothermal rheological model considering heat transfer. Yeow [4] developed a model to characterize the stability of the bubble that considered the inflation pressure and aerodynamic pressure caused by the cooling air over the bubble, and concluded that the stability of the bubble was influenced by a combination of process variables. Some research has also been done on the experimental aspects of the problem. Kanai and White [5] performed experiments to determine if

modeling could predict the shape and stability of the bubble. They found that changes of air cooling rate has a significant effect on the frost-line height, bubble shape as well as the pressure around the bubble. In 1990, Cao [6] demonstrated that the static pressure produced by the cooling jets exiting from the single-lip air rings varied locally due to the complexity of the bubble shape. The numerical investigations by Feron et al, [7] focused on the aerodynamics produced by dual-lip air rings. They noted that the occurrence of vortices led by the angle-of-attack together with the bubble shape was responsible for the unstable behaviour in the bubble. Then, Sidiropoulos and Vlachopoulos [8-10]carried out numerical simulations of aerodynamics for cooling air in the blown-film process with RNG k-ε turbulent model and a commercial software (Fluent), and published a dozen of papers to examine the flow fields produced by different dual-lip air ring settings compare to single-lip air rings. In their papers, they noted that vortices produced between the bubble and forming cone can cause a negative static pressure around the bubble, which was assumed to stabilize the bubble against the forming cone. More recently, Gao. al. [11] experimentally measured the distribution of pressure on the bubble surface for a rigid model bubble and demonstrated the existence of a negative static pressure region on the bubble surface due to the deformation of the bubble at different processing conditions. However, due to the complexity of the cooling air flow and to the absence of a device able to capture quantitatively the characteristics of bubble instabilities, there has not been a detailed investigation that correlates the bubble instability to the aerodynamics of cooling air under different processing conditions. Therefore, the objective of this work is to investigate the relationship between bubble instability and aerodynamics of cooling jets.

Experimental and simulation methodology

A 45mm Killion single screw extruder with a helical film die (D_0 = 63.5mm, h_0 = 1.5mm with double lips) was used for the production of blown films. The extrusion temperature profile was set 150/170/180/180/180 °C from the hopper to the die. LDPE with some particular characteristics was used in this study. The flow rate of polymer was maintained at 2.5 ±0.1 kg/hr. The take-up ratio (TUR) was set at 38. The dual orifice air-rings were employed in this study as schematically shown in the Fig.1. In this air-ring design, the air stream is split into a lower and an upper jet.

Bubble instabilities were experimentally studied using an in-line scanning camera system developed in our laboratory [12]. The cooling flow rate was increased or decreased gradually in order to generate unstable bubbles. Detailed dynamics of bubble instabilities was investigated as a function of time at various flow rates of the cooling air for the different bubble shapes.

Because the typical Reynolds number based on the air ring clearance and air velocity exceeds 10^4 [7], the cooling air surrounding the bubble gives rise to very complex turbulent flow. The RNG (Renormalization Group) k-ε model coupled with a specific

wall treatment was employed to achieve turbulence closure. Fluent software was used to calculate the aerodynamics variables around the bubble. No-slip boundary condition was considered at the bubble surface with a fixed experimental temperature profile. Temperatures at the bubble surface as a function of vertical distance from the die were measured by an infrared-pyrometer (IRCON 3400). The bubble shape was set according to the experiments. The bubble diameter profile was determined by video camera. The ambient temperature was set to 25°C. The cooling air enters the computational domain with a certain velocity, kinetic energy of turbulence (k), dissipation rate (ε) and temperature value. A FMA-905-V hot wire anemometer was used to measure the air velocity. Kinetic energy (k) and dissipation rate (ε) were evaluated empirically [13, 14].

Results and Discussions

Flow rate of cooling air plays a predominant role in the bubble instability. Draw resonance bubble instabilities caused by flow rate were investigated in this study. When the diameter of the bubble is similar or bigger to the one of the air ring exit, this kind of instability will take place.

Fig.2 exhibits radius and radius variation response for a Blow-Up-Ratio (BUR) of 1 at different air flow rate. When flow rate varies from 1.63 l/s to 3.61 l/s, a typical stable bubble was observed with a radius variation less than 1%. With the increasing the flow rate to 4.03 l/s, variation of radius was up to around 4 % with periodic oscillations, and exceeded the critical value of 2.5%. With another increase of 0.19 l/s, the variation of radius dramatically changed to show oscillations greater 20%. However, all the bubbles have a similar average diameter. Static pressure and gradient of pressure distributions along the bubble surface obtained from the numerical analysis are presented in Fig.3. The unstable bubble shows more pressure variation than the stable one. It is reasonable that the higher flow rate of cooling air can produce the higher pressure gradient around the bubble surface, and then destabilizes the bubble.

The situation is reversed for a bubble with the BUR of 2 as shown in Fig.4. These data were obtained at the same TUR (Take-Up-Ratio) as the previous one (BUR of 1). When the flow rate was set to 1.63 l/s, the radius variation exceeded the critical value of 2.5% with periodic oscillations. The bubble shows typical draw resonance instability with a long-neck shape. With increasing of air flow rate, the bubble shape was changed from long-neck to short-neck as shown in the Fig.5, at the same time, the radius variation decreases to around 2.5 %. The air flow rate was then increased to 2.10 l/s, stabilizing the bubble. The radii almost overlap each other with a radius variation down to 1%. A further increase of air flow rate will result in a bubble sitting down on the air ring and collapsing.

Static pressure and gradient of pressure distributions along the bubble for a BUR of 2 were obtained from the numerical analysis and are presented in Fig.6. The complexity of the aerodynamics acting on the bubble surface produces a different effect as the one

presented for a BUR of 1. Higher flow rate generated a lower static pressure gradient on the bubble surface, resulting in a stable bubble. The first peak on the pressure profile is higher for the smaller flow rate than the bigger one. Another peak appeared at z = 70 mm for the unstable bubble, while the profile of pressure increases gradually for the stable bubble. This is the reason why the unstable bubble has a long neck. The aerodynamics of cooling air determines the shape of the bubble. Varying the flow rate causes a variation of static pressure on the bubble surface, and then changes the bubble shape. As a result, the static pressure was re-distributed by changing of the bubble shape.

The part of the air stream emerging through the lower orifice is forced to travel close to the bubble surface through a flow deflector. It deflects the flow away from the bottom of the polymer bubble, where the polymer is at its melt temperature and the melt strength of the film can be influenced by the high pressure produced by a higher speed. Fig.7 shows the streamline pattern around a bubble surface with a BUR of 2 obtained from calculations. The vortex created between the flow deflector and the base of the film presented in this figure corresponds to the initial negative pressure in the static pressure profile as shown in the Fig.6. This local negative static pressure led by the vortex helps to stabilize the bubble through by avoiding high speed airflow to act on the initial stage of the bubble. The first peak of around 40Pa on the pressure distribution is not negligible compared to typical value of the bubble inflation pressure of 250 Pa. Pressure changes can not be neglected. Additionally, the acceleration due to the narrow gap between the air ring and the film produces another big vortex, which results in another negative pressure in the pressure profile. It seems that negative static pressure led by the vortex can act to stabilize draw resonance instabilities. However, the negative pressure region from z (axial distance) = 50mm to z = 90mm seems to be responsible for the bubble sitting down on the air ring.

Conclusions

The bubble instability depends on many parameters in the film blowing process with aerodynamic forces being one of them. For processing condition such as BUR=2, the complexity of the aerodynamics acting on the bubble surface produced the reversed effect as compared to one of a BUR=1 whereas increasing cooling air flow rate can minimize the pressure gradient around the bubble surface resulting in a stabilizing effect. Different bubble shapes, produced by various cooling rates, showed important differences in dynamics of bubble instability for a constant BUR bubble. The existence of a vortex can act to stabilize draw resonance bubble.

References

1. Pearson, J. R.A. and Petrie, C.J.S., J. Fluid Mechanics, 40:1, 1-19, (1970)
2. Pearson, J. R.A. and Petrie, C.J.S., J. Fluid Mechanics, 42:3 609-625, (1970)

3. Petrie, C.J.S., AIChE Journal 21 :2, 275-282 (1975)
4. Yeow, Y. L., Journal of Fluid Mechanics, v75, 577-589, (1975)
5. Kania, T. and White, J., Polymer engineering and science, v24, 1185-1201, (1984)
6. Cao, B., Ph. D. Thesis, Clarkson university, (1990)
7. Feron, B., Wolf, D. and Wortberg, J., Polymer engineering and science, 37:5 876-881, (1997)
8. Sidiropolos, V., Wood, P.E. and Vlachopoulos, J., ANTEC, 108-112, (1998)
9. Sidiropolos, V. and Vlachopoulos, J., Polymer engineering and Science, 40:7 1611-1618, (2000)
10. Sidiropolos, V. and Vlachopoulos, J., J. of reinforced plastics and composites, 21:7 629-637, (2002)
11. Gao, N., Li, S. and Ewing, D., J., Intern. Polymer processing, XX 68-77 (2005)
12. Kim, B. S., Fang, Y., Lafleur, P.G. and Carreau, P.J., Polymer engineering and Science, 44;2 283-302, (2004)
13. Fluent Inc., "Fluent User's Guide", Version 6.1 (1998)
14. Fluent Inc., "Gambit User' Guide", Version 2.1 (1998)

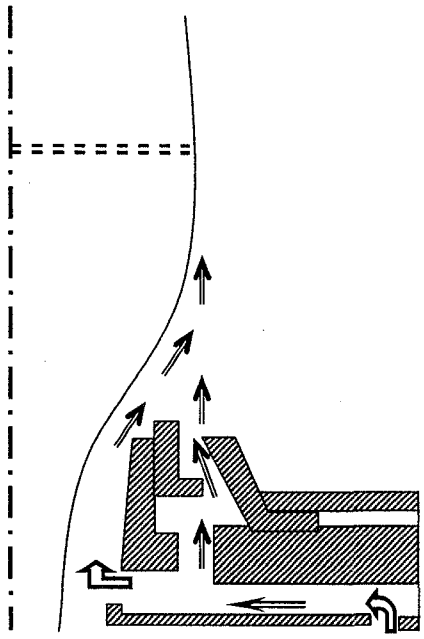

Fig.1 Schematic of dual lip air ring

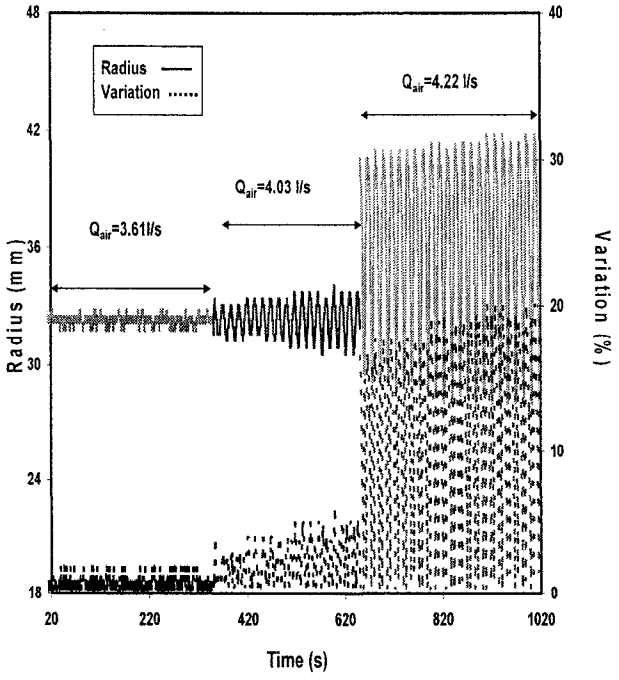

Fig.2 Radius and radius variation response at different air flow rate (BUR=1)

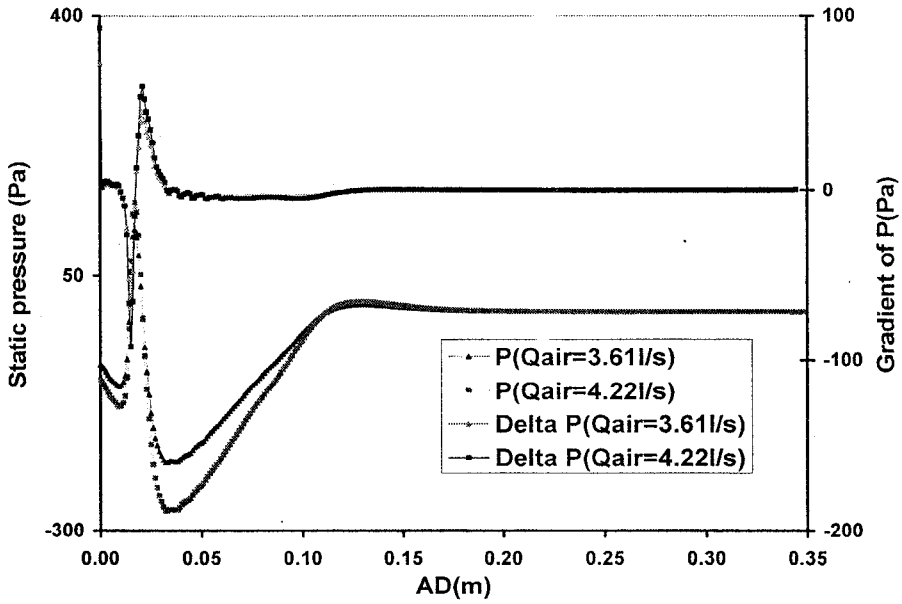

Fig.3 Gradient of pressure and pressure profile around bubble surface for different air flow rate (BUR=1)

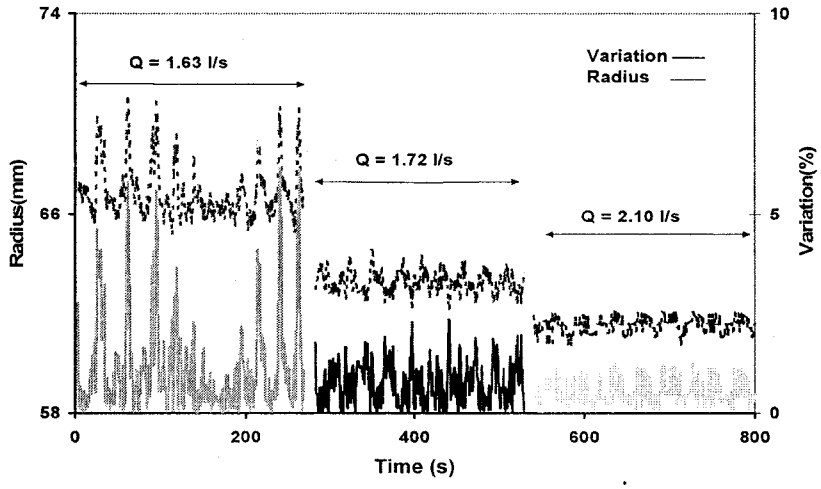

Fig.4 Radius and radius variation response at different air flow rate (BUR=2)

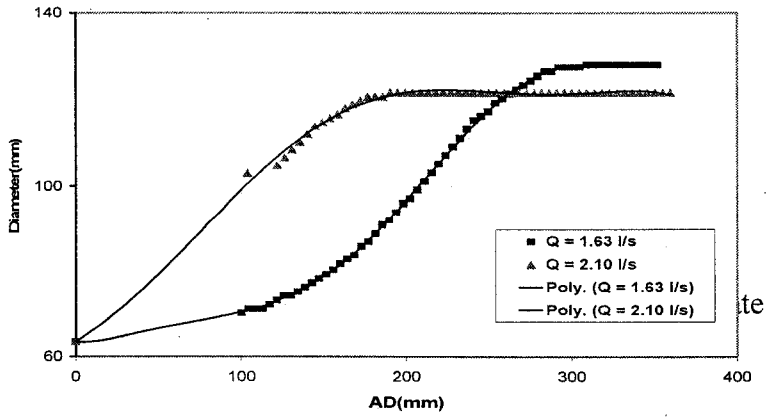

Fig.5 Bubble shapes at different air flow rate

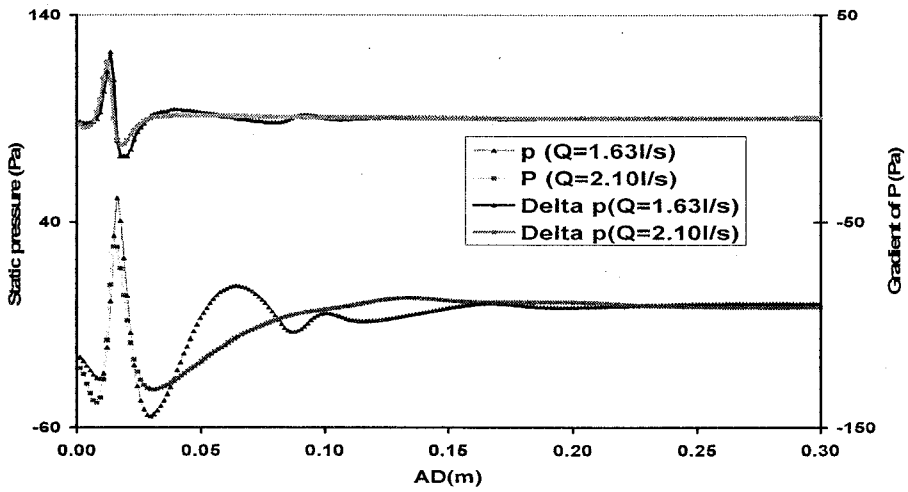

Fig.6 Gradient of pressure and pressure profile around bubble surface for different air flow rate (BUR=2)

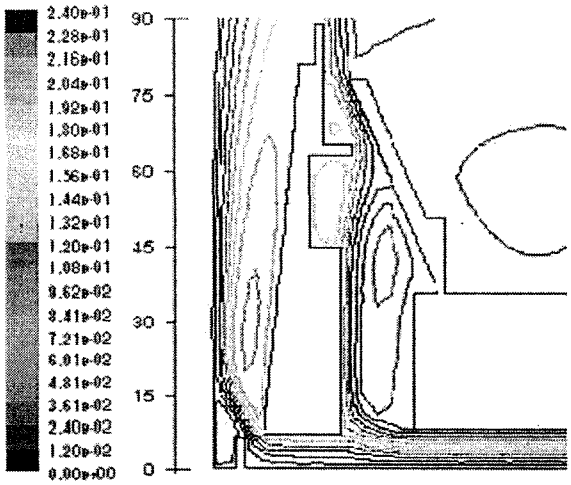

Fig.7 cooling air streamline around the bubble inside air ring

Key words

Air cooling, aerodynamics, bubble instability, negative pressure

APPENDIX C: Effect of aerodynamics on film blowing process

Published in International Polymer Processing, 2006, XXI, 5, p527

Z. Zhang, P.G. Lafleur and F. Bertrand*

Department of Chemical Engineering, Ecole Polytechnique de Montréal, CREPEC, Montreal, QC. H3C 3A7 Canada

Abstract

A Computational Fluid Dynamics (CFD) technique using a renormalization group (RNG) k-ε model and Fluent software was employed to analyze numerically the effects of aerodynamics on the air ring cooling system of a film blowing process. An in-line scanning camera system developed in our lab was used to study experimentally the detailed dynamics of bubble instabilities. An operation window for the heat transfer coefficient and the maximum air velocity function was established. The simulation results showed that it is adequate mainly at low BUR (Blow-Up-Ratio) outside of the air ring. The relationship between thermal inertia and cooling air aerodynamics for different bubble geometries was also explored. Different bubble shapes, for the same BUR, produced significant differences in the airflow pattern and heat transfer coefficient. The combination of experimental measurements and numerical simulations indicated that various cooling rates result in important variations in the dynamics of bubble instabilities for different BUR bubbles. It was observed that increasing the cooling rate can destabilize the lower BUR bubbles, but stabilize the higher ones due to the production of different bubble shapes. Finally, it is shown that the bubble instabilities depend on the static pressure distribution along the bubble surface, and that minimizing the pressure gradient can stabilize the bubbles.

Key words: film blowing, bubble instability, heat transfer coefficient, aerodynamics, CFD

---

*Corresponding author: tel: (514)340-4711ext. 4461; fax: (514)340-4031;
email:pierre.lafleur@polymtl.ca

INTRODUCTION

Tubular film extrusion is one of the most important polymer processing operations. It has been extensively used for the production of uni-axially and bi-axially oriented thin polymeric films. The air cooling system is an integral part of any tubular film extrusion line. Air jets cool the bubble by reducing the temperature of the polymer from the die exit to the frost line height. At the same time, these jets also exert an aerodynamic force on the bubble surface that can either stabilize or destabilize the bubble. Since the cooling power directly limits the polymer mass throughput, increasing the airflow rate seems to be a good way of increasing the final production rate. However, accelerating the flow of cooling air can lead to bubble instability and bad film properties. Therefore, the design of an efficient air-cooling system should take into account the effect of aerodynamics on the heat transfer in the overall film blowing process.

Numerous investigations have proposed analytical models to study heat transfer produced by cooling jets [1-5]. Most of them are relatively simple and have been used to predict heat transfer and the pressure distribution around the bubbles. Cao and Campbell [6] later studied the relationship between cooling rate, inflating pressure distribution inside the bubble and bubble shape. Cao [7] developed a full aerodynamic analysis model based on the method of superposition of stream functions as well as on mass and energy balance to show that there are significant pressure variations along the bubble surface. Campbell et al. [8] considered the effect of cooling-air velocity on blown-film formation and dealt with the aerodynamic aspect of the process by assuming axi-symmetric laminar jet flow and using the model developed by Cao [7]. Experimental observations revealed that the model produces correct streamlines that coincides with the model contour and leads to fairly good predictions for the pressure and velocity distributions. Because the typical Reynolds number based on the air ring clearance and air velocity exceeds 10^4, the flow of cooling air around the bubble is turbulent and very complex. Wolf et al. [9] extended the work of Campbell [8] by using a standard k-ε turbulent model and FIDAP to predict airflow for jets impinging on the blown film

bubble. They found out that the size of the vortices produced by the cooling jet has a significant effect on heat transfer. Nagarajan and Campbell [10] observed from experimental results that heat transfer coefficient changes locally. Hauck and Michaeli [11] proposed a 1/7 power turbulent analytical model for the calculation of the heat transfer coefficients based on the experimental investigation of air cooling. Sidiropoulos et al. [12, 13] compared the cooling profiles of single and dual orifice air rings using the renormalization group (RNG) k-ε turbulent model and Fluent. They found out that cooling mainly takes place inside a single air ring whereas heat transfer rate depends on the ratio of lower and higher lip sizes for a dual lip air ring. Akaike et al. [14] investigated numerically heat transfer from the molten polymer surface to cooling air using the Abe-Kondo-Nagano model, and attempted to estimate how the cooling air affects the bubble formation. Later, Gregory et al. [15] developed a relatively simple model and showed predicted that the heat transfer coefficient goes through a maximum as the bubble expands.

The aforementioned investigations all focused on the effect of airflow on heat transfer in film blown process. It is well known that, since the aerodynamics forces represent one of the key factors for bubble stability, they play a predominant role on determining the production rate and the quality of the film produced in this process. However, research in this area remains limited, due to the complexity of the cooling airflow and the absence of a device that can capture quantitatively the characteristics of bubble instabilities. Huang [16] used a pressure transducer to detect variations of pressure inside the bubble and correlated them to oscillations in the bubble diameter. Ghaneh-Fard [17] demonstrated that cooling rate variations may lead to bubble instability. Sidiropoulos and Vlachopoulos [18, 19] investigated numerically the bubble stability for dual-lip air ring and found out that jet acceleration from the lower lip of the air ring causes a negative gauge pressure between the bubble and the forming cone that may stabilize the bubble. In particular, they showed the importance of the Venturi and Coanda effects around the bubble. Gao et al. [20] measured the pressure distribution along the surface

of a rigid model bubble and found out that there exists a negative static pressure region, the extent of which is related to the processing conditions. To our knowledge, no literature has investigated quantitatively the relationship between bubble instability and the pressure at the bubble surface under different processing conditions. One objective of this work is to study the relationship between heat transfer and cooling air aerodynamics. Another one is to investigate the relationship between bubble instability and the aerodynamics of cooling jets.

METHODOLOGY

Experimental

An experimental setup for the film blowing process has been developed in our lab, which consists of a 45mm Killion single screw extruder with a helical film die (D_0 = 63.5mm, h_0 = 1.5mm with double lips), as shown schematically in Fig.1. In this work, a dual orifice air ring was used; its cross section is also schematized in Fig.1. Air is pumped by a blower. Airflow rate is controlled with a bleed valve that discharges air to atmosphere and with a backpressure valve that directs air to the air ring. The volumetric airflow rate through the air ring was measured by multiplying the air velocity by the wetted area. The air velocity was obtained with a FMA-905-V air velocity transducer; it was calibrated in a NIST-traceable wind tunnel by the OMEGA Co. A temperature compensation is provided internal the transducer, no temperature and pressure corrections are required in the application range of -40 to121°C, 150 PSIG maximum. The temperature at the bubble surface was measured as a function of vertical distance from the die by an infrared pyrometer (IRCON 3400). The melt index, density and heat capacity of the LDPE used in this study were determined by the resin supplier by means of the ASTM-D1238, D792 and C177 methods, respectively. Their values are 0.88g/10min, 923.9kg/m^3 and 2300kJ/kg*K, respectively. The DSC melting point of 385K was supplied by DOW Chemical Co.

The bubble diameter profile was determined by video camera. Bubble instabilities were experimentally studied using an in-line scanning camera system developed in our laboratory [21]. Polymer melt temperature was set to 180°C at the die exit, and the flow rate of polymer was maintained at 2.5 ±0.1 kg/hr. The Take-Up Ratio (TUR) was maintained at 38. The cooling rate was increased or decreased gradually in order to generate unstable bubbles. Detailed dynamics of bubble instabilities was investigated as a function of time at various cooling air flow rates.

Simulation

Turbulence modeling

The turbulent flow of cooling air around the bubble is governed by the Navier-Stokes equations. In this work, the RNG k-ε model [22] of Fluent was used, which is an improved version of the standard k-ε model that has been shown to be better suited to the treatment of flow in the regions where the Reynolds number is small (e.g. near the walls). Another advantage of this model is that it calculates the effective inverse turbulent Prandtl number as a function of μ_{mol}/μ_{eff}, which is consistent with experimental evidence and allows heat transfer to be accounted adequately in low Reynolds number regions.

Using the effective viscosity (μ_{eff}) defined in the RNG k-ε model, the mean momentum equation for two-dimensional flow can be written as:

$$\frac{\partial(\rho U_i)}{\partial t}+\frac{\partial(\rho U_i U_j)}{\partial x_j}=\frac{\partial}{\partial x_j}\left[\mu_{eff}\left(\frac{\partial U_i}{\partial x_j}+\frac{\partial U_j}{\partial x_i}\right)\right]-\frac{\partial p}{\partial x_i} \tag{1}$$

The turbulent transport of energy equation is given by:

$$C_p\left(\frac{\partial(\rho T)}{\partial t}+\frac{\partial(\rho U_i T)}{\partial x_i}\right)=\frac{\partial}{\partial x_i}\left[\alpha_h \mu_{eff} C_p \frac{\partial T}{\partial x_i}+U_j \mu_{eff}\left(\frac{\partial U_i}{\partial x_j}+\frac{\partial U_j}{\partial x_i}\right)\right] \tag{2}$$

The reader is referred to FLUENT use's guide [23] for more details on these equations and the RNG k-ε model.

However, the turbulent models based on the k-ε elements do not take account any wall effect and is inadequate for the investigation of the momentum and heat transfer near the wall. The enhanced near wall treatment was employed at the solid surface in this study; it can automatically accommodate cells places in the log-law layer and hence provided a more robust treatment.

Computational grids

Owing to the symmetry of the bubble with air ring geometry, a 2D axi-symmetry coordinate system was considered. A mesh sensitivity analysis was performed using three different grid sizes (coarse, intermediate and fine grids) generated with the help of GAMBIT from Fluent. The grids were refined near the bubble surface, especially inside the air ring to ensure adequate resolution. The number of grid cells for the whole computational domain was 9173, 29174 and 50716 for the three meshes considered. As an illustration, one example of computational grid along with the boundary conditions is given in Fig. 2. In order to get a clear view, 2861 cells are shown, which covers one fourth of the number of nodes along the axial direction of the bubble as compared to the coarse grid. Pressure and heat transfer coefficients were computed for the three meshes to assess the influence of grid size on the solution. As it can be seen in Fig.3, there is a variation of about 1% between results obtained from the intermediate and the fine mesh, while the coarse mesh produces results that are significantly different from those obtained with the intermediate one. The intermediate mesh was also considered to ensure that the meshes the near walls were fine enough to take into account the viscous sublayer ($y^+ \approx 1$). Thus, the intermediate mesh was accepted to use for all subsequent simulations.

Boundary conditions

The air is assumed to be an ideal gas. The ambient temperature is set to 298K. The bubble shape is fixed and corresponds to that measured experimentally. The frost line height was set to 120-300mm in this work. Cooling air enters the domain with predetermined velocity ($\overline{V}$), ambient temperature (T), kinetic energy of turbulence (k) and dissipation rate (ε). Kinetic energy and dissipation rate are estimated from the following relationships [23]:

$$k = \frac{3}{2}(\overline{V}I)^2 \tag{3}$$

$$\varepsilon = C_{\mu}^{3/4} \frac{k^{3/2}}{0.07D} \tag{4}$$

The turbulence intensity, I, is defined as the ratio of the root-mean square of the fluctuation velocity ($V - \overline{V}$) to the mean flow velocity:

$$I = \frac{\left[\overline{\left(V - \overline{V}\right)^2}\right]^{1/2}}{\overline{V}} \times 100\% \tag{5}$$

A no-slip velocity is imposed along the bubble surface. During the simulations, the temperature profile along this surface was gradually decreased according to the experimental data. Else where, the temperature was set to 298K and an atmospheric pressure was imposed.

Solution method

All computational results presented in this paper were obtained from the commercial CFD code FLUENT 6.2.16. A second order upwind scheme was used for the solution of the momentum equation and the transport equations for the turbulence variables (kinetic energy and dissipation rate). Each simulation was run on a pentium4 PC and took between 40 and 60 minutes. Convergence criteria were set in Fluent to ensure that the results were fully converged. The heat transfer to the walls is calculated using the log-law formulation for the temperature derivative (based on the analogy between heat and

momentum transfer) [24]. The flow streamlines were calculated from the resulting velocity fields.

Validation

Fig.4 shows numerical and experimental results for the air velocity distribution around the bubble at two different heights from the die for a BUR of 2.28. The predictions are in good agreement especially near the air ring close to the bubble. The maximum experimented air velocity is 3.34m/s at the distance of 8.7mm from the bubble surface and the computed one is 3.40m/s at a distance of 9.2mm. When moving away from the surface, for both heights, the experimental and numerical velocity profiles follow the same trend; they decrease with respect to the radial distance. However, at that position turbulent intensity is very high and discrepancy of about the 50% can be found away from the bubble.

RESULTS AND DISCUSSION

Flow field results predicting heat transfer coefficient and velocity around the bubble surface are presented in this section for Reynolds number ranging from 7800 to 24000. Other results depict the relationship between the bubble instability and pressure distribution in the film blowing system.

Effect of aerodynamics on the heat transfer

Heat transfer between the bubble and the cooling air plays a predominant role on the temperature dependent rheological properties of the melt, its crystallization and degree of orientation upon cooling. The determination of the heat transfer coefficient between the cooling air and the bubble is then critical in this study. Several correlations have been proposed in the literature for the evaluation of the heat transfer coefficient, like the following [10]:

$$\text{Zippenfeld model: } h = 7.11(V_{\max})^{0.78} \qquad [6]$$

Menges and Predohl model: $h = 3.3(V_{max})^{1.5}$ [7]

Petrie model: $h = 4(V_{max})^{1.5}$ [8]

Kanai and White model: $h = 0.043K_{air}(\mathrm{Re})^{0.78} / L$ [9]

Where, K_{air} is a constant and L is function of V_{max} in the Kanai and White model. Re is the Reynolds number.

The numerical analysis was performed for heat transfer between bubble surface and cooling air as well as velocity of cooling air around the bubble at different BUR conditions. Fig.5 shows the profiles of heat transfer coefficient and the maximum velocity along axial distance on the internal and external air-ring. It was found out from the plots there is no simple correlation between the air velocity and heat transfer for both lower and higher BUR inside the air ring (below z = 90mm). Therefore, no simple correlation can be used inside the air-ring to improve die design by predicting flow and heat transfer. Outside the air-ring, the maximum velocity profile exhibits the same trend as the heat transfer coefficient; especially at lower BUR. Fig.6 shows the logarithm of heat transfer coefficient versus the maximum velocity. The relationship is almost linear on a plot. The regression coefficient R^2 decreases from 0.98 to 0.86 with a BUR increasing from 1 to 3, which indicates a better fit for the lower BUR bubble. Further, simple model $h = a\ (Vmax)^{b}$ predicts a better relationship between heat transfer coefficient and maximum velocity for lower BUR than for higher BUR bubble. This observation is at least qualitatively coincident with that one reported by Gamache et al. [25].

In order to examine the correlation between thermal inertia and aerodynamics of cooling air further, numerical simulation was performed on different shapes and same BUR bubbles. Heat transfer coefficient profiles along the bubble surface obtained from the numerical analysis are presented in Fig.7 for three bubbles (Bubble1: long neck,

Bubble3: short neck and Bubble2: intermediate). The heat transfer coefficients went up through a maximum at a location around z = 14mm and then decreased. Another smaller peak appeared on z = 90mm for Bubble2 and Bubble3, while the profile of heat transfer coefficient decreased gradually for Bubble1. Close to the air-ring, the heat transfer coefficient is the highest for bubble1 and the lowest for bubble3. Away from the air-ring the situation is reversed.

Flow pattern of cooling-air are shown in Fig.8 for the three different bubble shapes and can be used to explain variation of heat transfer coefficients. In order to get a clear view, partial zoom-in inside the air-ring at the first point of contact with the bubble is also shown in the Fig.8. The three shapes show vortices in the area between the bubble surface and the air-ring gate avoiding bubble instability led by the air stream from the lower lip jetting directly to the bubble surface. It is well known that the selection of air ring design always plays a critical role in determining cooling processing. However the recirculation flow region reduces the heat transfer rate and is responsible for the presence of the first heat transfer coefficient maximum at a position around 14 mm from the die exit.

Velocity vector, shown in Fig.9, could also be used to provide a representation of not only direction but also magnitude of flow. From the zoom-in sections we can see higher velocities near the lower-lip jet region for Bubble1 where the heat transfer was calculated to be the highest.

The second peak of heat transfer coefficient appearing in the heat transfer coefficient profile for Bubble2 and Bubble3 is due to the well-known Venturi effect. The Venturi is caused by the air accelerating from the main part of the air-ring (z = 90mm) at the gap formed by the bubble surface and the air-ring. The gap adjustment due to the bubble shape will affect the air velocity. Narrow gap (like the situation of Bubble3) tends to

increase the Venturi effect by increasing the speed of air flow. This is the reason why the second peak in heat transfer coefficient was the highest for Bubble3.

Additionally, it was found out from Fig.9 that the upper lip of the air-ring injects large volumes of air, the vertical and stream-wise velocity components are simultaneously enhanced by the conjoined flow parallel to the bubble surface, resulting in high Reynolds stresses and produce the high heat transfer rate.

Effect of aerodynamics on the bubble instability

Flow rate of cooling air plays a predominant role in the bubble instability. Draw resonance bubble instabilities caused by flow rate were investigated in this study. When the diameter of the bubble is similar or bigger to the one of the air ring exit, this kind of instability will take place.

Fig.10. shows radius and radius variation response for a Blow-Up-Ratio (BUR) of 1 at different air flow rate. When flow rate varies from lower to 3.61 l/s, a typical stable bubble was observed with a radius variation less than 1%. Increasing the flow rate to 4.03 l/s, variation of radius produces up to around 4 % with periodic oscillations, and exceeded the critical value of 2.5%. With another increase of 0.19 l/s, the variation of radius dramatically changes to show oscillations greater 20%. However, all the bubbles have a similar average diameter. The situation is reversed for a bubble with the BUR of 2 as shown in Fig.11. These data were obtained at the same TUR (Take-Up-Ratio) as the previous one (BUR of 1). When the flow rate was set to 1.63 l/s, the radius variation exceeded the critical value of 2.5% with periodic oscillations. The bubble show typical draw resonance instability with a long-neck shape. An increase of air flow rate can change the bubble shape from long-neck to short-neck as shown in the Fig.12, at the same time, the radius variation decreases to around 2.5 %. The air flow rate was then increased to 2.10 l/s, stabilizing the bubble. The radii almost overlap each other with a radius variation down to 1%. A further increase of air flow rate will result in a bubble sitting down on the air ring and collapsing.

Static pressure and gradient of pressure distributions along the bubble surface obtained from the numerical analysis are presented in Fig.13 and 14. For the BUR of 1, the unstable bubble shows more pressure variation than the stable one. It is reasonable that the higher flow rate of cooling air can produce the higher pressure gradient around the bubble surface, and then destabilizes the bubble. For the BUR of 2, the complexity of the aerodynamics acting on the bubble surface produces a different effect as the one presented for a BUR of 1. Higher flow rate generated a lower static pressure gradient on the bubble surface, resulting in a stable bubble. The first peak on the pressure profile is higher for the smaller flow rate than the bigger one. Another peak appeared at z = 70 mm for the unstable bubble, while the profile of pressure increases gradually for the stable bubble. This is the reason why the unstable bubble has a long neck. The aerodynamics of cooling air determines the shape of the bubble. Varying the flow rate causes a variation of static pressure on the bubble surface, and then changes the bubble shape. As a result, the static pressure was re-distributed with the changing bubble shape. The peak, around 35Pa, on the pressure distribution is not negligible compared to typical value of the bubble inflation pressure of 250 Pa. Pressure changes can not be neglected. The acceleration due to the narrow gap between the air ring and the film produces another big vortex as shown in the Fig.15, which results in another negative pressure in the pressure profile. It seems that negative static pressure led by the vortex can act to stabilize draw resonance instabilities. However, the negative pressure region from z = 50mm to z = 90mm seems to be responsible for the bubble sitting down on the air ring.

Part of the air stream emerging through the lower orifice is forced to travel close to the bubble surface through a flow deflector. It deflects the flow away from the bottom of the polymer bubble where the polymer is at its melt temperature. The vortex created between the flow deflector and the base of the film presented in Fig.15 corresponds to the initial negative pressure in the static pressure profile as shown in the Fig.14. This local negative static pressure led by the vortex helps to stabilize the bubble by avoiding high speed airflow to act on the initial stage of the bubble. However, such a recirculation

flow region between the bubble surface and the air ring gate reduces the heat transfer rate as shown in the Fig.7; The combine affect of heat transfer and flow aerodynamics around the bubble surface on bubble instability is very complex and will be assessed in the future work.

CONCLUSIONS

The simulations showed that a relationship between the heat transfer coefficient and the maximum velocity, like the one proposed in the literature ($h = aV_{max}^{b}$), is good outside the air ring at low BUR, while no simple correlation can be used inside the air-ring to improve die design by predicting flow and heat transfer. Different bubble shapes at the same BUR produced significant differences in the air-flow pattern and heat transfer coefficient. Recirculation flow region inside the air ring could reduce the heat transfer rate. The heat transfer coefficient was higher for long neck bubble inside the air-ring and lower outside the air-ring because of the Venturi effect.

The bubble instability depends on many parameters in the film blowing process with aerodynamic forces being one of them. Increasing cooling air flow rate can act to destabilize draw resonance bubble for a BUR of 1, while minimizes the pressure gradient around the bubble surface resulting in a stabilizing effect for a BUR of 2. Different bubble shapes, produced by various cooling rates, showed important differences in dynamics of bubble instability for a constant BUR bubble.

Nomenclature:

$$y^{+} = \frac{y}{\mu_{mol}}\sqrt{\rho\tau_{w}}$$

y the distance from the wall to the cell center

τ_{ω} the wall shear stress.

μ_{mol} molecular viscosity,

ρ density of air

μ_{eff} effective viscosity

C_p heat capacity

U, $\overline{V}$ mean velocity

D hydraulic diameter

Q heat flow

Vmax Maximum velocity

h heat transfer coefficient

p static pressure

$C\mu$ turbulence model constant

α_h inverse turbulent Preandtl number

z Axial distance

References:

1. Yeow, Y. J.: Fluid Mech. 75, p.577 (1976)
2. Gupta, R.K., Wissbrun, A.M.K.: Polym. Eng.Sci. 22, p.172(1982)
3. Kanai, T., White, J.: Polym. Eng. Sci. 24, p.1185(1984)
4. Luo, X., Tanner, R.: Polym. Eng. Sci. 25, p.620(1985)
5. Cain, J., Deen, M.: Polym. Eng. Sci. 28, p.1527 (1988)
6. Cao, B., Campbell, G.: Int. Polym. Process. 4, p.114(1989)
7. Cao, B.: PhD thesis, Clarkson University, Potsdam, NY (1989)
8. Campbell, G., Obot , N., Cao, B.: Polym. Eng. Sci. 32, 11 p.751 (1992)
9. Wolf, D., Feron, B., Wortberg, J.: Inter. Polym Processing. XII p.38(1997)
10. Nagarajan , G., Campbell, G. A.: SPE ANTEC Tech. Papers, p.162 (1995)
11. Hauck, J., and Michaeli, W.: J of Reinf. Plast. Comp., v18, n10, p.895 (1999)

12. Sidiropoulos, V., Vlachopoulos, J.: SPE ANTEC Papers part 1(of 3), p.108(1998)

13. Sidiropoulos, V., Wood, P.E., Vlachopoulos, J.: J. Reinf. Plast. Comp., 18 p.529(1999)

14. Akaike, O., Tsuji, T., Nagano, Y.: Intern. Polym. Process., 14 p.168(1999)

15. Gregory, A., Campbell, N., Ganesh, S., Campbell, W., Lana B.,: SPE ANTEC Tech. Papers p.49 (2003)

16. Huang, T. A.: Advances in Polym. Tech. 8(1) p.65 (1988)

17. Ghaneh-Fard, A. : PhD thesis, Ecole Polytechnique de Montreal (1996)

18. Sidiropoulos, V., Vlachopoulos, J.: Intern. Polymer Processing XV, p.40 (2000)

19. Sidiropoulos, V., Vlachopoulos, J.: Polym. Eng. Sci. v40, n7, p.1611(2000)

20. Gao, N., Li, S., Ewing, D.: Intern. Polymer Processing XX, p.68(2005)

21. Kim, S., Fang, Y., Lafleur, P.G., Carreur P. J.: Polym. Eng. Sci. 44, p.283 (2004)

22. Yakhot, V., Orszag, S. A.: J. science. Comput. v1, p.3 (1986).

23. Fluent Inc., "Fluent User's Guide", Version 6.2 (1998)

24. Sidiropoulos, V., Vlachopoulos, J.: Intern. Polymer Processing XVI, p.48 (2001)

25. Gamache, E. : PhD thesis, Ecole Polytechnique de Montréal (2005)

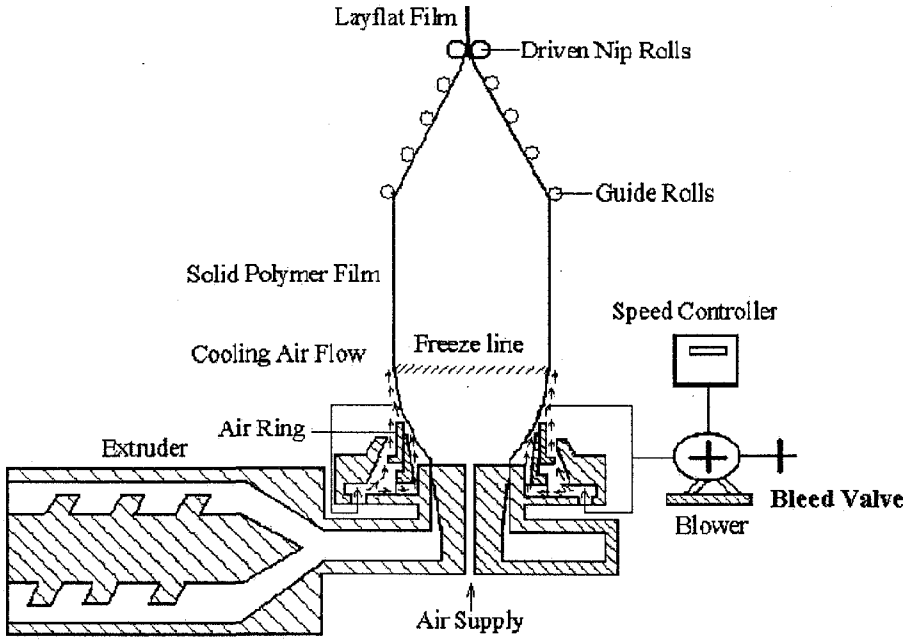

Fig.1 Schematic of film blowing process (not to scale)

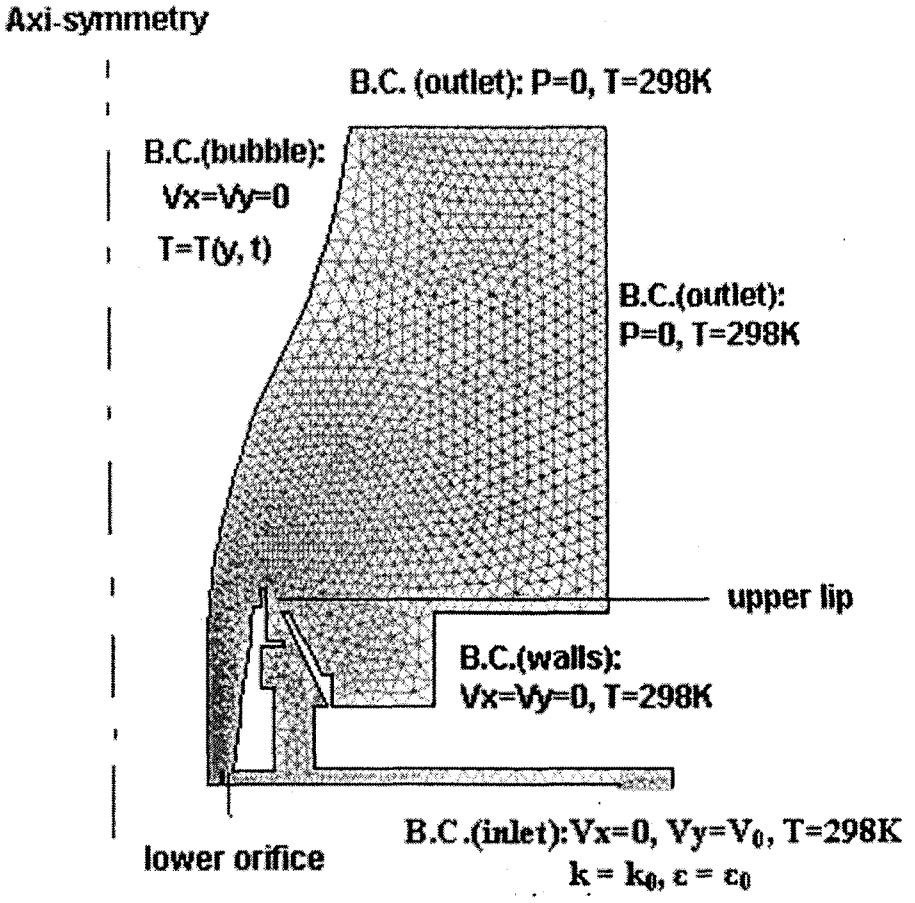

Fig.2 Computational domain with the boundary conditions

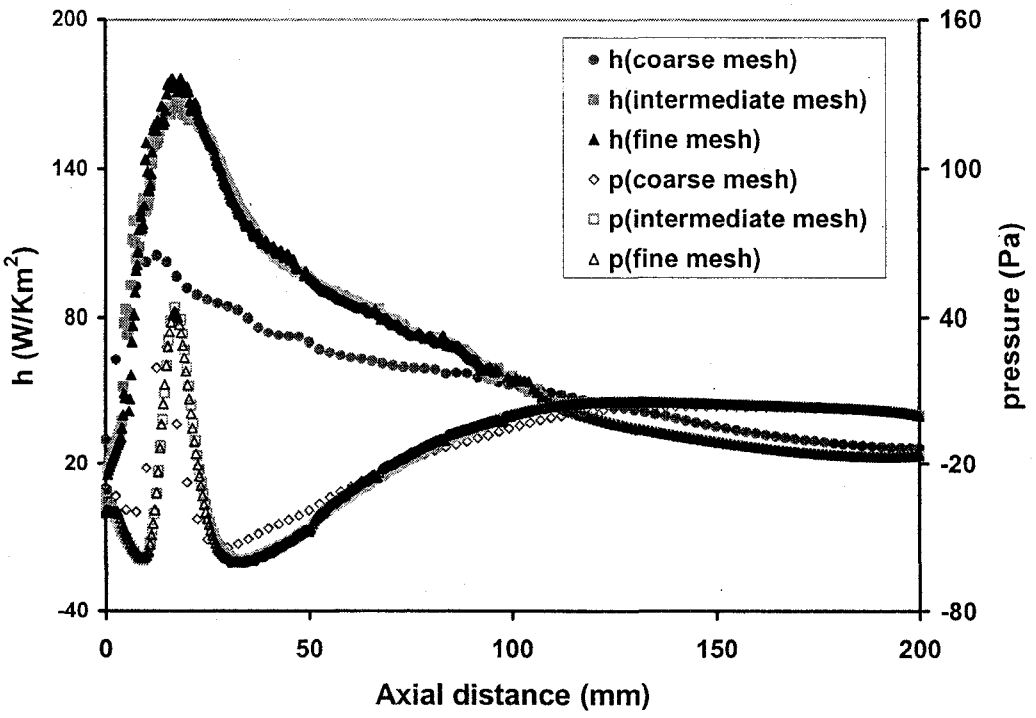

Fig. 3 Influence of grid size on pressure and heat transfer coefficient (TUR=38, BUR=2.5)

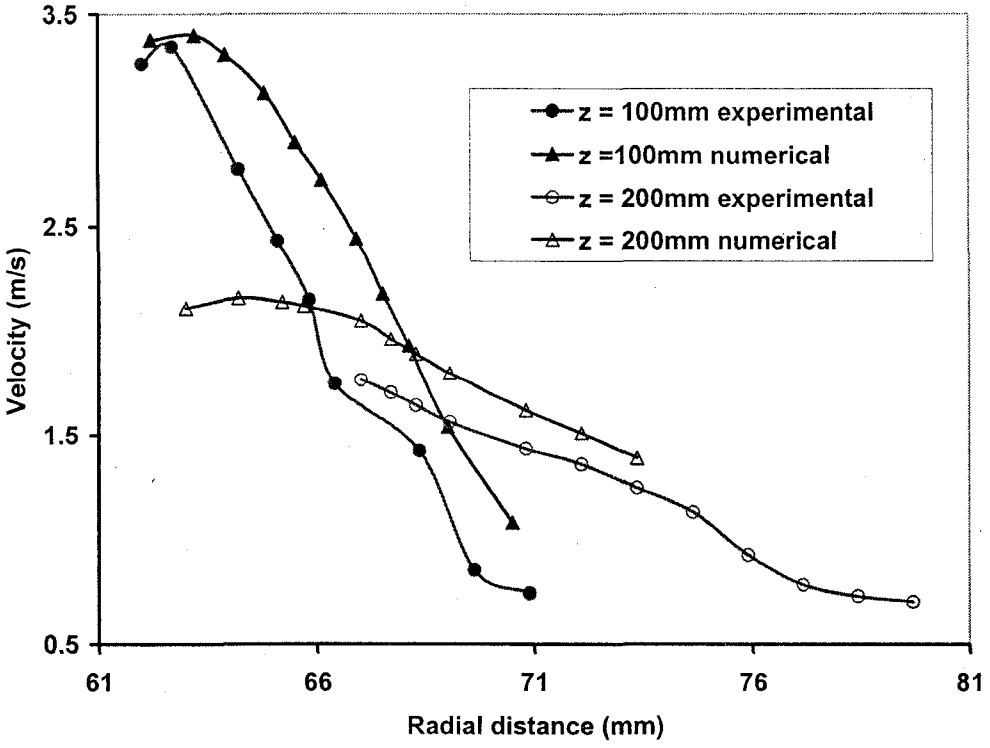

Fig.4 Comparison of numerical and experimental velocities (BUR=2.28)

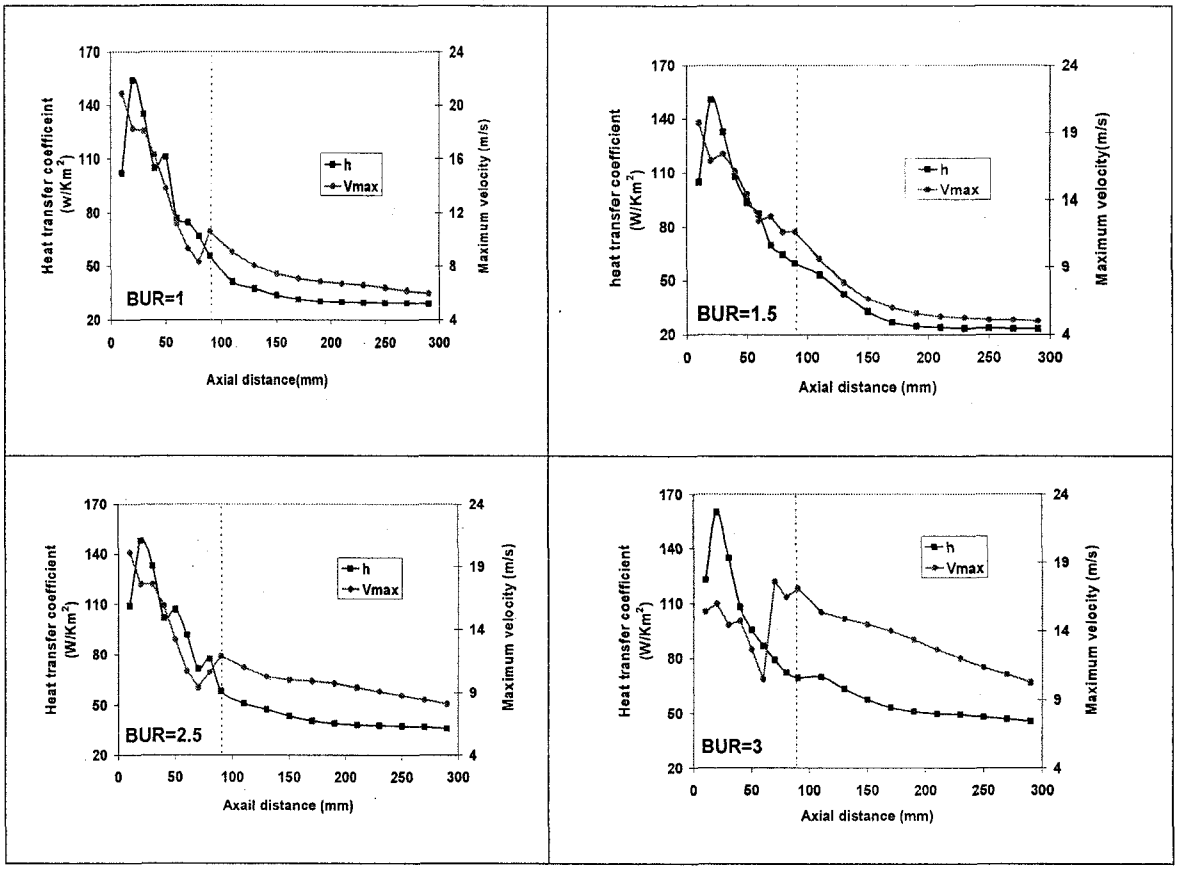

Fig.5 Heat transfer coefficient and maximum velocity profile at the different BUR

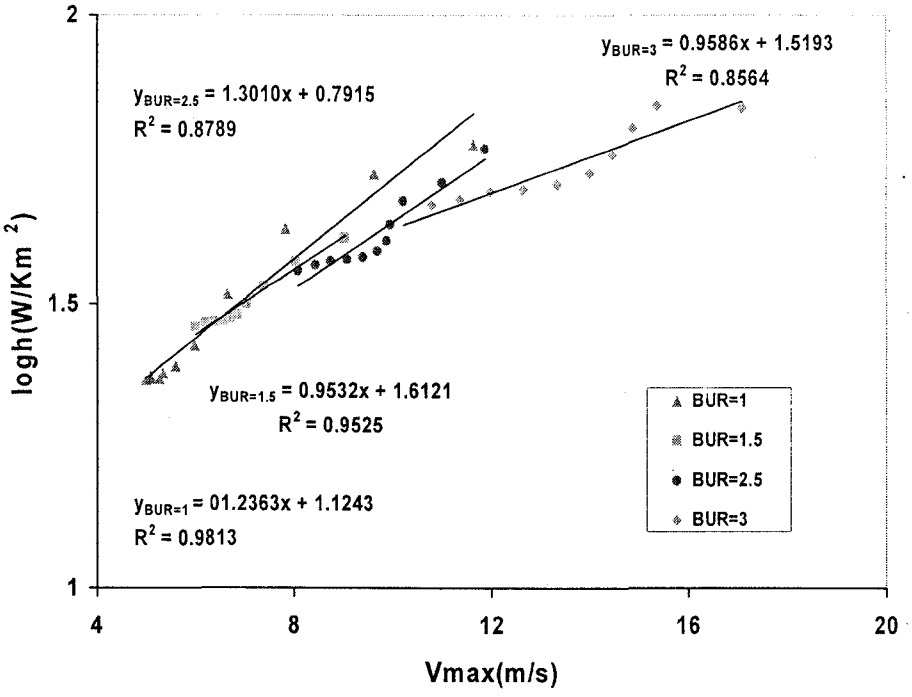

Fig. 6 Linear regression log (h) from Vmax on the external air-ring at different BUR

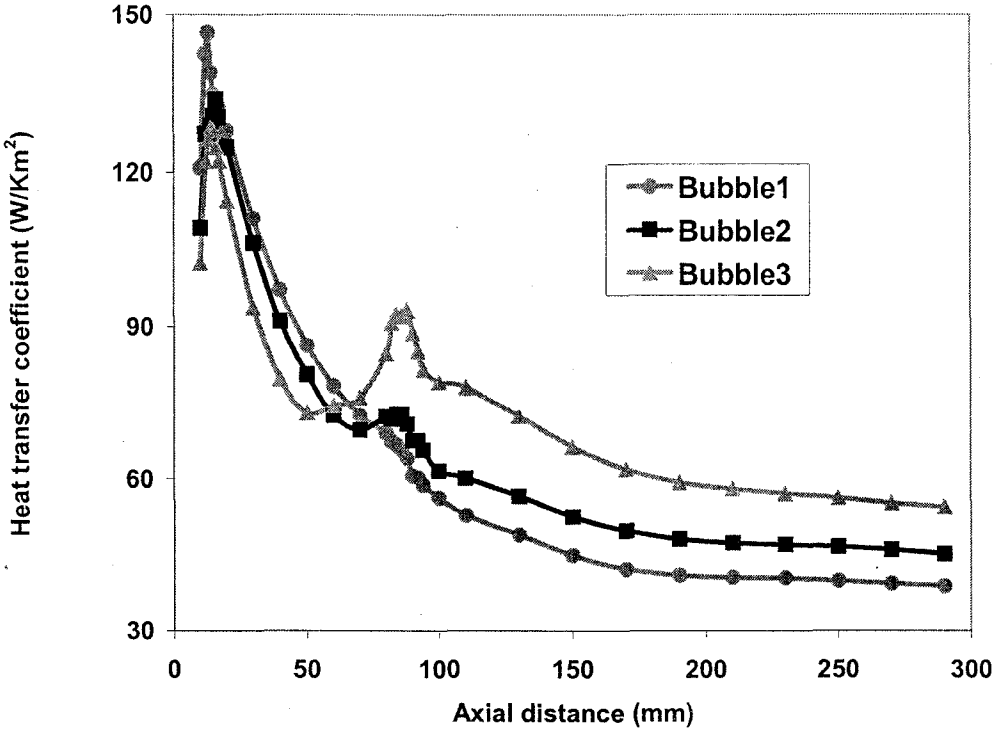

Fig.7 Heat transfer coefficient at different bubble shape (BUR=2.5)

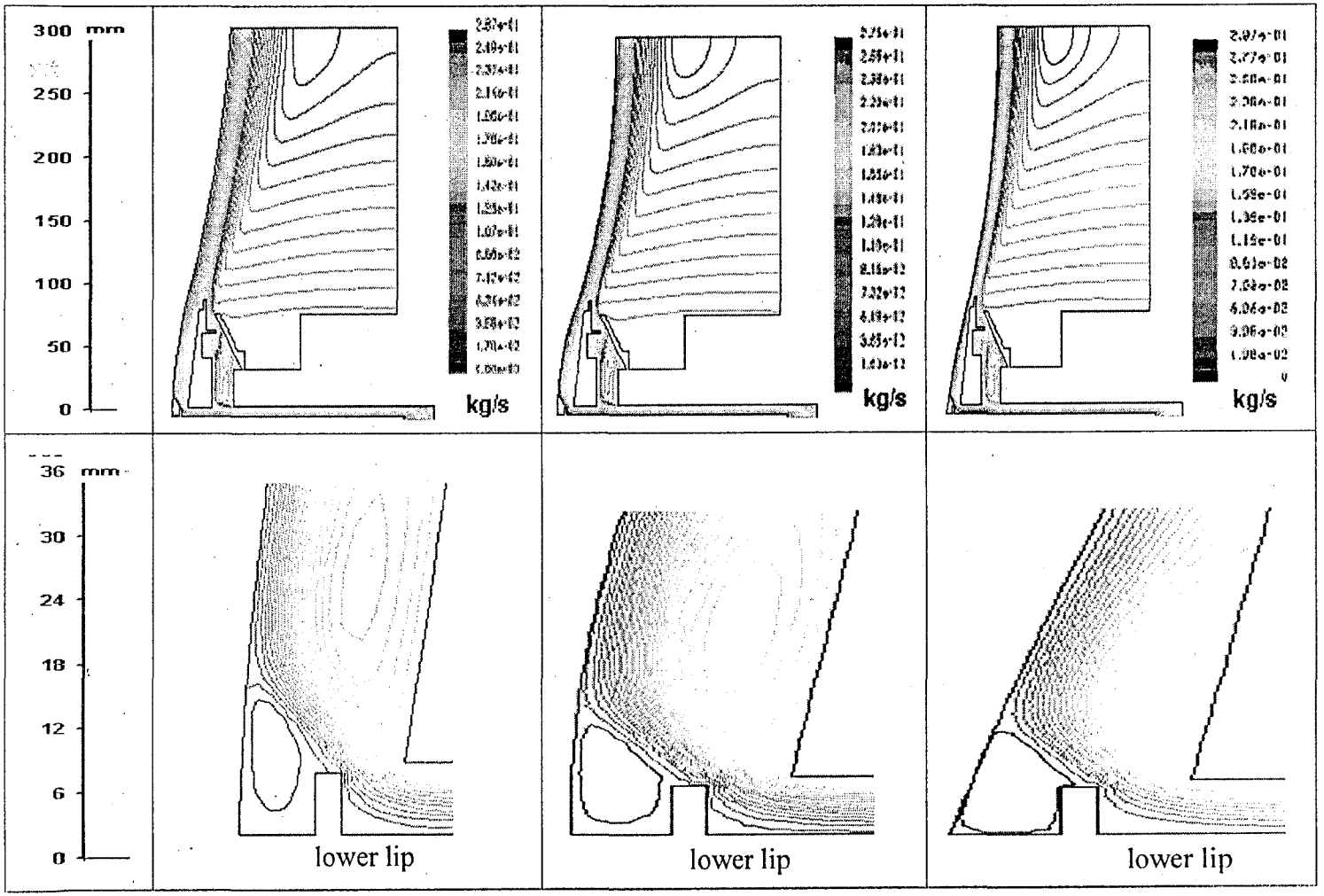

Fig.8 Cooling air streamline and partial zoom-in of flow around bubbles (BUR=2.5)

(Left: bubble1, middle: bubble2, right: bubble3)

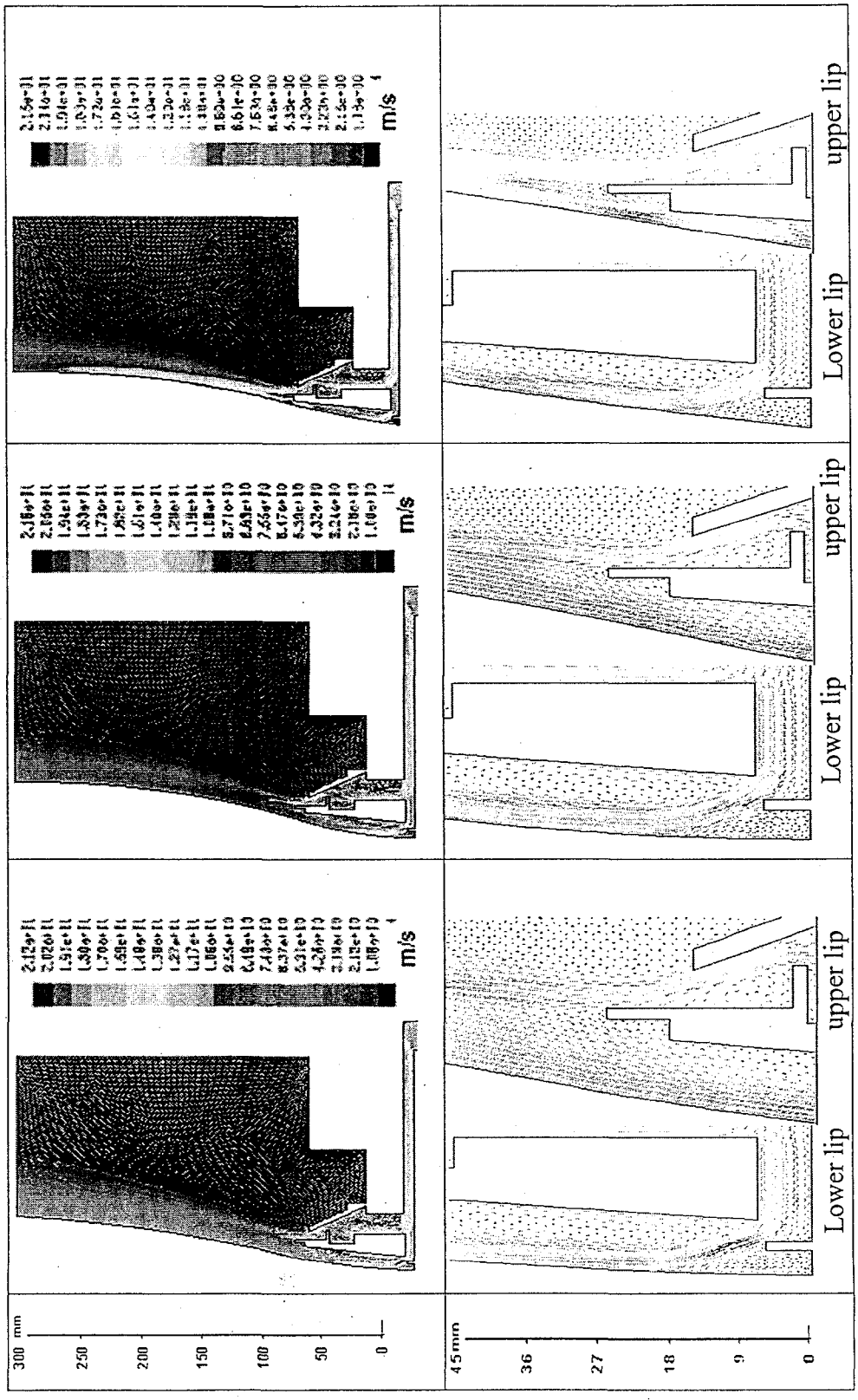

Fig.9 Velocity vector pattern and partial zoom-in of flow around bubbles (BUR=2.5)

(Left: bubble1, middle: bubble2, right:bubble3)

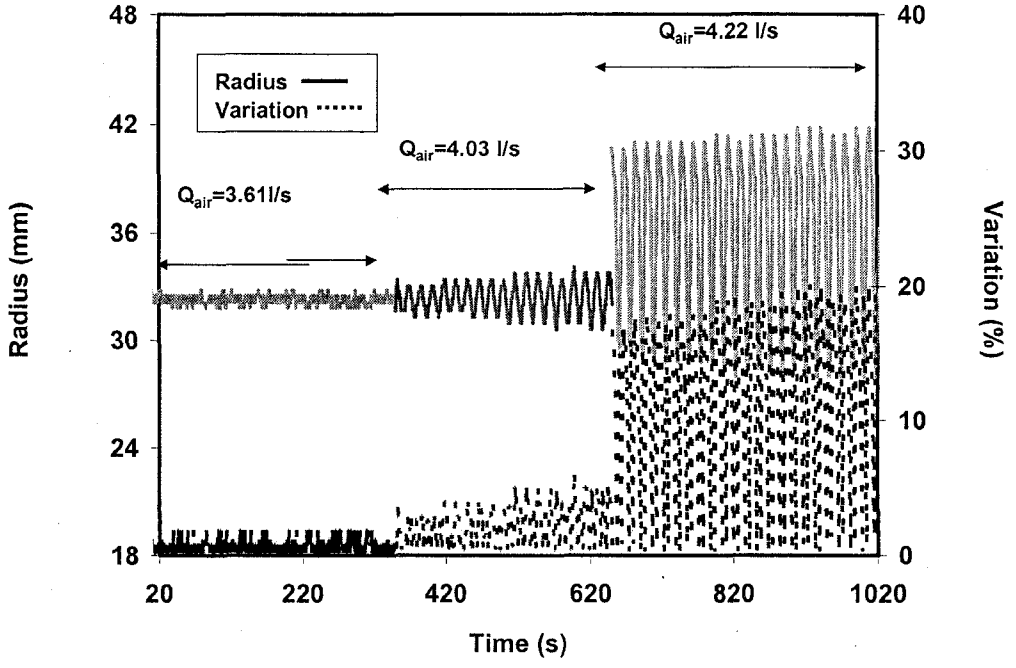

Fig.10 Radius and radius variation response at different air flow rate (BUR=1)

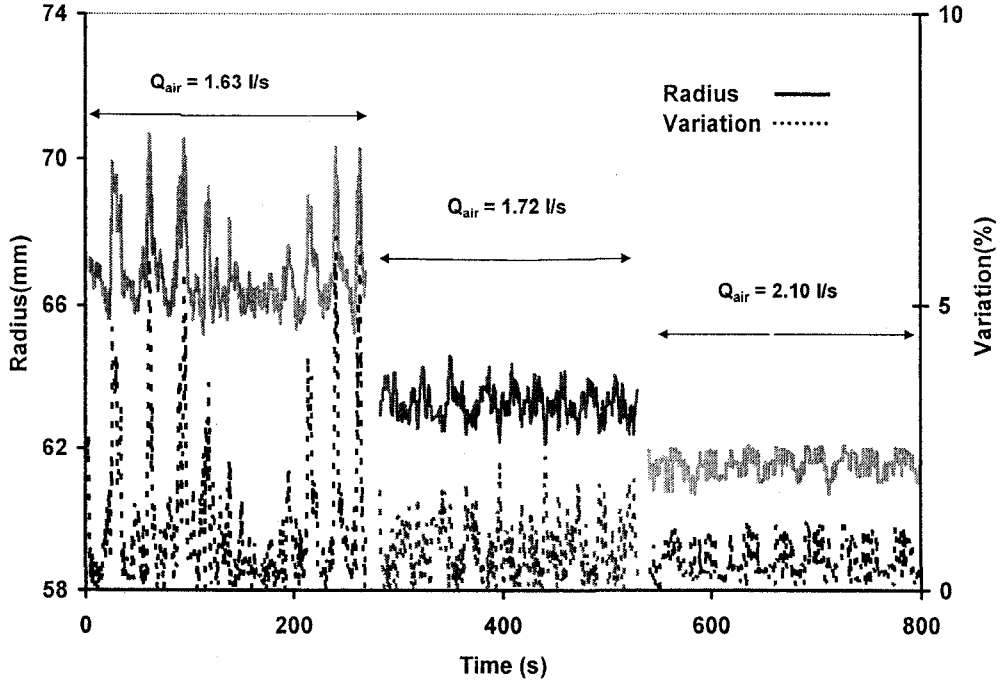

Fig.11 Radius and radius variation response at different air flow rate (BUR=2)

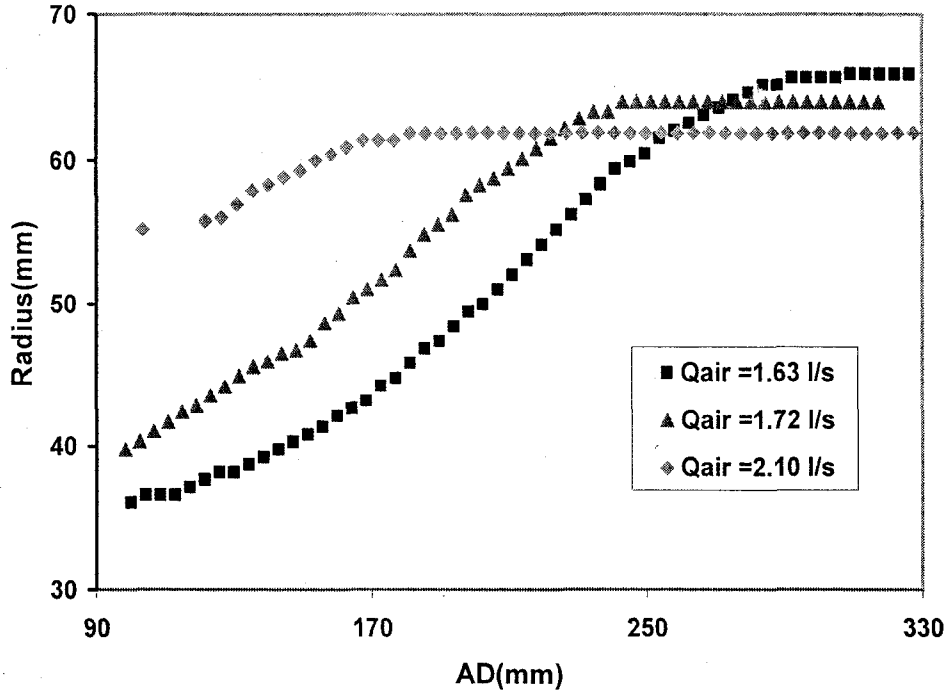

Fig.12 Bubble shapes at different air flow rate

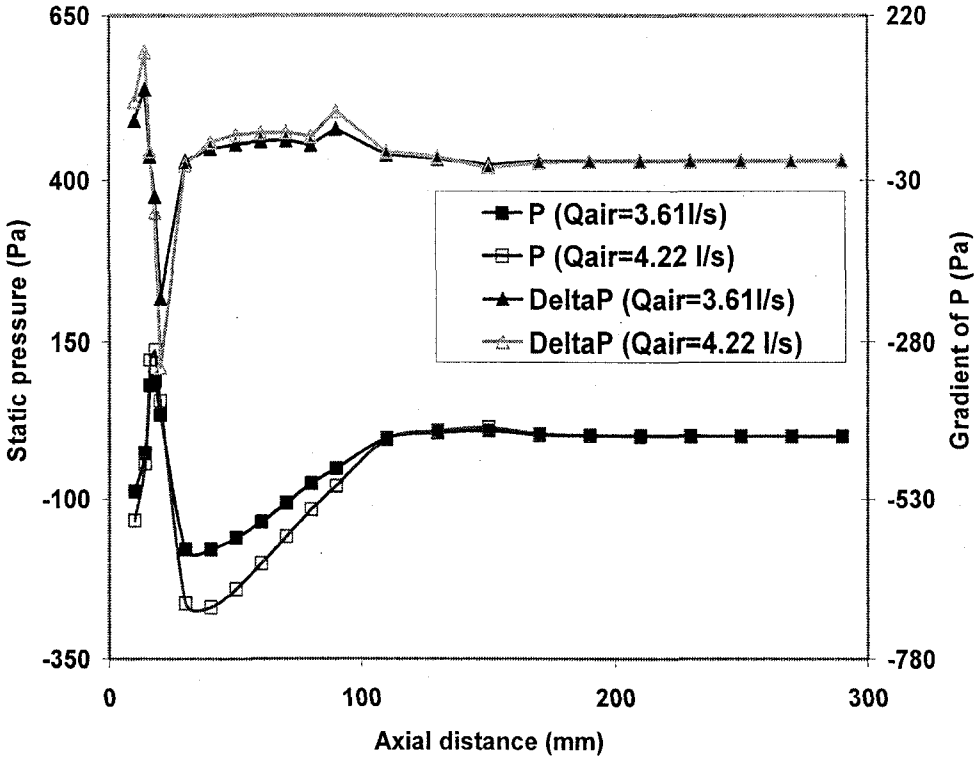

Fig.13 Gradient of pressure and pressure profile around bubble surface for different air flow rate (BUR=1)

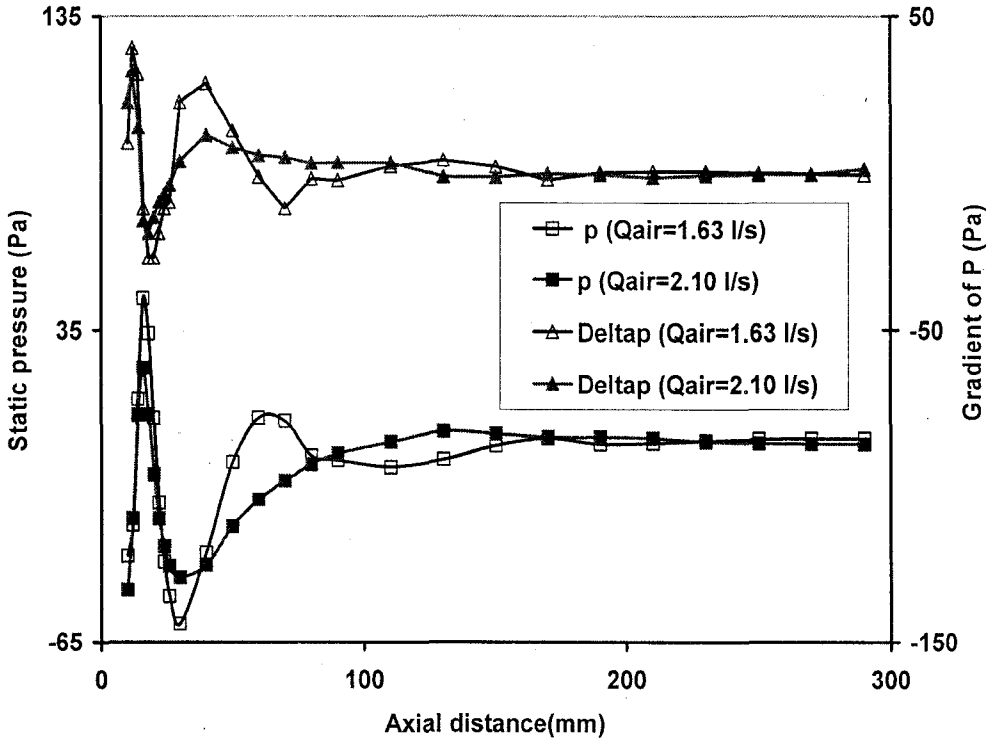

Fig.14 Gradient of pressure and pressure profile around bubble surface for different air flow rate (BUR=2)

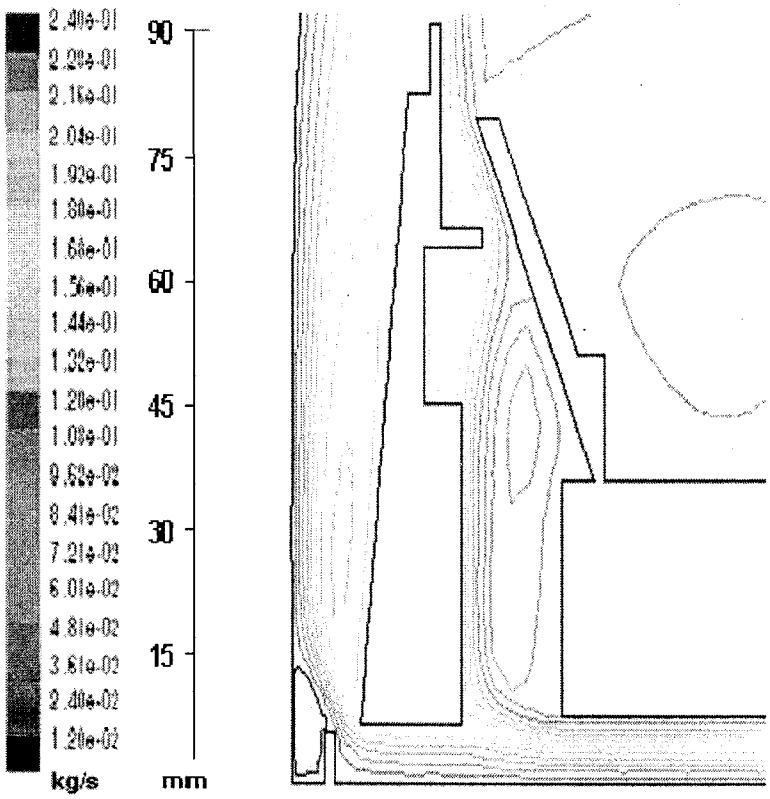

Fig.15 cooling air streamline around the bubble inside air ring

APPENDIX D: A Study of Heat Transfer in the Blown Film Process

Publication in Journal of Plastic Film and Sheeting (in press)

*Z. Zhang and P .G. Lafleur**

Department of Chemical Engineering, École Polytechnique de Montréal, CREPEC, CP 6079, Succ. Centre-ville, Montreal, QC. H3C 3A7 Canada

ABSTRACT

The air ring design directly affects the aerodynamic phenomena in the film blowing process. In this paper, the effects of impinging jets on heat transfer were explored taking into account the influence of cooling on the bubble shape, by comparing the characteristics and performance of flows produced by single and dual orifice air-rings. The aerodynamic characteristics of air-cooling flow around the bubble surface was investigated utilizing a finite volume numerical method and renormalization group (RNG) theory based on the k-ε turbulence model coupled with Enhanced Wall Treatment method of the FLUENT commercially available software. Our numerical analysis provided a detailed description of fluid flow pattern as well as heat transfer coefficients for different air ring designs, and under different processing conditions. The results of calculation indicate that the heat transfer rate critically depends on the air ring design. A simple correlation for the heat transfer coefficient and the maximum air velocity function (i.e., $h = aV_{max}^{b}$ proposed in the literature) was established. The boundary conditions dominated by airflow rates are equally important for cooling efficiency. The correlation between Reynolds number and the heat transfer in the numerical solution is also reported.

Key words: aerodynamics, dual orifice air ring, single-lip air ring, heat transfer coefficient, CFD

INTRODUCTION

The blown film process has been used to manufacture a broad range of commercial packaging and agricultural films since 1940. It is one of the most widely used polymer processing technologies. By 2000, approximately 25% of the 22M tones annual consumption of polyolefin in the United States and Canada was employed to produce blown films [1]. Such an increasing demand for high production rates with high quality films has steered the research community to pay more attention to developing materials and equipment for film blowing. However, the film blowing process is a very complex one, since many parameters influence production rates and properties of blown films. Heat transfer between the bubble and cooling air is an important and integral part of any blown film line. It greatly affects the temperature-dependent rheological properties of the melt, the crystallization and the degree of orientation in the cooling polymer. Due to the lack of detailed knowledge of aerodynamics of the cooling flow and its influence on heat transfer, the design of the air ring has to be done in a tedious empirical fashion. A less than optimal design limits the cooling power and might eventually lead to bubble deformation and an unacceptable final product. As a result, the effect of cooling airflow on heat transfer has received substantial attention in the literature.

One of the first studies to predict the bubble shapes considering heat transfer and using a non-isothermal model was done by Petrie [2]. Wagner [3] then studied the importance of the film temperature employing a non-linear, non-isothermal, viscoelastic model. There were several later investigations which examined heat transfer and the pressure distribution produced by cooling jets, using relatively simple models [4-8]. Kanai and White [9] experimentally investigated the effect of cooling rate on the rheological behavior, crystallinity (or crystallization rate), and heat transfer at the bubble surface. They found, as expected, that varying the airflow rate had a significant influence on the freeze-line height. Nagarajan and Campbell [10] experimentally observed that the heat transfer coefficient varies locally. In most of the previous studies, heat transfer has been examined semi-empirically.

Campbell et al. [11] were the first to address the problem using a full aerodynamic analysis, including heat and momentum transfer models. Their models are based on the method of superposition of stream functions as well as mass and energy balances. They showed that there are significant pressure variations along the bubble surface. Wolf et al. [12 and 13] extended Campbell's [11] work by using a standard k-ε turbulent model and FIDAP to predict airflow for jets impinging on the blown film bubble. They found that the size of the vortices produced by the cooling jet has a significant effect on heat transfer. Akaike et al. [14] numerically investigated heat transfer from the molten polymer surface to the cooling air using the Abe-Kondo-Nagano model, and attempted to estimate how the cooling air affects the bubble formation. For the above investigations [11-14], the cooling airflow was produced by different single-lip air rings. Hauck and Michaeli [15] proposed a 1/7 power turbulent analytical model for the calculation of heat transfer coefficients, based on an experimental investigation of air cooling using dual orifice air ring. They compared air velocity and film temperature profiles at different air ring gaps and emergence angles. Then, Sidiropoulos and Vlachopoulos [16-19] carried out numerical simulations of cooling air aerodynamics in the blown-film process, employing a RNG k-ε turbulent model and commercial software (Fluent). They published several articles where the flow fields produced by different dual-lip and single-lip air rings were examined and compared. They noted that cooling mainly takes place inside the air ring for single-lip ones, whereas heat transfer rate depends on the ratio of lower and higher lip sizes for dual-lip ones. They also observed that the Coanda effect has a large influence on the heat transfer rates due to the tendency of air from the jets to attach to the surface. More recently, Gao et. al. [20] experimentally measured the velocity field in the region above the forming cone and the distribution of pressure on the bubble surface produced by a dual lip air ring. They characterized the development of the cooling jets were the lower jet was initially decelerated and then entrained into the upper jet which was attached to the bubble surface.

Heretofore, there has not been a detailed investigation to correlate the aerodynamics with heat transfer under different processing conditions. The objective of the study presented in this paper is to investigate the aerodynamic characteristics of air-cooling flow around the bubble surface and its influence on heat transfer taking into account the influence of cooling on the bubble shape, by comparing the characteristics and performance of fluid flow produced by both single and dual-lip air rings.

METHODOLOGY

Experimental Investigation

Film blowing unit

A 45mm Killion single screw extruder with a helical film die (D_0 = 63.5 mm, h_0 = 1.5 mm with double lips) was used. The extrusion temperature profile was set as 150/170/180/180/180°C from the hopper to the die. The flow rate of the polymer was maintained at 2.5 ±0.1 kg/hr. The properties of the low density polyethylene (LDPE) used in this study are summarized in Table1. The melt index, density and heat capacity were determined by the resin supplier according to ASTM-D1238, D792, and C177, respectively. The DSC melting point was supplied by the Dow Chemical Co.

Air-ring settings

The single and dual orifice air rings used in this study are schematically shown in Figure1. For both air rings, the air stream from the lower lip jets onto the bubble surface through a flow deflector. It deflects the flow away from the bubble, which results in reducing the pressure at the base of the bubble and allowing higher flow rates to be used. The dual-lip air ring is set by lowering the adjustable part of the single-lip ring and splitting the airflow into a lower jet and an upper one.

Measurements

Air was pumped by a blower. A backpressure valve directed air into the air ring. The airflow rate was controlled with a bleed valve that discharged air into the atmosphere.

The volumetric airflow rate (Q_{air}) through the air ring was measured by multiplying the air velocity (U) and the wetted area (A). The air velocity was measured with an FMA-905-V air velocity transducer, calibrated in a NIST-traceable wind tunnel by the OMEGA Co. No temperature and pressure corrections were required in the application range of -40 to121°C, and a maximum of 150 PSIG. The temperature at the bubble surface was measured as a function of vertical distance from the die by an infrared pyrometer (IRCON 3400). The instrument absorbs the infrared radiation in the wavelength of 3.43μm. At a certain BUR and an airflow rate, the targeted bubble shape was obtained by adjusting the TUR value. [BUR is the Blow-Up-Ratio, defined as the final film to the die radii ratio, and TUR is the Take-Up-Ratio, defined as the ratio of the take up velocity of the nip rollers and the extrudate velocity at the die exit.] The detection of the bubble shape was realized by analyzing digital photos of the stable process.

Simulation Investigation

Turbulence modeling

The flow of cooling air around the bubble is governed by the Navier-Stokes equations. Since the airflow is turbulent, the instantaneous velocity (u_i) can be considered as the sum of a mean velocity (U_i) and fluctuation velocity (u_i'). The Reynolds averaged Navier-Stokes equation for momentum transfer can be written as:

$$\frac{\partial \rho U_i}{\partial t}+\frac{\partial\left(\rho U_i U_j\right)}{\partial x_i}=-\frac{\partial P}{\partial x_i}+\frac{\partial}{\partial x_j}\left(\mu\left(\frac{\partial U_i}{\partial x_j}+\frac{\partial U_j}{\partial x_i}\right)-\left(\frac{2}{3}\mu\frac{\partial U_k}{\partial x_k}\right)\right)+g_i\rho+\frac{\partial}{\partial x_j}\left(-\rho\overline{u_i'u_j'}\right) \qquad (1)$$

Where ρ is the density; μ is the viscosity, P is the pressure, and t is the time. In this work, the Renormalization Group (RNG) k-ε model of Yakhot and Orszag [21] was utilized to achieve turbulence closure. This model applies a scale elimination procedure to avoid computational problems associated with small-scale eddies, and introduces two

equations, one for the turbulence energy (k), and the other for its dissipation rate (ε). The contribution of Reynolds stresses ($-\rho\overline{u_i' u_j'}$) to the momentum balance is introduced through the concept of the effective viscosity (Boussinesq approximation) (μ_{eff}), which is expressed by the sum of the molecular viscosity (μ) and the turbulent viscosity (μ_{tur}) as following:

$$\mu_{eff} = \mu + \mu_{tur} = \mu\left[1+\sqrt{\frac{\rho C_\mu}{\mu\,\varepsilon}}\right]^2 \tag{2}$$

For high Re flows, $\mu_{tur} \succ\succ \mu$

$$\mu_{eff} = C_\mu \rho \frac{k^2}{\varepsilon} \tag{3}$$

Where, C_μ (a turbulence model constant) equals to 0.0845 [22]. The Boussinesq approximation makes possible the calculation of the Reynolds stresses as the product of the turbulent viscosity and the mean velocity derivatives. Therefore, the mean momentum equation for a two-dimensional flow can be written as:

$$\frac{\partial(\rho U_i)}{\partial t} + \frac{\partial(\rho U_i U_j)}{\partial x_j} = \frac{\partial}{\partial x_j}\left[\mu_{eff}\left(\frac{\partial U_i}{\partial x_j} + \frac{\partial U_j}{\partial x_i}\right)\right] - \frac{\partial p}{\partial x_i} \tag{4}$$

The turbulent transport of energy equation (Reynolds' analogy) is given by:

$$C_p\left(\frac{\partial(\rho T)}{\partial t} + \frac{\partial(\rho U_i T)}{\partial x_i}\right) = \frac{\partial}{\partial x_i}\left[\alpha_h \mu_{eff} C_p \frac{\partial T}{\partial x_i} + U_j \mu_{eff}\left(\frac{\partial U_i}{\partial x_j} + \frac{\partial U_j}{\partial x_i}\right)\right] \tag{5}$$

Where C_p is the heat capacity, T is the temperature, and α_h is an inverse turbulent Prandtl number. The scale elimination procedure provides an effective method of calculation for relatively coarse grids at high Reynolds number. However, the turbulent models based on the k-ε elements do not take into account any wall effects and are inadequate for the investigation of momentum and heat transfer near the wall. The enhanced near wall treatment was employed at the solid surface in this study. More details about RNG k-ε model and Enhanced Wall Treatment can be found in the FLUENT user's guide [23].

Simulation methodology

Owing to the symmetry of the bubble with air ring geometry, a 2D axi-symmetric coordinate system was employed. All computational results, presented in this paper, were obtained using the commercial CFD code FLUENT 6.2.16.

Topology refinements were examined using different grid sizes generated with the help of GAMBIT from Fluent, corresponding to various bubble shapes, blow-up ratios as well as air ring set-ups. An adequate resolution was employed to ensure that the meshes near the walls were fine enough to take into account the viscous sub-layer ($y^+ \approx 1$). The details of a mesh sensitivity analysis can be found in a previous publication [25].

A no-slip velocity condition was imposed along the bubble surface. As an illustration, one example (dual lip air ring) of computational grid along with the boundary conditions (B.C.) and initial conditions (I.C.) is given in Figure 2. In order to get a clear view, 2861 cells are shown, which covers approximately one tenth of the number of nodes along the axial direction of the bubble as compared to the real grids in the simulations. Experimentally, a gradually decreasing temperature profile along the bubble surface was used in the simulation. Since this boundary condition is not a constant, it was established by programming a Fluent UDF (User Defined Function). The bubble shape was fixed

and corresponded to that measured experimentally. The frost line height was set to 120-300 mm. The ambient temperature was set to 298K. Air was assumed to be an ideal gas; it entered the domain with predetermined mean velocity (U_i), ambient temperature (T), kinetic energy of turbulence (k) and dissipation rate (ε). The k and ε were calculated from the following expressions [23]:

$$k = \frac{3}{2}(U_i I)^2 \tag{6}$$

$$\varepsilon = C_\mu^{3/4} \frac{k^{3/2}}{0.07D} \tag{7}$$

Where, D is the hydraulic diameter at the inlet. The turbulence intensity, I, is defined as the ratio of the root-mean square of the fluctuation velocity to the mean flow velocity, it can be calculated from the experimental variables:

$$I = \frac{\overline{(u_i')^2}^{1/2}}{U_i} \times 100\% \tag{8}$$

The definitions reported in reference [24] were used to calculate dimensionless Nu and Re numbers. Thermal conductivity and viscosity were assumed to be constant and the density of the cooling air was considered to be a function of both pressure and temperature

A second order upwind scheme was applied for the solution of the momentum equation and the transport equations for the turbulence variables (kinetic energy and dissipation rate). Each simulation took approximately 40 to 60 min., depending on the grid, and was run on a 1.7GHz Pentium 4 PC running Unix. The proper criteria in Fluent were set to ensure full convergence of the results. For each of the finite volumes, solution of Equation (4) gives local values for pressure and velocity; solution of Equation (5) gives local values of temperature. The flow streamlines and heat transfer to the wall are calculated from the resulting velocity field and temperature derivative, respectively.

RESULTS AND DISCUSSION

Figure 3 displays experimentally obtained temperature profiles along the axial bubble surface at different airflow rates for both air rings. The temperature decreases as the axial distance (z) increases. For the single-lip air ring at the higher airflow rate of 2.81 l/s, however, the temperature profile reached a plateau immediately, indicating that all the heat transfer took place inside the air ring ($z < 100$ mm) in this case. At the lower rate of 1.78 l/s, the plateau was reached at $z \approx 230$ mm.

Numerical analysis was performed for heat transfer between the bubble surface and the cooling air using different operation conditions resulting in various bubble shapes and temperature profiles. Heat transfer coefficient (h) profiles along the bubble surface are presented in Figure 4. As expected, the heat transfer coefficients were higher for higher airflow rates for both air rings. However, for the same airflow rate, the heat transfer coefficient was higher for the single-lip air ring. Inside the air ring, the profile of heat transfer coefficient was almost the same for the single-lip at an airflow rate of 1.78 l/s and the dual-lip at a 2.81 l/s one. The heat transfer coefficient became higher for dual-lip away from the air-ring.

Airflow rates were adjusted to ensure that the temperature profiles of the bubble surface or the bubble shape were similar for different types of air rings. When similar temperature profiles were obtained, the airflow rate was 1.94 l/s for the dual-lip air ring, and 1.45 l/s for the single-lip air ring as presented in Figure 5. The bubble shapes obtained from these airflow rates were definitely different as seen in Figure 6. A short-neck shape was formed by the lower airflow rate using the single-lip air ring, while a long-neck shape bubble was formed by the dual-lip air ring. When the airflow rate was lowered to 1.21 l/s for the single-lip air ring and maintained at 1.94 l/s for the dual-lip air ring, same shape bubbles were obtained with two different temperature profiles around the bubble surface.

Heat transfer coefficient profiles corresponding to bubble surface boundary conditions obtained from the numerical analysis are displayed in Figure 7. For the same bubble shape, the heat transfer coefficients inside the air ring were almost equal although their temperature boundary conditions were different. Outside the air ring (z >100mm), these profiles start to separate. A greater difference in the heat transfer coefficient curve is observed close to the air ring due to the small peak appearing on z =100mm for dual-lip air ring, while for single-lip air ring, the heat transfer coefficient decreased gradually. For the same bubble temperature profile on the surface, the situation of the heat transfer was totally different. The overall heat transfer coefficient of the dual-lip ring was lower than that of the single-lip air ring, although a higher airflow rate was used for dual-lip air ring. From Figure 7, a comparison of the heat transfer coefficient profiles in the single-lip and the dual-lip air rings can be made. The single-lip profile goes through a peak higher than that for the dual-lip, then it decreases to the level of dual-lip at z = 50 mm. It goes through an even higher peak at z =100-160 mm, relative to the dual-lip profile, followed by a gradual decrease. A second peak is also observed in the dual-lip profile but it is quite small. Overall, the single-lip profile is significantly higher than the dual-lip one.

Since the heat transfer coefficient is an essential parameter to describe heat transfer between the bubble surfaces and cooling air, several correlations to evaluate it have been proposed in the literature, see Table 2. Numerical analysis was carried out for heat transfer between the bubble and the cooling air as well as the velocity of the cooling air around the bubble at different BUR conditions for both of air rings. The simulation inside the air ring indicated that variation of the maximum velocity (Vmax) around the bubble was independent of the heat transfer coefficient, for both air rings, and under low and high BUR. Therefore, correlations of the form $h = aV_{\max}^{b}$ (a and b are model constants) were considered not suitable for predicting flow and heat transfer inside the air-ring.

Outside the air ring the maximum velocity profile exhibits the same trend as the heat transfer coefficient. Figure 8 shows the logarithm of the heat transfer coefficient versus the maximum velocity for single-lip air ring. The relationship is nearly linear on a log\log plot. The regression coefficient R^2 is almost constant for different BUR, indicating that $h = aV_{max}^b$ is adequate for various BUR bubbles produced by the single-lip air ring. The values of constants in the function depend on BUR, i.e. $h = 16.6V_{max}^{0.56}$ for high BUR, and $h = 3V_{max}^{1.4}$ for low BUR. The function for low BUR is nearly coincident with the Menges and Predohl model.

Figure 9 displays the variation of heat transfer coefficient with the maximum velocity for dual-lip air ring, where the regression coefficient R^2 decreases from 0.98 to 0.86 with a BUR increasing from 1 to 3, indicating that such a simple correlation is a better fit for lower BUR. There are two regions in the results for higher BUR with a shape transition. The relationship between the heat transfer coefficient and the maximum velocity in each region is almost linear on a log\log plot with different powers. This seems similar to a transition from a laminar to a turbulent regime.

At the bubble surface, the flow can be defined as consisting of two regions, such as an inner layer or jet between the bubble surface and the position corresponding to the maximum air velocity, and an outer layer or jet between the latter position and infinity, as illustrated in Figure 10. The maximum velocity just outside the inner layer is considered to be the result of the effect of heat transfer taking place according to the function $h = aV_{max}^b$. On the other hand, the heat transfer between the bubble surface and the cooling air is also affected by the turbulent characteristics in the outer layer that propagates into the inner layer. Since the characteristics of the flow appear to be uniquely determined by Reynolds number, heat transfer rate can be described very effectively by correlating it with the Reynolds number.

In order to generalize the results, the heat transfer rate is expressed in terms of the Nusselt number (Nu). The Nusselt and Reynolds numbers (Re) corresponding to the various BURs along the axial distance are listed in Table 3. Based on the clearance of the single-lip air ring, Reynolds number was found to exceed 10^4, which verifies the flow as being turbulent. For lower BUR, as the flow at the bubble surface moved downstream the Reynolds number decreased for both inside and outside the air ring. For higher BUR, the Reynolds number decreased inside the air ring and increased outside it, along the axial distance.

The Reynolds number of the flow for the dual-lip was smaller than that for the single-lip air ring at the same airflow rate. For BUR = 3, as the flow at the bubble surface moved downstream from 90 mm to 250 mm the Reynolds number changed from 8800 to 29500, which seems to indicate a transition from a laminar to a turbulent regime. This may give a reasonable explanation for the sharp transition, observed for higher BUR in Figure 9.
It seems there is no similar tendency related to the Reynolds number along the downstream for both air rings and different BUR. It was found, however, that the Reynolds number is a function of the Nusselt number. Inside the air ring, the function is totally independent of the BUR and the air ring type (single- or dual-lip). This function can be, approximately, expressed as follows:

$$Nu = \mathrm{Re}^{0.56} \tag{9}$$

Outside the air ring, the constant "n" in the function $Nu = \mathrm{Re}^n$ depends on the variation of BUR. An exception appears at z in the range of 90-110 mm. This seems to be a combination of the Venturi effect and mixing of the jets from the upper lip.
Velocity contours inside the air ring, plotted on axi-symmetry cross sections of the simulation domain in Figure 11, exhibit a complex flow pattern. The simulation results indicate that, even when the same inlet airflow rate was used, the flow configurations have noticeable difference for single- and dual-lip air rings. The curvature of the

streamlines at the entrance of the lower lip was observed for the single-lip air ring only. For the dual-lip air ring, a small recirculation pattern is observed at the separation flow point. The flow then splits into two jets, resulting in a lower downstream air velocity than that found for the single-lip air ring. For the recirculation flow zone after the air ring gate, the size of the vortex core is larger and has a higher air velocity for single-lip air ring, where the flow attaches to the bubble surface. Since the recirculation flow region has significant influence on the heat transfer rate, such varied flow configurations for the single- and dual- lip air rings play some role in explaining results inside the air ring presented in Figures 4 and 5.

Velocity vectors of the cooling air, for flow generated by different air rings at different BUR, are shown in Figure 12. For lower BUR, the heat transfer rate is lightly enhanced for the dual-lip air ring due to impinging jets from the upper lip and the main part of air ring. This is responsible for the higher heat transfer coefficient away from the dual-lip air ring as shown in Figure 5. For higher BUR, the behavior of the impinging flow appears to be more complex. First, the heat transfer rate is enhanced by the Venturi effect due to the increase in bubble diameter as compared to a BUR of 1, for both air rings. The degree of enhancement depends on the gap formed between the bubble surface and the air ring. These phenomena are well known and are in correspondence with the results of other investigations [18 and 25]. Furthermore, as shown in Figure 12, the higher velocity region becomes wider with increasing distance from the die for both air rings. A larger inner layer observed for the flow pattern produced by dual-lip indicates that the distance between the maximum air velocity and the bubble surface is increasing with the volumes of air injected by the upper lip of the air ring. The larger the inner layer, the more important the effects of the turbulent character of the outer layer on the heat transfer. On the other hand, the Reynolds number is increased by a combination of Venturi effect and jet mixing for the dual-lip air ring, resulting in a downstream flow which seems to be in transition. This combined effect is enhanced with increasing BUR. This is the reason why the fit is not good for the relationship between

the heat transfer coefficient and the maximum velocity $h = aV_{max}^{b}$, cited in the literature, at higher BUR for the dual-lip air ring.

CONCLUSIONS

The paper addressed numerical and experimental studies of heat transfer in film blowing by comparing the characteristics and performance of flow produced by both single and dual orifice air rings at different processing conditions. The observed flow structure is highly complex and the predicted results have shown that the boundary conditions and bubble shape as a result of various airflow rates have a significant influence on the heat transfer rate. The simulations revealed that a relationship between the heat transfer coefficient and the maximum velocity in the literature ($h = aV_{max}^{b}$), is good outside the single-lip air ring and the dual-lip air ring at the lower BUR. The cooling jet flow on the bubble surface moves downstream with a changing Reynolds number. The Nusselt number inside the air ring depends on $(Re)^{n}$. The correlation between them is independent of the various BURs, and of air ring type (single- and dual-lip). Such a simple correlation could be used to improve die design by predicting flow and heat transfer inside the air ring.

REFERENCES

1. Kamal, M. (2002). Processing-Structure-Property Relationships in Polyolefin Films, *Proceedings Canadian Society of Rheology's Polymer Technology Symposium (in Montreal Canada): Polymer films and fibers 2002*, 7-8
2. Petrie, C.J.S., (1975). A comparison of Theoretical Predictions with Published Experimental Measurements on the Blown Film Process, *AIChE Journal*, **21(2):**275-282

3. Wagner, M.H., (1976). Ein Rheologisch-Thermodynamisches Prozessmodell Des Folien-Blasverfahrens, Ph.D. Thesis, IKT Stuttgart, Germany
4. Yeow, Y.J. (1976). Stability of Tubular Film Flow: A Model of the Film-blowing Process, *Fluid Mech.*, **75(3):**577-591.
5. Gupta, R.K., Metzner, A.B. and Wissbrun, K.F., (1982). Modeling of Polymeric Film-Blowing Process, *Polym. Eng. & Sci.*, **22(3):**172-181.
6. Luo, X., and Tanner, R. (1985) A Computer Study of Film Blowing, *Polym. Eng. & Sci.,* **25(10):**620-629.
7. Cain, J.J., and Denn, M.M. (1988) Multiplicities and Instabilities in Film Blowing, *Polym. Eng. & Sci.*, **28(23):**1527-1541.
8. Campbell, G.A., Ganesh, N., Campbell, S. and Burl, L. (2003) An Investigation into the Cooling of Blown Film, *Proceedings SPE's ANTEC 2003*, 49-53
9. Kanai, T. and White, J.L. (1984) Kinematics, Dynamics and Stability of the Tubular Film Extrusion of Various Polyethylene, *Polym. Eng. & Sci.*, **24(15):**1185-1201
10. Nagarajan, G., and Campbell, G.A. (1995) Experimental Determination of Heat Transfer Coefficient in Blown Film Process, *Proceedings SPE's ANTEC 1995*,162-166
11. Campbell, G., Obot , N., and Cao, B. (1992) Aerodynamics in the Blown Film Process, *Polym. Eng. & Sci.,* **32(11):**751-759.
12. Wolf, D., Feron, B., and Wortberg, J. (1997) Numerical Analysis of Cooling Air Systems in Film Blowing, *Intl. Polym. Process.*, **12(1):**38-44
13. Feron, B., Wolf, D. and Wortberg, J.(1997) Optimized Cooling and Gauge Tolerances in Blown Film Extrusion, *Polym. Eng. & Sci.*, **37(5):**876-881.
14. Akaike, O., Tsuji, T., and Nagano, Y. (1999) Simulation Of Blown Film Process Taking Account Of Cooling-Air Effect, *Intl. Polym. Process.*, **14(2):**168-174.
15. Hauck, J., and Michaeli, W. (1999) Investigation into the Cooling Characteristics of Blown Film Extrusion Lines, *J. Reinfd. Plas. & Comp.*, **18(10):**895-905.

16. Sidiropoulos, V., Wood, P.E., and Vlachopoulos, J. (1999) The Aerodynamics of Cooling of Blown Film Bubbles, *J. Reinfd. Plas. & Comp.*, **18(6):**529-538.
17. Sidiropoulos, V., and Vlachopoulos, J. (2000) An Investigation Of Venturi and Coanda Effect in Blown Film Cooling, *Intl. Polym. Process.*, **15(1):**40-45.
18. Sidiropoulos, V., and Vlachopoulos, J. (2000) The Effect of Dual-Orifice Air-Ring Design on Blown Film Cooling, *Polym. Eng. and Sci.*, **40(7):**1611-1618.
19. Sidiropoulos, V., and Vlachopoulos, J. (2002) The Aerodynamics of Cooling of Blown Film Bubbles, *J. Reinfd. Plas. & Comp.*, **21(7):**629-637.
20. Gao, N., Li, S., and Ewing, D. (2005) Investigation of the Cooling Jets Used in the Blown Film Process, *Intl. Polym. Process.*, **20(1):** 68-77
21. Yakhot, V. and Orszag, S.A. (1986) Renormalization Group Analysis of Turbulence, 1. Basic Theory, *J. of Scientific Computing*, **1(1):**3-51.
22. Lam, S.H. (1992) On the RNG Theory of Turbulence, *Physics of Fluids A*, **4(5):**1007-1017
23. Fluent Inc., "Fluent User's Guide", Version 6.1 (1998)
24. Incropera, F.P., and DeWitt, D.P., Fundamentals of heat and mass transfer, 2nd ed. (1985): John Wiley & Sons, Hoboken, N.J.
25. Zhang, Z., Lafleur, P.G. and Bertrand, F. (2006) Effect of aerodynamics on film blowing process, *Intl. Polym. Process.*, **21(5):** 527-535.

Table1. Properties of the LDPE used

Properties	Melt Index (g/10min)	Density (g/cm^3)	Heat capacity (J/kg*K)	Melting point (K)
Values	0.88	0.9239	2300	385

Table2. Various models to predict the heat transfer coefficient [10]

MODEL	CORRELATION
Zippenfeld(1971)	$h = 7.11(V_{max})^{0.78}$
Menges and Predohl(1972)	$h = 3.3(V_{max})^{1.5}$
Petrie (1974)	$h = 4(V_{max})^{1.5}$
Kanai and White (1984)	$h = 0.043K_{air}(\mathrm{Re})^{0.78}/L$

Table3. Influence of Reynolds number on the heat transfer

AD (mm)	Single lip air ring						Dual lip air ring					
	BUR=1			BUR=3			BUR=1			BUR=3		
	$Nu*10^{-2}$	$Re*10^{-4}$	logNu/logRe	$Nu*10^{-2}$	$Re*10^{-4}$	logNu/logRe	$Nu*10^{-2}$	$Re*10^{-4}$	logNu/logRe	$Nu*10^{-2}$	$Re*10^{-4}$	logNu/logRe
30	4.84	4.96	0.57	4.97	4.86	0.57	3.64	2.65	0.58	3.57	2.69	0.56
40	4.23	4.88	0.56	4.23	4.88	0.56	2.94	2.46	0.56	2.83	2.50	0.56
50	3.91	4.69	0.56	3.99	4.59	0.56	2.59	2.32	0.55	2.54	2.19	0.55
60	3.68	4.44	0.55	3.58	4.60	0.55	2.37	2.06	0.55	2.31	2.00	0.55
70	3.36	4.06	0.55	3.52	4.23	0.55	2.22	1.79	0.55	2.12	1.74	0.55
80	3.20	3.62	0.55	3.24	3.98	0.55	2.03	1.54	0.55	1.98	1.24	0.56
90	2.99	3.27	0.55	3.12	3.73	0.55	1.89	1.21	0.56	1.80	0.88	0.57
110	2.32	2.96	0.53	2.69	2.19	0.56	1.43	1.35	0.52	1.39	0.91	0.54
130	2.02	2.57	0.52	2.62	3.28	0.54	1.19	1.23	0.51	1.19	1.25	0.51
150	1.70	2.23	0.51	2.47	3.37	0.53	1.03	1.20	0.49	1.14	1.31	0.50
170	1.35	2.07	0.49	2.27	3.61	0.52	0.90	1.37	0.47	1.13	1.19	0.50
190	1.13	1.97	0.48	2.16	4.64	0.50	0.81	1.31	0.46	1.21	1.53	0.50
210	1.02	1.88	0.47	2.35	4.73	0.51	0.82	1.33	0.46	1.48	1.81	0.51
230	0.97	1.71	0.47	2.48	4.89	0.51	0.86	1.33	0.47	1.64	2.87	0.50
250	0.92	1.60	0.47	2.56	4.81	0.51	0.87	1.32	0.47	1.72	2.95	0.50
270	0.86	1.44	0.47	2.56	4.60	0.52	0.87	1.29	0.47	1.82	2.87	0.51
290	0.80	1.38	0.46	2.44	4.35	0.51	0.84	1.29	0.47	1.89	2.39	0.52

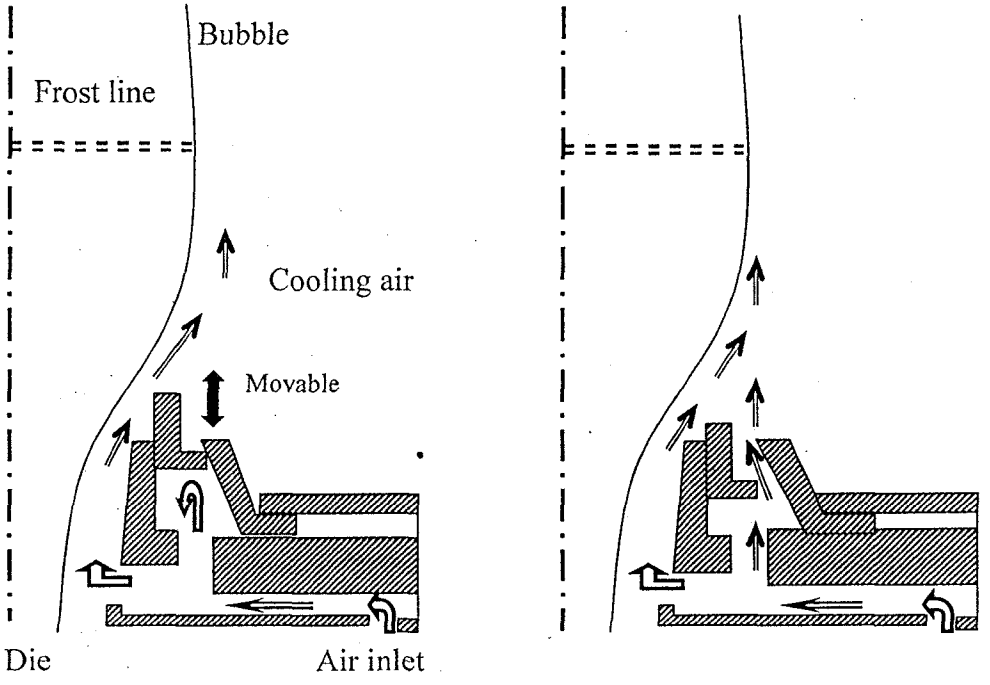

Figure 1 Schematics of different air ring types (left: single lip; right: dual lip).

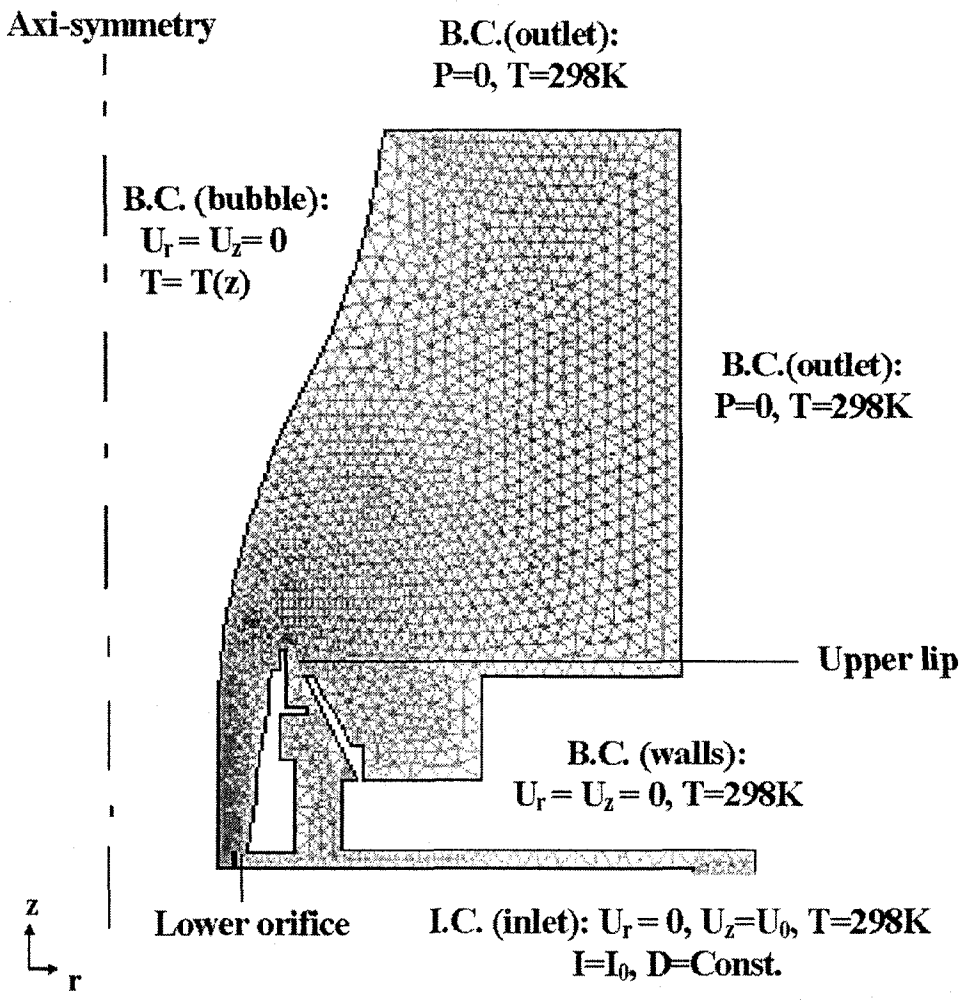

Figure2 Computational domain with the boundary conditions

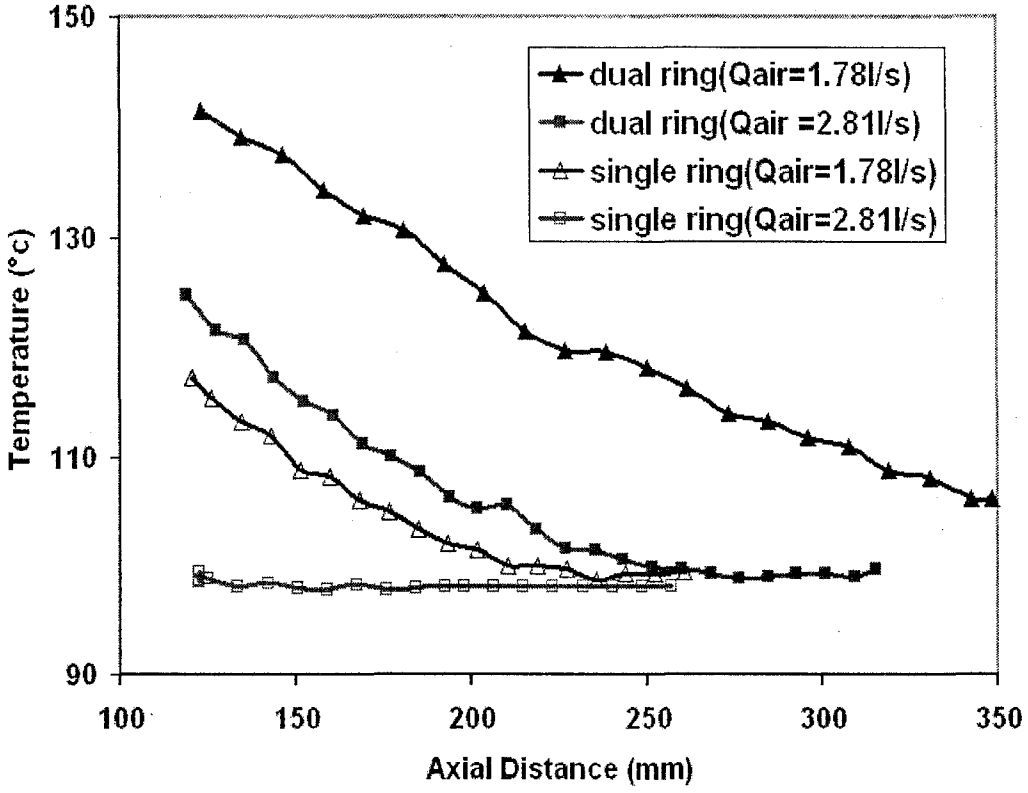

Figure3 Temperature profiles for single- and dual-lip air rings at different airflow rates (BUR=1).

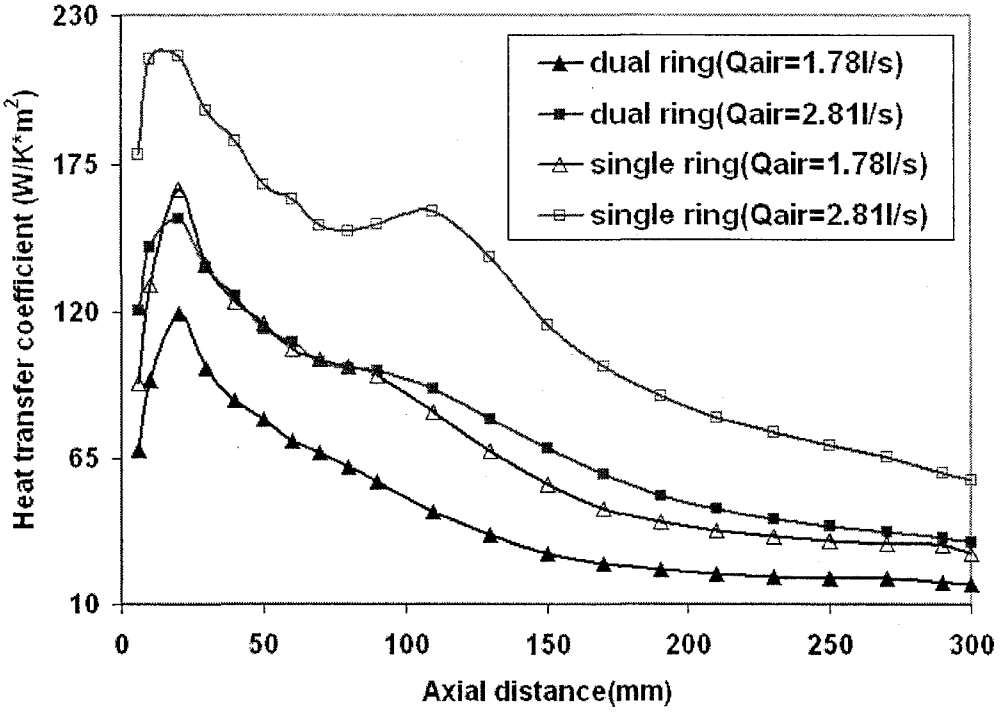

Fig.4 Heat transfer coefficient profiles for single- and dual-lip air rings at different air flow rates (BUR=1).

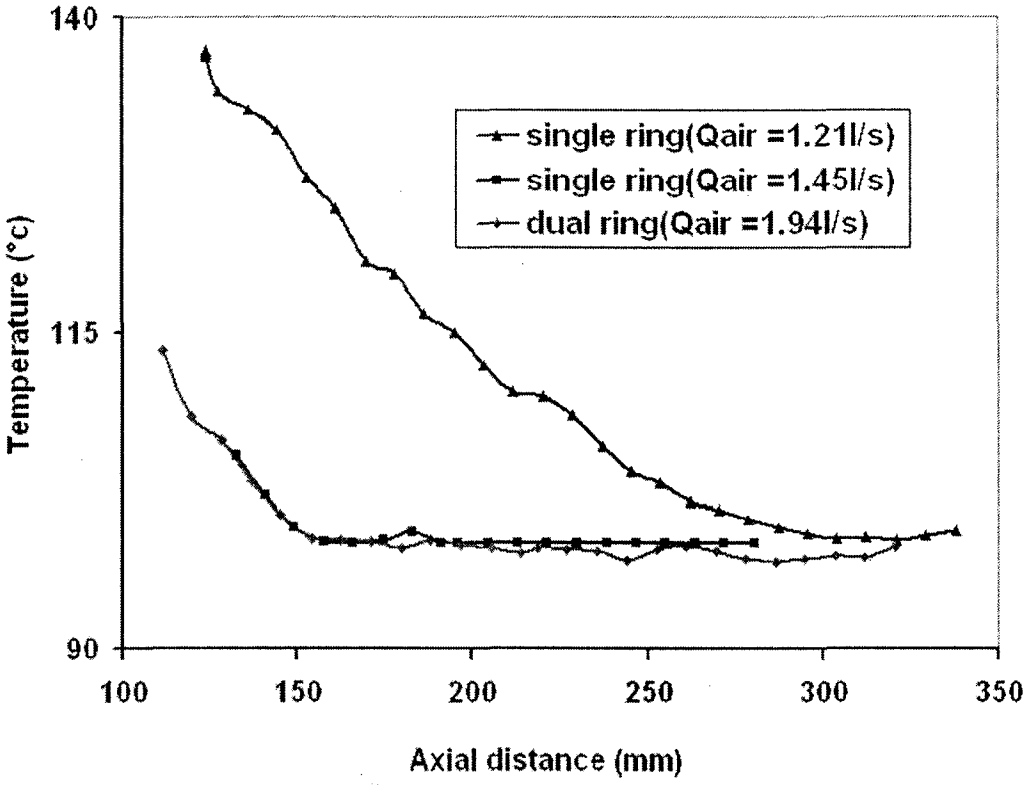

Figure 5 Temperature profiles for single- and dual-lip rings (BUR=2).

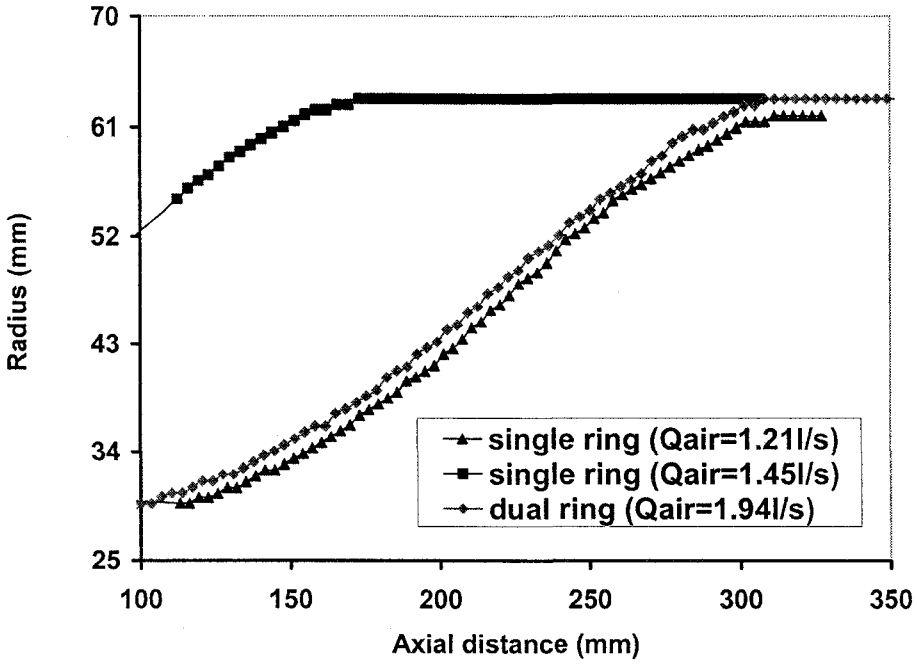

Figure 6 Radius profiles for dual-lip and single-lip air rings (BUR=2).

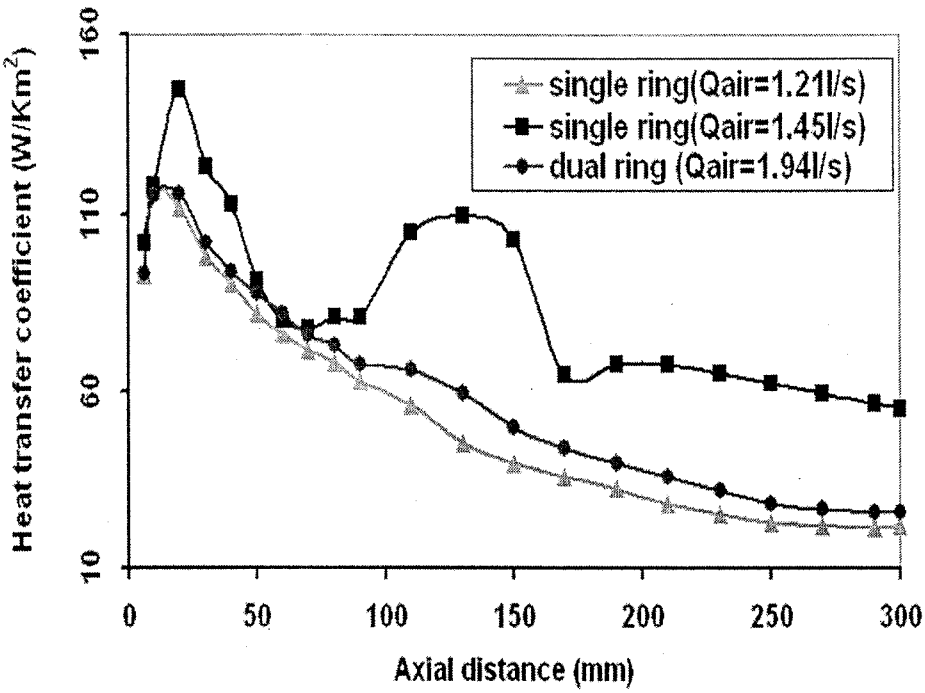

Figure 7 Heat transfer coefficient profile for single- and dual-lip air rings.

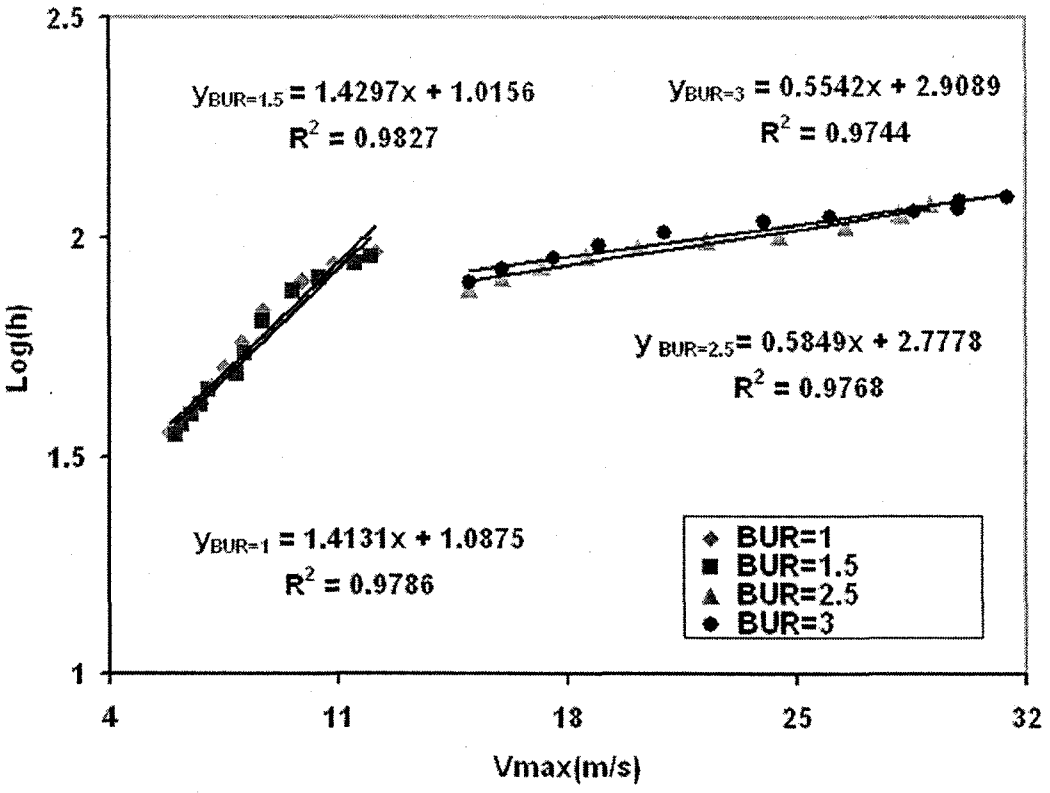

Figure8 Linear regression log (h) versus Vmax outside the single lip air ring at different BUR

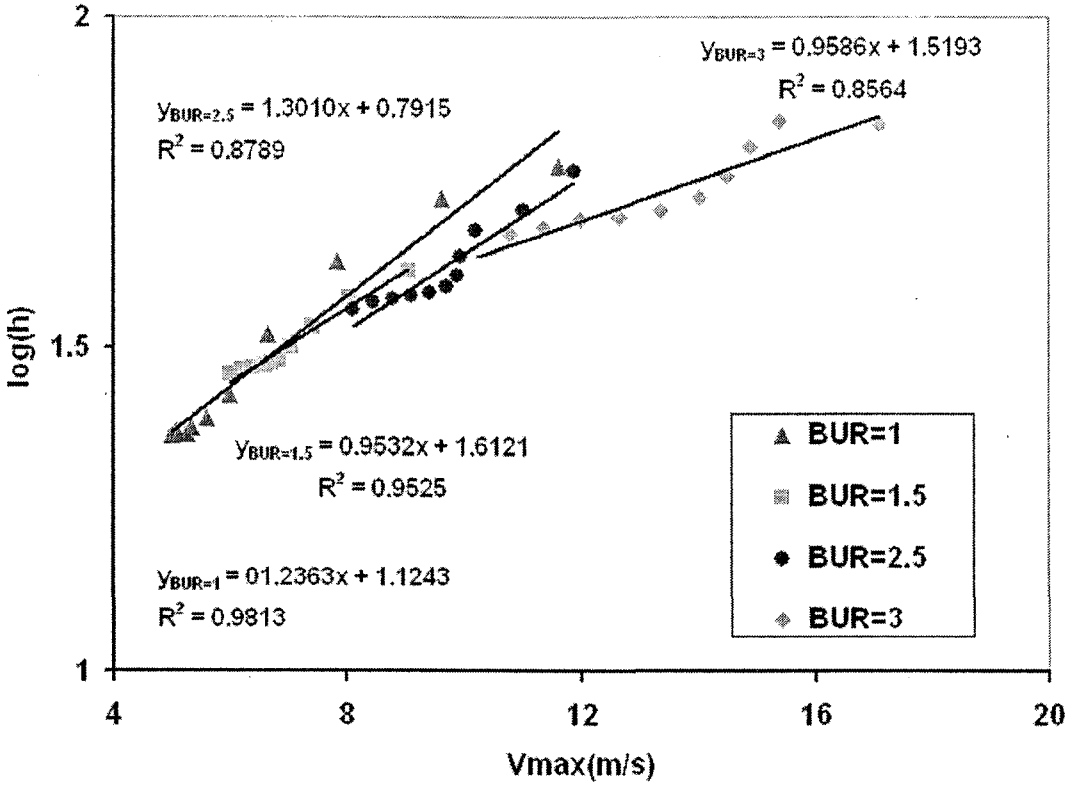

Figure 9 Linear regression log (h) versus Vmax outside the dual lip air ring at different BUR

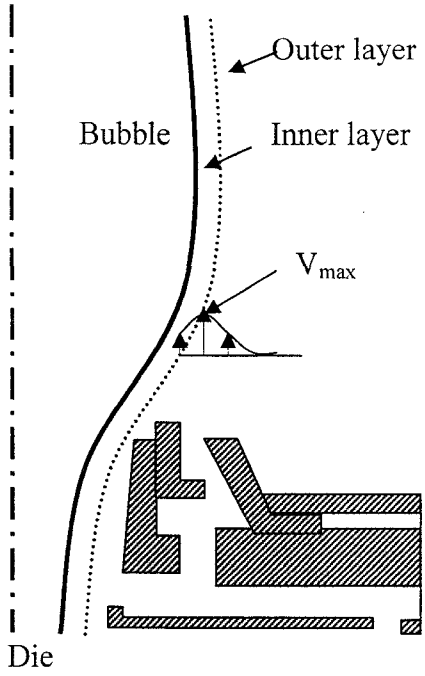

Figure 10 impinging jet nomenclatures

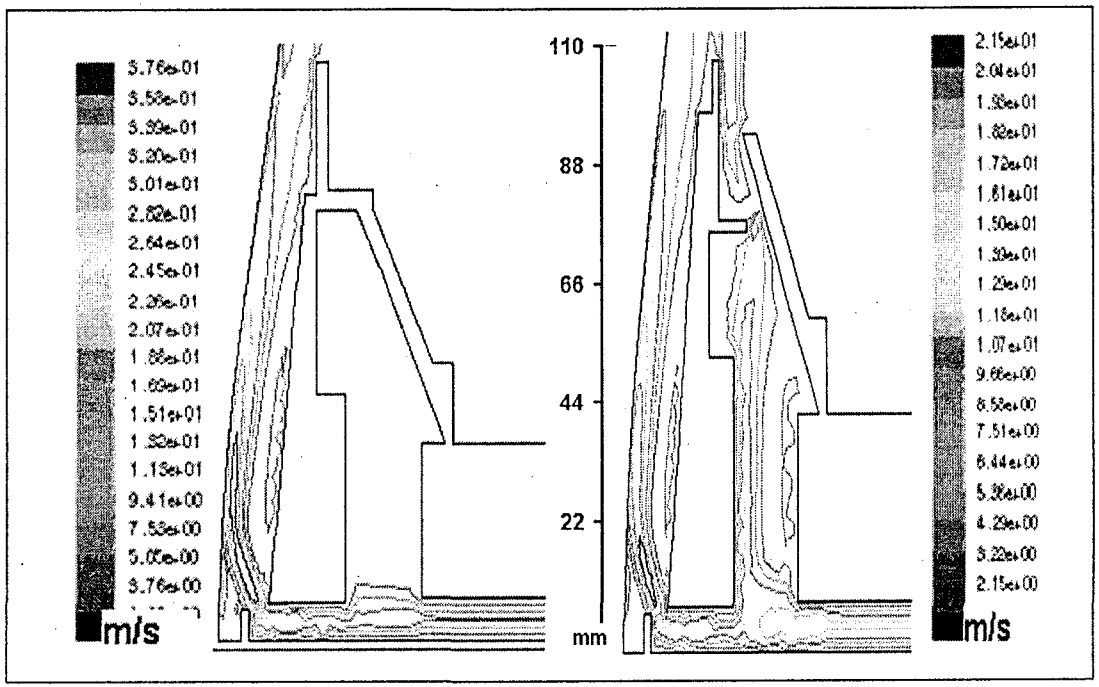

Figure11 Velocity contours inside the air ring
(BUR=2 and left: single lip air ring, right: dual lip air ring)

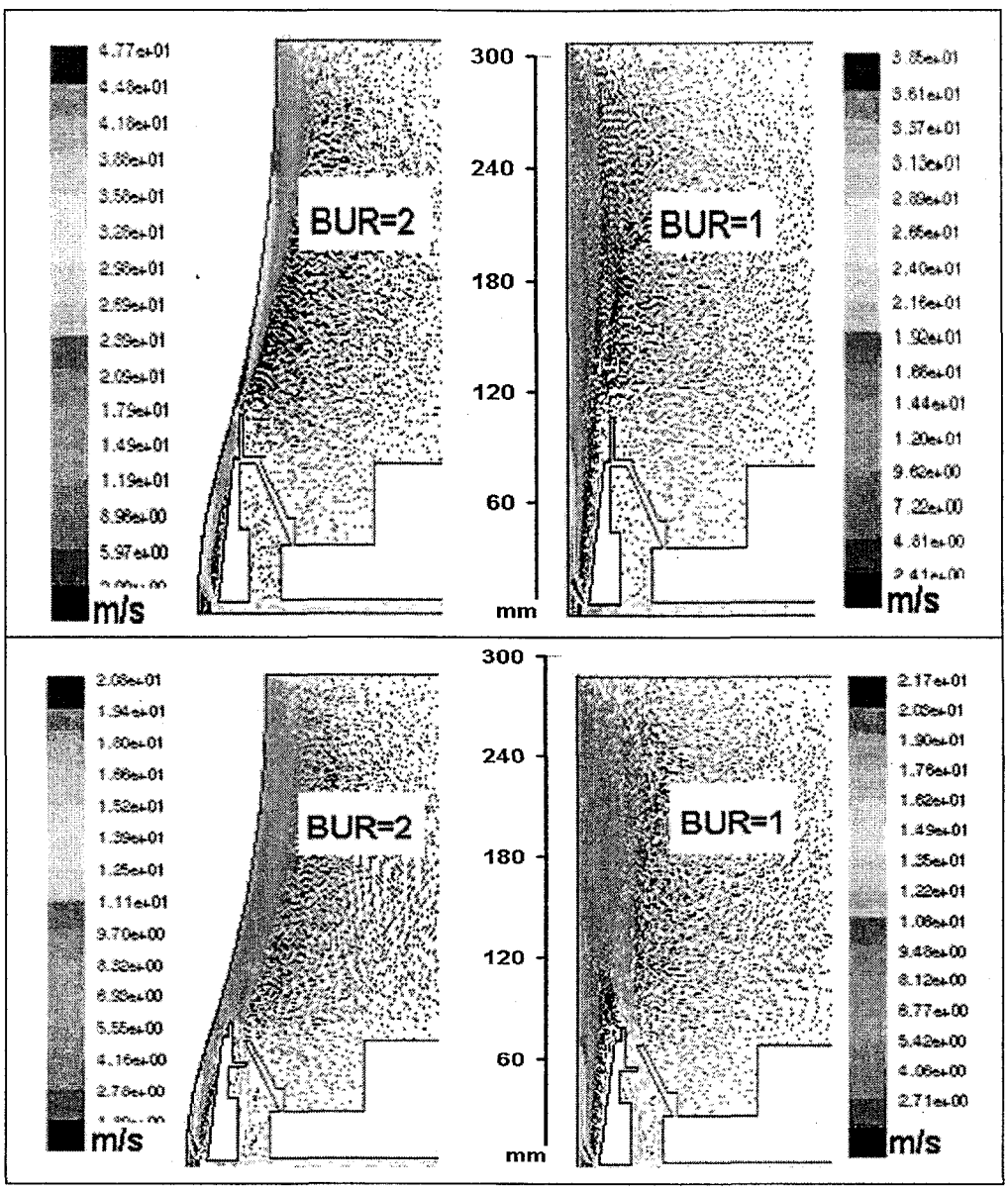

Figure12 Velocity vectors in the simulation volume at different BUR
(top: single-lip air ring, bottom: dual-lip air ring)

APPENDIX E : Investigation of Blown Film Instability Induced by Air Cooling

Publication Polymer Engineering and Science (submitted)

*Z. Zhang, P.G. Lafleur**

Department of Chemical Engineering, Ecole Polytechnique de Montréal, CREPEC, Montreal, QC. H3C 3A7 Canada

Abstract

This paper deals with the bubble instabilities induced by cooling air flow rate at different Take-Up-ratio (TUR) and Blow-Up-ratio (BUR) conditions in the film blowing process. Experimental methods to monitor the on-site bubble instability included an in-line scanning camera system to record the bubble oscillation and a manometer mounted on the die to measure the internal pressure corresponding to the radius variation. A good correlation between the bubble instability and the pressure inside the bubble has been obtained. Experimental results indicated that varying the cooling air flow-rate at different TURs and BURs conditions produced significant differences in the dynamics of bubble instability. While a higher cooling air rate stabilized the bubble for a high BUR, the bubble was destabilized for a low BUR. The bubble with a high TUR sustained greater aerodynamics forces acting on the bubble surface, resulting in a broader operating range of stable operation. Finally, a numerical simulation using a RNG (Re-Normalization Group), k-ε model and Fluent software was performed, to analyze the effects of momentum and heat transfer, from the cooling air to the polymer film on bubble instability.

Introduction

Instability in polymer processes, which have free surface flows, such as fiber spinning, cast film and blown film, limits the rate of industrial production and may give rise to

unacceptable production quality. Bubble instability is one of the most difficult problems observed in blown film extrusion. Seven common types of instability were described by Waller [1] including: Draw Resonance (The periodic oscillation of the bubble diameter); Helical instability (A helical motion of the bubble); FLH (Frost-Line-Height) oscillation (Variation in the FLH location); Bubble sag (When the bubble sits on the air ring); The bubble tears off the die; Bubble flutter; and Bubble breathing.

Instabilities, whether caused by non-optimized processing conditions, equipment malfunction or unsuitable raw material, can severely limit the maximum production rate. In order to overcome instabilities in the film blowing process, it is necessary to understand the reason and mechanism of their appearance. There have been numerous literatures on the subject of instability in film blowing. One of the first experimental results was presented by White and coworkers [2,3,4], who compared the bubble stability using different molecular structures of polyethylene and found that the resins containing LCB (Long Chain Branching) are the most stable, followed by the broad MWD (Molecular Weight Distribution) linear resins. The narrow MWD resins are the most unstable. In other words, LDPE (Low Density Polyethylene) has the widest operation window, and LLDPEs (Liner Low Density Polyethylene) with broad MWD are unstable. Improving bubble stability of LLDPE with blends of LDPE has been reported by Obijeski and Pruitt [5]. Micic. et al [6] correlated this stabilizing effect with enhanced strain hardening. Ghaneh-Fard [7] studied the stability behavior of Polypropylene (PP) and showed the relative order of stability, in comparison with three type of polyethylene. According to him the stability order is as follows: LDPE>HDPE (High Density Polyethylene) >LLDPE>PP. A significant effort in the aforementioned investigations has been directed toward understanding the effect of polymer properties on bubble stability. Han et al [8, 9] focused on the importance of processing conditions specifically; they proposed that a lower polymer melt temperature provides a more stable HDPE and LDPE bubble. Yeow [10] was the first to try a theoretical investigation of bubble instability using a linear stability analysis of a Newtonian film under

isothermal conditions. Cain and Denn [11] extended Yeow's analysis to a viscoelastic upper-convected Maxwell fluid. None of them seem to provide reasonable agreement with experimental observations [2, 8 and 9]. Huang [12] used a pressure transducer to detect variations in the internal bubble pressure and correlated them to oscillations in the bubble diameter. Ghijsels et al. [13] demonstrated that a low tension bubble induced by a small axial take-up force becomes sensitive to surrounding air flows and gravity forces, resulting in bubble instability. Sweeney and Campbell [14] reported on the importance of interaction of various process variables, polymer properties and air ring design on bubble instability. In the course of an experimental study, Butler [15] investigated process variables, such as melt temperature, FLH, BUR, and film thickness, to determine the influence of bubble stability on the maximum output rate. Laffague and co-workers [16] developed a new system using an in-line scanning camera with seven mirrors to study the stability of LLDPE; they concluded that the new device can capture quantitatively characteristics of all bubble instabilities. They, also, concluded that LLDPE instabilities are enhanced by increasing the TUR, BUR, and FLH. Kim et al [17] extended Laffague's work [16] to investigate the dynamics and criteria of bubble instabilities, for three commercial film-grade polyethylene resins, LmPE (metallocene-catalyzed linear polyethylene), LLDPE, and LDPE, in a broad range of TURs, BURs and FLH. They came up with a graphical quantification approach and presented stability maps of the operating condition under which a stable bubble can be obtained.

The cooling air from the air-ring is one of the key factors to stabilize or destabilize the bubble in the film blowing process. The available literature about the subject, though, is quite limited due to the complex character of the flow field involved. The development of CFD (Computational Fluid Dynamics) technology provides an effective method to better understand the complex aerodynamic phenomena in film blowing. The numerical investigations by Feron et al, [18] focused on the aerodynamics produced by dual-lip air-rings. They noted that the occurrence of vortices caused by the angle-of-attack, in conjunction with the bubble shape, were responsible for the unstable bubble behaviour.

Sidiropoulos and Vlachopoulos [19-21] carried out numerical simulations of the aerodynamics of cooling air in the film blowing process, employing an RNG k-ε turbulent model and commercial software (Fluent). They published several papers to examine the flow fields produced by different dual-lip air-rings compared to single-lip air-rings. They noted that vortices produced between the bubble and the forming cone can cause a negative static pressure around the bubble, which was assumed to stabilize the bubble. More recently, Gao et al. [22], experimentally, measured the pressure distribution on the bubble surface for a rigid model bubble and demonstrated the existence of a negative static pressure region on the bubble surface, due to the deformation of the bubble at different processing conditions. However, there has not been any detailed experimental study that correlates the bubble instability to the aerodynamics of the cooling air, under different processing conditions. Therefore, the objective of this work is to investigate the relationship between bubble instability and aerodynamics of cooling jets.

Experimental

Blown Film Extrusion

A 45mm Killion single screw extruder with a helical die (out diameter = 63.5mm, and die gap at exit =3mm) was used for the production of blown films. The extrusion was carried out at a temperature of 180 °C. The polymer flow rate was maintained at about 2.5 ±0.1 kg/h for all experiments. The polymer used in this study is LDPE supplied by DOW Chemical Co., with a melt index of 0.88g/10min, a density of 0.923g/cm^3, a heat capacity of 2300 J/kg*K , and a melting point of 385K, respectively.

In the film blowing process, a molten polymer tube is extruded from an annular die and drawn upward by a nip roll device. Simultaneously, the tube is inflated by introducing a small amount of air inside the tube, which transforms the blown tube into a bubble shape. The impinging air from a dual-lip air-ring, located just above the die, cools the bubble reducing the temperature of the polymer from the die exit to the FLH. The nip rolls do

not only provide axial tension but also form an air-tight seal, so that a constant pressure could be maintained in the bubble. The target TUR, BUR and FLH values are achieved by adjusting the speed of nip rolls, the amount of air inside the bubble, and the cooling air flow rate, respectively. However, the cooling air flow-rate causes variations of FLH, bubble shape and bubble stability. In this study, the influence of cooling airflow on bubble instabilities was investigated, at different values of BUR and TUR. The experimental design is summarized in Table1.

Measurements

The volumetric air flow-rate through the air-ring was measured by multiplying the air velocity by the wetted area. The air velocity was obtained with an FMA-905-V air velocity transducer manufactured by the OMEGA Co., and calibrated in a NIST-traceable wind tunnel. The temperature at the bubble surface was measured as a function of vertical distance from the die by an infrared pyrometer (IRCON 3400). The pressure inside the bubble was measured using a manometer mounted on the die. The bubble diameter profile was determined by a video camera. After the process was started and gotten underway, the screw and nip rolls rotations were abruptly stopped and the bubble was immediately solidified by cooling air. The thickness of the frozen bubble was then measured using a micrometer.

Bubble instabilities were, experimentally, measured using the in-line scanning camera system developed by Laffague et al. [16] as shown schematically in Fig.1. This system can provide four parameters as output: 1). Eccentricity, d, 2) Rotation angle, α, 3) Radii of the left and right sides of the bubble (R_{Left} and R_{Right}), and 4) Ratio of the two radii. The relationships between these parameters and geometrical variables are as follows:

$$\alpha = \arctan(Y_c / X_c) \tag{1}$$

$$d = \sqrt{X_c^2 + Y_c^2} \tag{2}$$

$$\text{Radius ratio} = R_{Left} / R_{right} \tag{3}$$

Where X_c and Y_c are the bubble centre coordinates

This system gives continuous information during the transition between stable and unstable zones. The cooling flow rate was increased or decreased gradually in order to generate unstable bubbles. Detailed dynamics of bubble instabilities were investigated as a function of time, at various flow-rates of the cooling air and for different TURs and BURs.

Simulation

The typical Reynolds number, based on the air-ring clearance and air velocity, was found to exceed 10^4. Therefore, the cooling air surrounding the bubble gives rise to a very complex turbulent flow. The Reynolds averaged Navier-Stokes equations were used for the calculation of the momentum and heat transfer of the cooling air stream. In this work, the RNG k-ε model [23], an improved version of the standard k-ε model, was employed to achieve turbulence closure. Using the effective viscosity (μ_{eff}) defined in the RNG k-ε model, the mean momentum equation for two-dimensional flow can be written as:

$$\frac{\partial(\rho U_i)}{\partial t}+\frac{\partial(\rho U_i U_j)}{\partial x_j}=\frac{\partial}{\partial x_j}\left[\mu_{eff}\left(\frac{\partial U_i}{\partial x_j}+\frac{\partial U_j}{\partial x_i}\right)\right]-\frac{\partial p}{\partial x_i} \tag{4}$$

The turbulent transport of the energy equation is given by:

$$C_p\left(\frac{\partial(\rho T)}{\partial t}+\frac{\partial(\rho U_i T)}{\partial x_i}\right)=\frac{\partial}{\partial x_i}\left[\alpha_h \mu_{eff} C_p \frac{\partial T}{\partial x_i}+U_j \mu_{eff}\left(\frac{\partial U_i}{\partial x_j}+\frac{\partial U_j}{\partial x_i}\right)\right] \tag{5}$$

However, the turbulent models, based on the k-ε elements, do not take into account any wall effect, and are inadequate for the investigation of the momentum near the wall. The enhanced near wall treatment of Fluent [24] was employed at the solid surface in this

study; it can automatically accommodate cells located in the log-law layer, and hence provide a more robust treatment.

Owing to the symmetry of the bubble and the air-ring geometry, a 2D axi-symmetric coordinate system was employed. The adequate meshes generated with the help of Gambit from the Fluent software were used for all subsequent simulations. The air was assumed to be an ideal gas. The ambient temperature was set to 298K. The bubble shape was fixed corresponding to that measured experimentally. Cooling air entered the domain with predetermined velocity ($\overline{V}$), ambient temperature (T), kinetic energy of turbulence (k), and dissipation rate (ε). A no-slip velocity condition was imposed along the bubble surface. During the simulations, the temperature profile along the surface was gradually decreased in accordance with the experimental data. All computational results presented in this paper were obtained from the commercial CFD code FLUENT 6.2.16. The reader is referred to our previous article [25] for more details about the cooling airflow simulation procedure.

Results

The bubble instabilities induced by various flow rates of the cooling air at different TUR and BUR values are presented in this section. Draw Resonance (DR) is considered in this study, which is characterized by the radius variation of the bubble. The radius variation (ΔR) is defined as follows:

$$\Delta R = (R_r - R_s) * 100 / R_s \tag{6}$$

Where R_r is the observed radius, and R_s is the set radius.

Based on their experimental data for various operating conditions with different polymers, Laffague et al. [16] and Kim et al. [17] proposed a radius variation of ±2.5% as the criterion for differentiating various instabilities.

Fig.2&3 exhibit radius and radius variation response for a BUR of 1 at different air flow- rates for different TURs. The cooling air flow-rate was increase gradually by steps

of 0.11l/s. Data was collected once the bubble was completely stable. When the airflow rate was increased from 4.77 l/s to 5.10 l/s at a TUR of 20 as shown in the Fig.2, the radius variation showed a gradual increase from 1.2% to 4.1 %. Typical DR instability was observed with a radius variation of more than 2.5%, upon increasing the air flow-rate from 4.88 to 5.10l/s. All bubbles however showed similar average diameters. As shown in Fig.3, when TUR was set at a high value of 40, a typical stable bubble was maintained with a radius variation of less than 1%, while the air flow-rate was increased from 6.46l/s to 6.68l/s. A further increase of 0.11l/s in the air flow-rate caused a radius variation of up to around 4.6 %, exceeding the critical value of 2.5%, resulting in periodic oscillations. Meanwhile, the radius ratio was close to unity, which demonstrates that the bubble was always axi-symmetric. The average bubble diameter was only slightly larger at a TUR of 40 compared to that at 20. Table 2 shows other effects of the air cooling flow-rate on bubble instabilities at different TUR settings. The air flow-rate producing bubble DR instability increased when TUR was incremented up to a value of 40. Further increase of TUR resulted in a decrease of the cooling air flow-rate which caused DR instability. DR instability can cause film gauge and lay-flat variations, due to different expansions in the Transverse Direction, TD. Process optimization is required to minimize these variations. When TUR was set at 40 (see Table 2), the radius variation of 0.28%, at the most stable state (RVMS), was reduced to a minimum, while the air flow-rate was at a maximum. In addition, the pressure inside the bubble (Data not shown) was simultaneously measured along with bubble radius. The pressure and the bubble radius varied with the same period and in phase. When the DR instability occurred, the variations in pressure were around 10%, which is larger than those observed for stable bubbles. The same observations were reported by Huang [12], who detected bubble instability using a pressure transducer.

The situation is different for a bubble with a BUR of more than 1. Fig.4 shows radius and radius variation response as a function of air flow-rate for a BUR of 1.75 at a TUR of 30. When the flow-rate was set to 1.89 l/s, the radius variation exceeded the critical

value of 2.5%, and periodic oscillations started to take place. The bubble showed typical draw resonance instability with a long-neck shape as presented in Fig.5. As the airflow rate was increased, the bubble shape changed from long-neck to short-neck, and the average diameter of the bubble decreased somewhat. Meanwhile, the radius variation decreased to around 2 %. When the air flow rate was increased to 2.28 l/s, the bubble stabilized. The values of the radii almost overlapped with the radius variation down to 0.4%. The same changes were obtained at a BUR of 2, for a different air flow-rate [25]. However, further increase of the air flow-rate caused an additional variation in the radius when a BUR of 1.75 was used, and the bubble shape remained virtually unchanged as compared to the resulting shape when keeping air flow rate at 2.28l/s. A BUR of 2 resulted in the bubble sitting down on the air ring and collapsing. The value of air flow-rate producing DR instability attains a maximum at a TUR of 50, and a BUR of 1.75. However, at the TUR of 40, a corresponding maximum was found for a BUR of 2 (see Table 3).

The increase in the bubble volume, as the bubble expands from a long-neck to a short neck shape, corresponds to a decrease in the average internal pressure of the bubble. Fig.6 exhibits the corresponding pressure profiles inside the bubble. The average pressure inside the bubble was around 67.5 ± 0.9Pa, for an air flow-rate of 1.89l/s, with a standard deviation of approximately 1.26%. This seems to imply that the use of a single pressure transducer does not detect DR instability for different processing conditions. However, with the increase of air flow-rate to 2.28l/s, the bubble showed a minimal radius variation at the lowest average internal pressure. The same phenomena were observed at the higher BUR values of 2 and 2.5. A further increase of air flow rate, for a BUR of 1.75, dramatically increases the pressure inside the bubble along with an increase in the radius variation. This trend shows that the lowest average internal pressure can be related to the radius variation at a BUR of 1.75.

The bubble shapes for a BUR of 2 at the onset of instability vary as a function of the TUR as shown in Fig.7. At a TUR of 20, the bubble inflates faster with a short neck region. Increasing the TUR increase the angle formed by the film at the position of inflation implying that the bubble at the higher TUR presents a larger operation space considering the variation in air flow rate.

DISCUSSION AND CONCLUSIONS

The experimental observations described earlier indicate that the bubble instabilities depend on a strong level of interaction between various process parameters including, TUR, BUR, and the cooling air flow-rate used. This is most likely due to the effect the different factors and interactions have on the momentum transfer from the cooling air to the polymer film, and the heat transfer from the polymer film to the cooling air. In a previous publication [25], the static pressure along the bubble surface from numerical simulation was reasonably used to analyze the momentum transfer influence on bubble instability. It was shown [25] that the bubble instabilities depend on the static pressure distribution along the bubble surface, and that minimizing the pressure gradient can stabilize the bubble. This result was obtained at the conditions of fixed TUR and a constant amount of inflation air for different BURs. For different TUR conditions, the difference of static pressure between a stable and an unstable (i.e. 2.5% of radius variation) bubble along the surface for a BUR of 1 were obtained from the numerical analysis, and are presented in Fig.8. Certain general trends in the data are clear; the bubble with the higher TUR shows a greater difference of static pressure, resulting in lower susceptibility to instability induced by aerodynamics acting on the surface of the bubble. After setting the TUR to 40, a smaller difference in static pressure is obtained when TUR is increased. This can be simply explained by noticing that the film thickness, (see table 2&3), turned to be a key influencing factor for the bubble instability, if it is reduced to a certain value. Yeow [10] similarly predicted that the film blowing process is always stable unless the thickness reduction is as large as 10^4, this result was cited by Yoon et al [26] in their investigation. At a BUR higher than 1, static pressure

distribution of a stable bubble at a high TUR produces instability at a lower TUR. This implies that a bubble with a high TUR is capable of sustaining greater force caused by the aerodynamics acting on the surface of the bubble. Since the shape of the bubble is determined by the cooling air flow-rate under these circumstances, increasing TUR broadens the range of stable operating conditions.

The trace of pressure inside the bubble can provide a warning about the instability of a film blowing operation. The warning signals depend on the BUR of the bubble. The period of the bubble-diameter variation, analyzed using the video camera, matched that of pressure perturbation for a BUR of 1, the amplitude of both oscillation modes must be reduced to a minimum in order to obtain a stable bubble. The fluctuation of internal pressure could not be correlated well with the bubble diameters for a BUR of more than 1. However, a minimum average internal pressure, along with a minimum radius variation indicates that a stable bubble can be obtained. At that point, a further increase in air flow rate will increase the heat transfer and the bubble could become unstable again. As can be seen in Fig.5, the bubble radius increased somewhat with maintaining almost the same shape, when the air flow-rate was increased from 2.28 to 2.37l/s. Such a slight change in radius causes a significant effect on the aerodynamics of the cooling air. Fig.9 shows heat transfer coefficient profiles along the bubble surface, obtained from numerical analysis for different air cooling rates. The heat transfer coefficient went up through a maximum at a location around z = 14mm and then decreased. Another smaller peak appeared at z = 90 mm for both cooling rates. The heat transfer coefficient for an airflow rate of 2.28l/s was higher than that for 2.37l/s inside the air ring ($z \leq 90$mm), resulting in an increase in the temperature of the polymer film and the temperature inside the bubble. This can explain why the internal pressure of the bubble increased when the air flow rate was changed from 2.28l/s to 2.37l/s. Therefore, an increase of the film temperature can cause radius variations; this result is in agreement with the observation of Han and coworkers [8 and 9]

REFERENCES

1. Waller, P., Plastics Tech. online http://www.ptonline.com/articles/200212ts1.html (2002)
2. Kanai, T. and White, J., L., Polym. Eng. Sci. 24 p1185(1984)
3. Minoshima, M. and White, J. L., J. Non-Newt, Fluid Mech., 19 p275 (1986)
4. White, J. L. and Yamane, H., Pure &Applied Chem., 59(2), p193 (1987)
5. Obijeski, T. J., and Pruitt, K. R., SPE ANTEC Tech. papers, p150(1992)
6. Micic, P., Bhattacharya, S. N. and Field, G., Polym. Eng. Sci. V38, n10p1685(1998)
7. Ghaneh-Fard, A., Carreau, P. J., and Lafleur, P. G., AIChE, v42, n5 p1388 (1996)
8. Han, C.D., and Park, J.Y., J. Appl. Polymer Sci. 19, p329 (1975)
9. Han, C.D., and Shetty R., IEC Fundam., 16, p49(1977)
10. Yeow, Y. L., Journal of Fluid Mechanics, v75, p577(1975)
11. Cain, J.J., and Denn, M. M., Polym. Eng. Sci. v28, n23, p1527 (1988)
12. Huang, T. A.,: Advances in Polym. Tech. 8(1) p.65 (1988)
13. Ghijsels, A., Ente, J. J. S. M., and Raadsen, J., Int. Poly. Process., 5 p284 (1990)
14. Sweeney, P. A., and Campbell, G. A., SPE ANTEC Tech. papers, p146(1993)
15. Butler, T. I., SPE ANTEC Tech. papers, 1, p156 (2000)
16. Laffague, J., Parent, L., Lafleur, P.G., Carreau, P. J., Demay, Y. and Agassant, J. F., Intern. Polym. Prosess XVII p347 (2002)
17. Kim, S., Fang, Y., Lafleur, P. G. and Carreau, P. J., Polym. Eng. and Sci., v44, n2 p283 (2004)
18. Feron, B., Wolf, D. and Wortberg, J., Polym. Eng. Sci., v37, n5, p876 (1997)
19. Sidiropoulos, V., Wood, P.E. and Vlachopoulos, J., SPE ANTEC, Tech. papers, p108, (1998)
20. Sidiropolous, V. and Vlachopoulos, J., Polym. Eng. Sci., v40, n7, p1611 (2000)
21. Sidiropoulos, V. and Vlachopoulos, J., J. of reinforced plastics and composites, v21, n7 p629(2002)
22. Gao, N., Li, S. and Ewing, D., J., Intern. Poly. Process, XX, p68(2005)
23. Yakhot, V., Orszag, S. A.: J. science. Comput. v1, p.3 (1986).

24. Fluent Inc., "Fluent User's Guide", Version 6.2 (1998)

25. Zhang, Z., Lafleur, P. G., and Bertrand, F., Intern. Polym. Process, XXI, 5, p527(2006)

26. Yoon, K.S. and Park, C. W., Intern. Polym. Process, XIV, 4, p342(1999)

Table1 Experimental design

BUR	1					1.75					2				
TUR	20	30	40	50	60	20	30	40	50	60	20	30	40	50	60
Air flow rate	Vary gradually to make bubble from stable to unstable														

Table2 Radius variation as function of air flow rate at different TUR and BUR=1

TUR	20	30	40	50	60
Air flow rate at DR (l/s)	4.99	5.34	6.79	6.56	6.12
RVMS* %	1.2	1	0.28	0.38	1
Air flow rate at MS (l/s)	4.49	4.74	6.45	5.69	6.05
Average thickness of film (μm)	106.5	67	44.5	38	29

*RVMS: the radius variation at the most stable state

Table3 Radius variation as function of air flow rate at different TUR

BUR	1.75					2				
TUR	20	30	40	50	60	20	30	40	50	60
Air flow rate at DR (l/s)	1.98	2.09	2.26	2.30	2.24	1.85	1.90	2.06	1.79	1.71
Thickness at DR (μm)	58	38	29	21	16	54	36	25	18	15

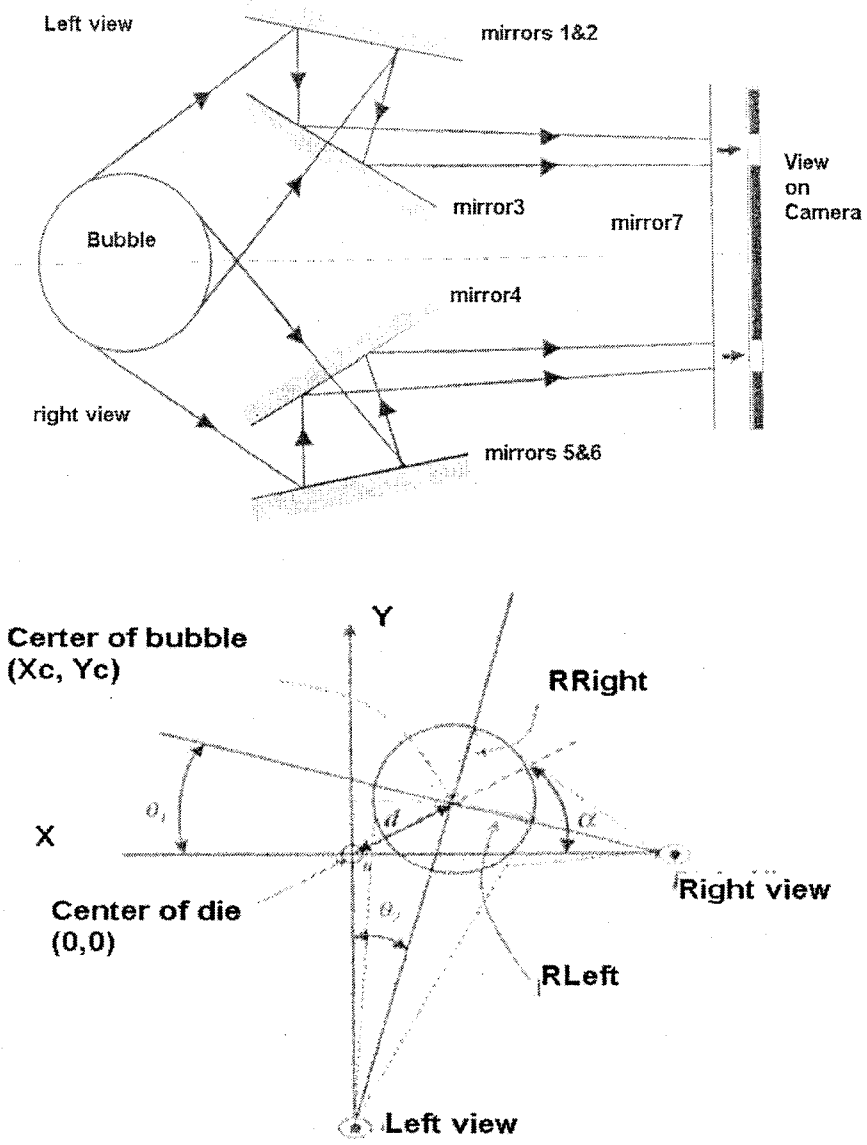

Fig.1 Schematic of bubble instability measurement system (above) and equivalent geometry of the system (bottom)

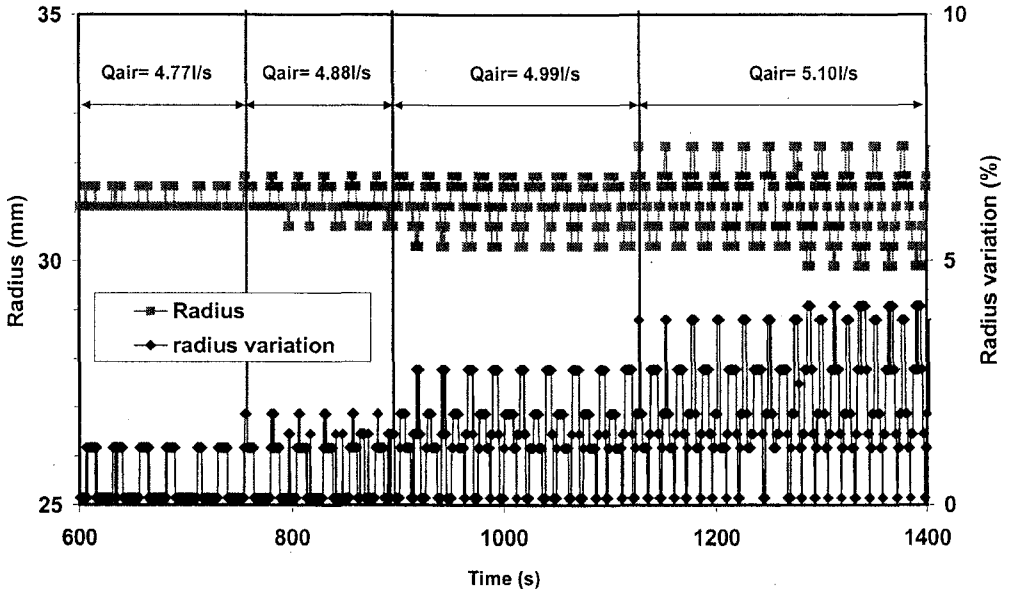

Fig.2 Radius and radius variation response at different air flow rate (BUR=1, TUR=20)

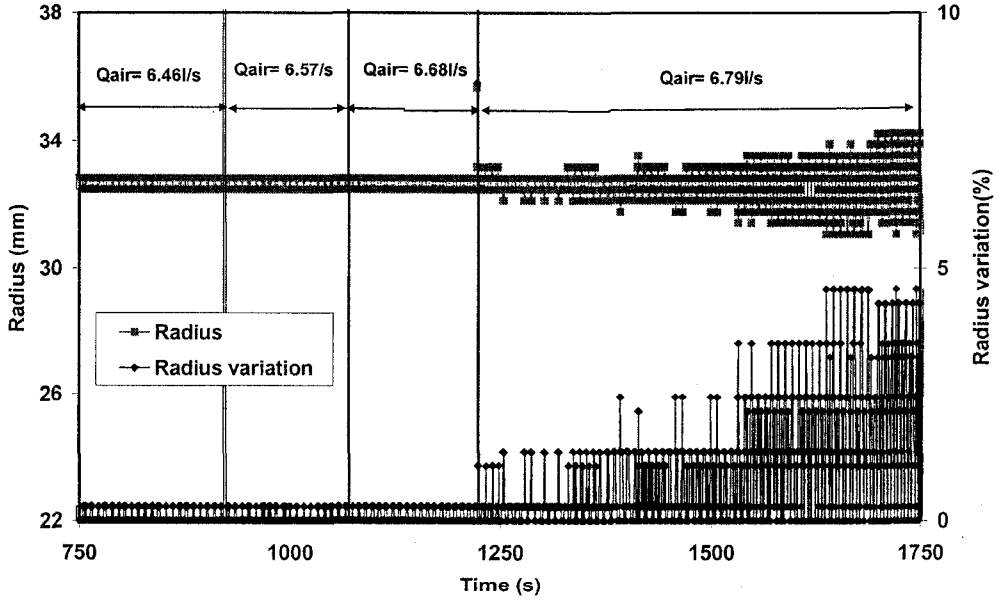

Fig.3 Radius and radius variation response at different air flow rate (BUR=1, TUR=40)

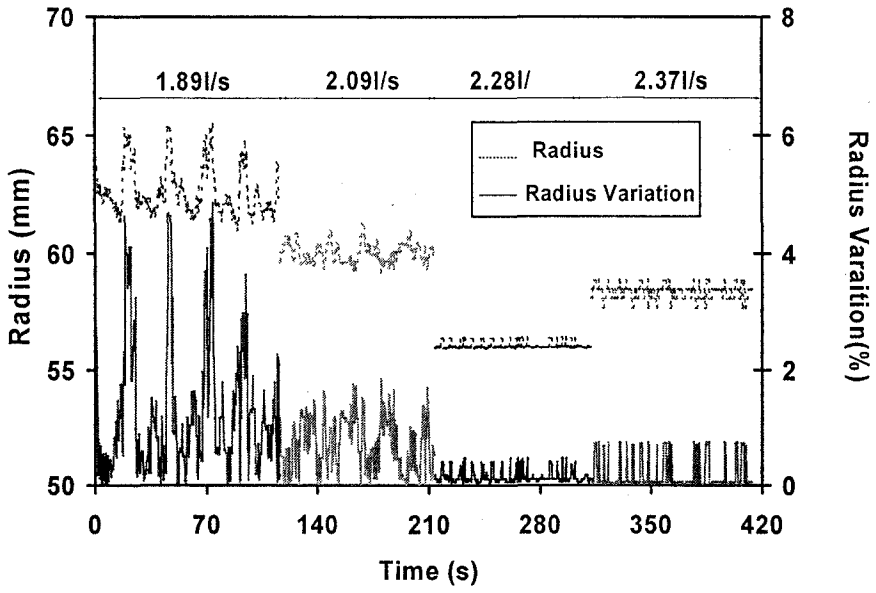

Fig. 4 Radius and radius variation response at different air flow rate (BUR=1.75, TUR=30)

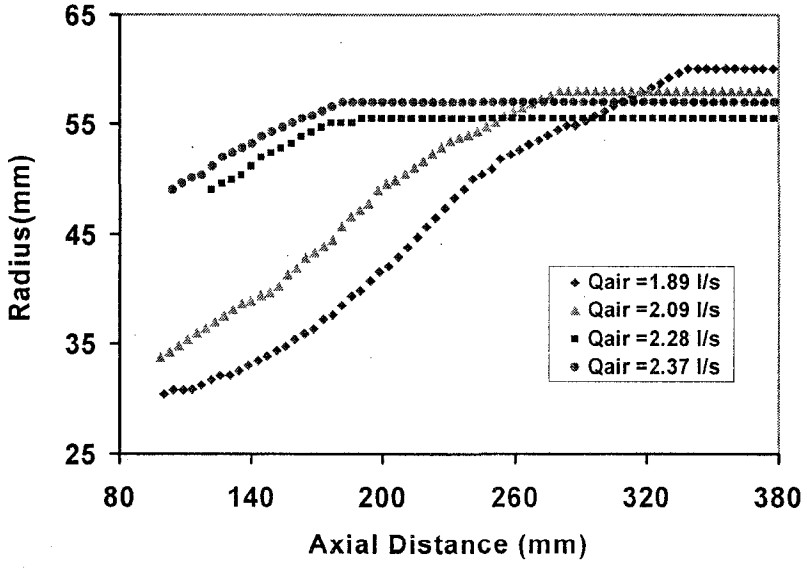

Fig.5 Bubble shape at different air flow rate (BUR=1.75, TUR=30)

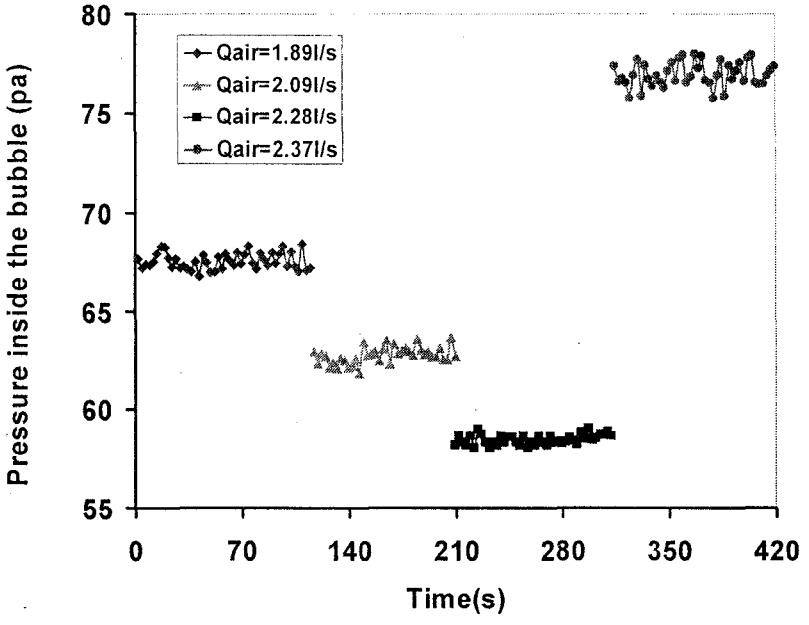

Fig.6 Pressure profile inside the bubble (BUR=1.75, TUR=30)

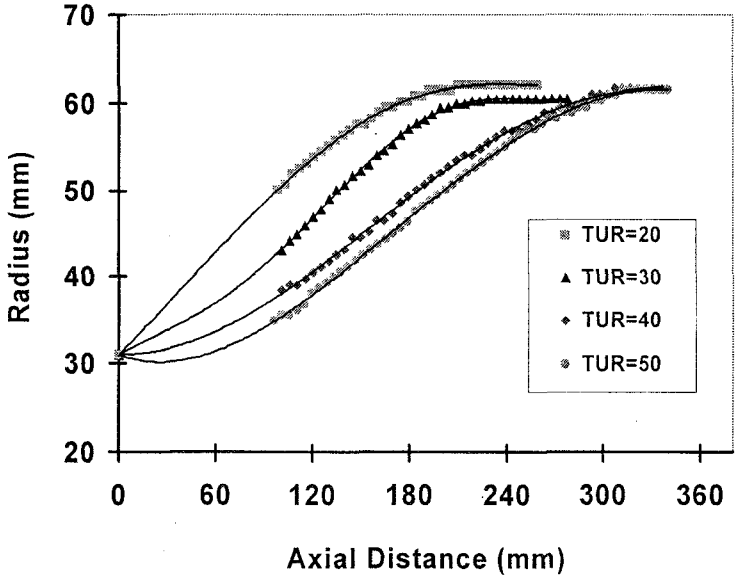

Fig.7 Bubble shape at instability critical point (BUR=2)

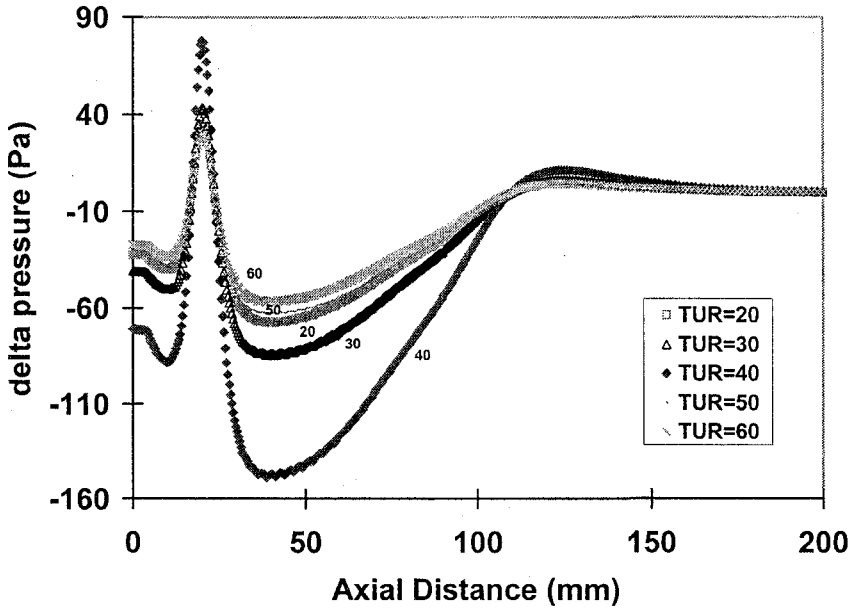

Fig.8 Delta pressure profiles around bubble surface at different TUR (BUR=1)

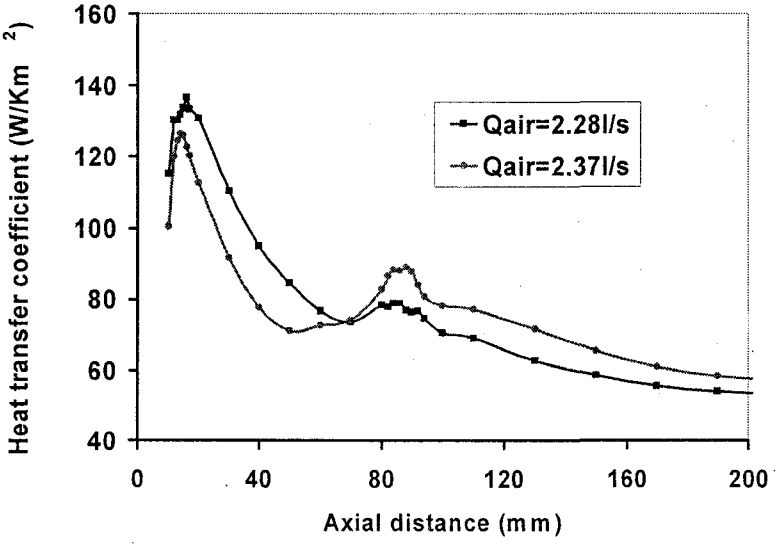

Fig. 9 Heat transfer coefficient at different air cooling rate used

APPENDIX F: Derivation of *RNG k-ε* Turbulence model

The governing equations of fluid dynamics represent the conservation of mass, momentum and energy for a fluid, which are now known as the Navier-Stokes equation. It is applied for a Newtonian and incompressible ideal gas as following:

These are the conservation of mass:

$$\frac{\partial \rho}{\partial t} + \frac{\partial \rho U_i}{\partial x_i} = 0 \qquad \text{(F. 1)}$$

The conservation of momentum:

$$\frac{\partial \rho U_i}{\partial t} + \frac{\partial}{\partial x_i}\left(\rho U_i U_j\right) = -\frac{\partial P}{\partial x_i} + \frac{\partial}{\partial x_j}\left(\mu\left(\frac{\partial U_i}{\partial x_j} + \frac{\partial U_j}{\partial x_i}\right) - \left(\frac{2}{3}\mu\frac{\partial U_k}{\partial x_k}\right)\right) + g_i\rho \qquad \text{(F.2)}$$

The conservation of thermal energy:

$$\rho\hat{C}_p\frac{DT}{Dt} = k\nabla^2 T \qquad \text{(F.3)}$$

For a turbulence flow, Reynolds decomposition can be applied, where the instantaneous variables is decomposed into the sum of a mean and fluctuating component, the replacing U by $\overline{U_i} + U_i'$ and T by $\overline{T_i} + T_i'$:

$$\frac{\partial \rho \overline{U_i}}{\partial t} + \frac{\partial}{\partial x_i}\left(\rho \overline{U_i U_j}\right) = -\frac{\partial P}{\partial x_i} + \frac{\partial}{\partial x_j}\left(\mu\left(\frac{\partial \overline{U_i}}{\partial x_j} + \frac{\partial \overline{U_j}}{\partial x_i}\right) - \left(\frac{2}{3}\mu \frac{\partial \overline{U_k}}{\partial x_k}\right)\right) + g_i \rho + \frac{\partial}{\partial x_j}\left(-\rho \overline{U_i' U_j'}\right) \quad \text{(F.4)}$$

A similar equation exists for the energy conservation:

$$C_p \frac{D\rho \overline{T}}{Dt} = k\left(\frac{\partial^2 \overline{T}}{\partial x_i^2}\right) - \frac{\partial C_p \rho \overline{U_i' T'}}{\partial x_i} \quad \text{(F.5)}$$

The extra terms are produced by this substitution are:

- Reynolds stress = $\rho \overline{U_i' U_j'}$
- Turbulent energy flux = $\hat{C}_p \rho \overline{U_i' T} = \overline{q^{(t)}}$

$$\rho \overline{U_i U_j} = \rho \begin{vmatrix} \overline{U_1^2} & \overline{U_1 U_2} & \overline{U_1 U_3} \\ \overline{U_2 U_1} & \overline{U_2^2} & \overline{U_2 U_3} \\ \overline{U_3 U_1} & \overline{U_3 U_2} & \overline{U_3^2} \end{vmatrix} \quad \text{(F.6)}$$

By analogy with the Fourier law of heat conduction, one may write:

$$\overline{q_{x_i}^{(t)}} = -k^{(t)} \frac{d\overline{T}}{dx_i} \quad \text{(F.7)}$$

The quantity $k^{(t)}$ is called the "turbulent coefficient of thermal conductivity" or "eddy conductivity". Where this eddy diffusivity is related to the eddy viscosity by:

$$k^{(t)} = \frac{\mu_T}{\sigma_T} \tag{F.8}$$

The Reynolds stress tensor (F.6) is unknown, the derivation of it leads to the turbulent closure problem. Two-equation models are widely used to closure this problem. In the standard ***k-ε model:***

$$-\rho\overline{u_i' u_j'} = \mu_{tur}\frac{\partial \overline{u_i}}{\partial x_j} \tag{F.9}$$

The contribution of Reynolds stresses to the momentum balance is introduced through the concept of the 'effective' viscosity, which is the sum of the molecular and the turbulent (or eddy viscosity) viscosity.

$$\mu_{eff} = \mu + \mu_{tur} = \mu\left[1 + \sqrt{\frac{\rho C_\mu}{\mu\varepsilon}}\right]^2 \tag{F.10}$$

For high Re flows, $\mu_{tur} \succ\succ \mu$

$$\mu_{eff} = C_\mu \rho \frac{k^2}{\varepsilon} \tag{F.11}$$

The k-ε model calculates two variables; the **kinetic energy of turbulence** ($k = \overline{u_i' u_j'} / 2$) and the **dissipation rate** of k (denoted as $\varepsilon = \frac{\mu}{\rho} \overline{u_i' u_j'}$). Using the concept of the effective viscosity, the mean momentum equation becomes:

$$\rho \frac{\partial k}{\partial t} + \frac{\partial \rho k \overline{U_i}}{\partial x_i} = \frac{\partial}{\partial x_i} \left(\left(\mu + \frac{\mu_T}{\sigma_k} \right) \frac{\partial k}{\partial x_i} \right) + G + B - \rho \varepsilon \tag{F.12}$$

$$\rho \frac{\partial \varepsilon}{\partial t} + \frac{\partial \rho \varepsilon \overline{U_i}}{\partial x_i} = \frac{\partial}{\partial x_i} \left(\left(\mu + \frac{\mu_T}{\sigma_\varepsilon} \right) \frac{\partial \varepsilon}{\partial x_i} \right) + C_1 \frac{\varepsilon}{k} G + C_1 (1 - C_3) \frac{\varepsilon}{k} B - C_2 \rho \frac{\varepsilon^2}{k} \tag{F.13}$$

The term G describes the additional turbulent kinetic energy (shear generation), which arises through the interaction of the main flow with the turbulent field. It is the shear production defined as:

$$G = \mu_{eff} \frac{\partial \overline{U_i}}{\partial x_j} \left(\frac{\partial \overline{U_i}}{\partial x_j} + \frac{\partial \overline{U_j}}{\partial x_i} \right) \tag{F.14}$$

The term B contains the influence of temperature dependent buoyancy generation/destruction. It is given by:

$$B = \frac{\mu_{eff}}{\sigma_T} \beta g_i \frac{\partial T}{\partial x_i} \tag{F.15}$$

The constants C_i that appear in these equations are empirical coefficients. σ_k and σ_ε are the turbulent Prandtl / Schmidt numbers for k and ε, respectively.

The RNG k-ε model, based on renormalized group theory, improves the shortcoming of the standard k-ε turbulent model in transient flows where the equilibrium turbulence

hypothesis is violated. It has the same form as the standard model. The only changes are a modified term relating to the production of energy dissipation in the ε equation and a different set of model constants.

$$\rho\frac{\partial k}{\partial t}+\frac{\partial \rho k\overline{U_i}}{\partial x_i}=\frac{\partial}{\partial x_i}\left(\left(\mu+\frac{\mu_T}{\sigma_k}\right)\frac{\partial k}{\partial x_i}\right)+G+B-\rho\varepsilon \tag{F.16}$$

$$\rho\frac{\partial \varepsilon}{\partial t}+\frac{\partial \rho\varepsilon\overline{U_i}}{\partial x_i}=\frac{\partial}{\partial x_i}\left(\left(\mu+\frac{\mu_T}{\sigma_\varepsilon}\right)\frac{\partial \varepsilon}{\partial x_i}\right)+C_1\frac{\varepsilon}{k}G+C_1(1-C_3)\frac{\varepsilon}{k}B+C_{1RNG}\frac{1}{\rho k}G^2-C_2\rho\frac{\varepsilon^2}{k} \tag{F.17}$$

The new function C1RNG is given by the equations:

$$C_{1RNG}=\frac{\eta\left(1-\eta/\eta_0\right)}{\left(1+\beta\eta^3\right)} \tag{F.18}$$

And:

$$\eta=\frac{k}{\varepsilon}\sqrt{\frac{P}{\mu}} \tag{F.19}$$

APPENDIX G: C Programming for bubble surface temperature boundary condition used in UDF (User Defined Function of Fluent)

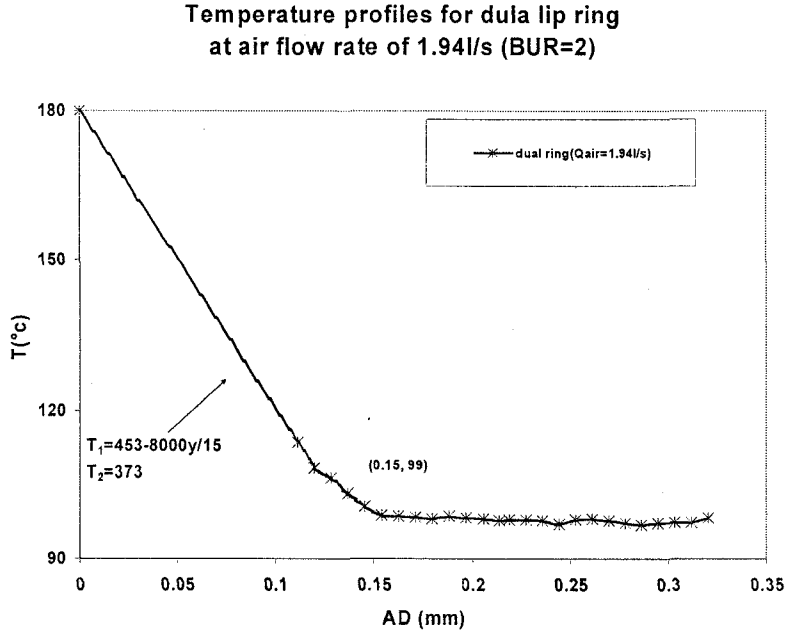


```
/************************************************************************
***
    UDF for computing and printing various parameters
************************************************************************
****/

#include "udf.h"

DEFINE_PROFILE(temp_prof_bubble, t, i)
{
 real x[ND_ND];
 real y;
```

```
 face_t f;

 begin_f_loop(f, t)
   {
    F_CENTROID(x,f,t);
    y = x[1];
    F_PROFILE(f, t, i) = 453-8000y/15; /* unit: K */
      if (N_ITER<2)
      {
            Message ("x and y positions of bubble face centroids: \t%f \t%f\n", x[0],
x[1]);
      }

   }
 end_f_loop(f, t)
}
```

APPENDIX H: Experiment setting to measure the air velocities

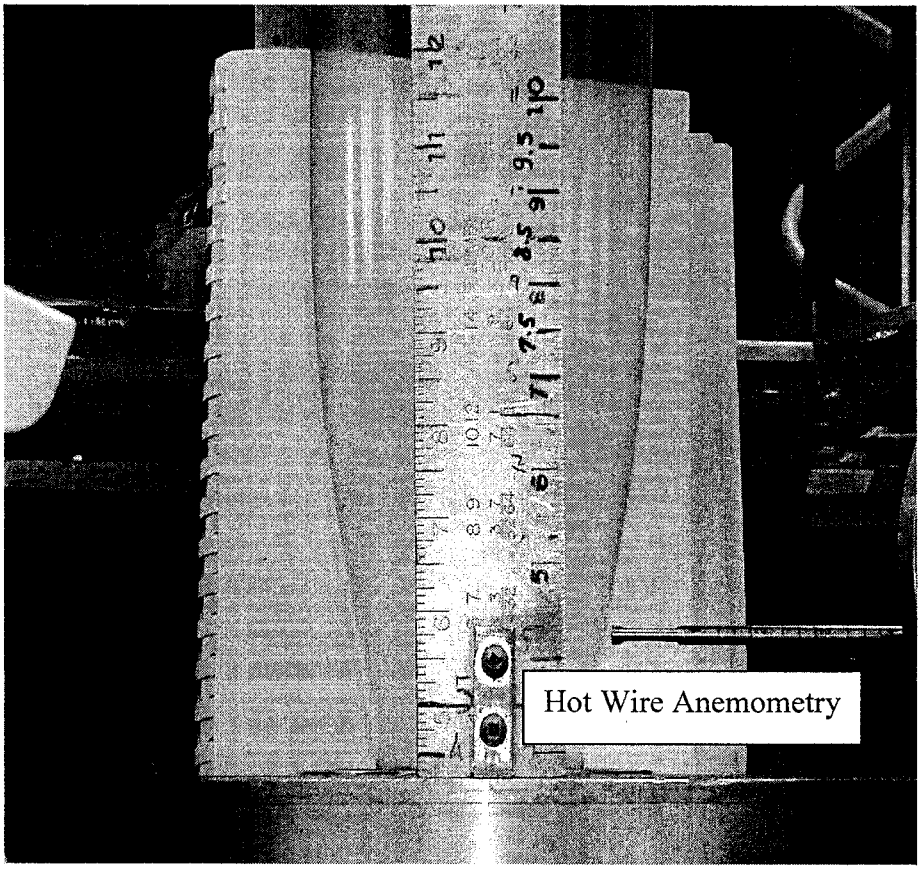

This photo shows the measurement of air velocity around the bubble surface. Hot-Wire Anemometer (HWA) is installed on the scaled frame that moves horizontally and indicates the distance from the bubble surface to the probe of the HWA. When the frame is fixed on a position, a series of air velocities of this point are captured by the HWA, the average value of them is considered as the measurement result. The air velocity at the different height from the die can be measured by adjusting the vertical position of the frame.

APPENDIX I: Some results in the work

Tables present the preset bubble kinematics in the simulation. (Take the dual lip air ring as an example.) The bubble radius, average temperature, static pressure around the bubble surface is listed at various axial distances from the die.

Table1 Bubble kinematics for BUR of 1 bubble

Node number	Axial distance (mm)	Radius (mm)	Temperature (K)	Pressure (Pa)
1	0.0000	32	420.23	-36.42
2	0.3333	32	452.87	-36.43
3	0.6667	32	452.73	-36.44
4	1.0000	32	452.60	-36.46
5	1.3333	32	452.47	-36.49
6	1.6667	32	452.33	-36.51
7	2.0000	32	452.20	-36.53
8	2.3333	32	452.07	-36.55
9	2.6667	32	451.93	-36.57
10	3.0000	32	451.80	-36.61
11	3.3333	32	451.67	-36.66
12	3.6667	32	451.53	-36.69
13	4.0000	32	451.40	-36.72
14	4.3333	32	451.27	-37.28
15	4.6667	32	451.13	-37.96
16	5.0000	32	451.00	-38.47
17	5.3333	32	450.87	-39.22
18	5.6667	32	450.73	-40.03
19	6.0000	32	450.60	-40.78
20	6.3333	32	450.47	-41.61
21	6.6667	32	450.33	-42.23
22	7.0000	32	450.20	-42.61
23	7.3333	32	450.07	-43.09
24	7.6667	32	449.93	-43.65
25	8.0000	32	449.80	-44.24
26	8.3333	32	449.67	-44.75
27	8.6667	32	449.53	-44.90
28	9.0000	32	449.40	-44.90
29	9.3333	32	449.27	-45.09
30	9.6667	32	449.13	-45.18
31	10.0000	32	449.00	-45.16
32	10.3333	32	448.87	-44.78
33	10.6667	32	448.73	-44.15
34	11.0000	32	448.60	-43.50
35	11.3333	32	448.47	-42.66
36	11.6667	32	448.33	-41.24
37	12.0000	32	448.20	-39.41

38	12.3333	32	448.07	-37.52
39	12.6667	32	447.93	-35.16
40	13.0000	32	447.80	-32.10
41	13.3333	32	447.67	-28.28
42	13.6667	32	447.53	-24.06
43	14.0000	32	447.40	-19.73
44	14.3333	32	447.27	-14.79
45	14.6667	32	447.13	-9.29
46	15.0000	32	447.00	-3.38
47	15.3333	32	446.87	2.26
48	15.6667	32	446.73	7.10
49	16.0000	32	446.60	12.04
50	16.3333	32	446.47	16.67
51	16.6667	32	446.33	20.37
52	17.0000	32	446.20	23.39
53	17.3333	32	446.07	25.99
54	17.6667	32	445.93	27.81
55	18.0000	32	445.80	28.46
56	18.3333	32	445.67	28.24
57	18.6667	32	445.53	26.86
58	19.0000	32	445.40	25.12
59	19.3333	32	445.27	23.38
60	19.6667	32	445.13	20.93
61	20.0000	32	445.00	17.91
62	20.3333	32	444.87	14.49
63	20.6667	32	444.73	10.33
64	21.0000	32	444.60	5.96
65	21.3333	32	444.47	2.16
66	21.6667	32	444.33	-1.64
67	22.0000	32	444.20	-5.52
68	22.3333	32	444.07	-9.33
69	22.6667	32	443.93	-13.76
70	23.0000	32	443.80	-18.06
71	23.3333	32	443.67	-21.26
72	23.6667	32	443.53	-24.25
73	24.0000	32	443.40	-27.23
74	24.3333	32	443.27	-30.00
75	24.6667	32	443.13	-32.83
76	25.0000	32	443.00	-36.49
77	25.3333	32	442.87	-39.74
78	25.6667	32	442.73	-41.19
79	26.0000	32	442.60	-42.44
80	26.3333	32	442.47	-44.12
81	26.6667	32	442.33	-45.70
82	27.0000	32	442.20	-47.17
83	27.3333	32	442.07	-48.77
84	27.6667	32	441.93	-51.41
85	28.0000	32	441.80	-53.33
86	28.3333	32	441.67	-53.23
87	28.6667	32	441.53	-53.24

88	29.0000	32	441.40	-53.86
89	29.3333	32	441.27	-54.55
90	29.6667	32	441.13	-55.21
91	30.0000	32	441.00	-55.84
92	30.3333	32	440.87	-56.73
93	30.6667	32	440.73	-58.80
94	31.0000	32	440.60	-59.93
95	31.3333	32	440.47	-58.88
96	31.6667	32	440.33	-58.15
97	32.0000	32	440.20	-58.18
98	32.3333	32	440.07	-58.41
99	32.6667	32	439.93	-58.69
100	33.0000	32	439.80	-59.01
101	33.3333	32	439.67	-59.60
102	33.6667	32	439.53	-60.18
103	34.0000	32	439.40	-60.01
104	34.3333	32	439.27	-59.52
105	34.6667	32	439.13	-59.34
106	35.0000	32	439.00	-59.36
107	35.3333	32	438.87	-59.72
108	35.6667	32	438.73	-60.15
109	36.0000	32	438.60	-59.82
110	36.3333	32	438.47	-59.19
111	36.6667	32	438.33	-58.92
112	37.0000	32	438.20	-58.84
113	37.3333	32	438.07	-59.12
114	37.6667	32	437.93	-59.44
115	38.0000	32	437.80	-58.98
116	38.3333	32	437.67	-58.25
117	38.6667	32	437.53	-57.92
118	39.0000	32	437.40	-57.76
119	39.3333	32	437.27	-57.80
120	39.6667	32	437.13	-58.30
121	40.0000	32	437.00	-58.73
122	40.3333	32	436.87	-58.13
123	40.6667	32	436.73	-57.07
124	41.0000	32	436.60	-56.47
125	41.3333	32	436.47	-56.19
126	41.6667	32	436.33	-56.20
127	42.0000	32	436.20	-56.67
128	42.3333	32	436.07	-57.06
129	42.6667	32	435.93	-56.38
130	43.0000	32	435.80	-55.24
131	43.3333	32	435.67	-54.58
132	43.6667	32	435.53	-54.28
133	44.0000	32	435.40	-54.26
134	44.3333	32	435.27	-54.71
135	44.6667	32	435.13	-55.07
136	45.0000	32	435.00	-54.34
137	45.3333	32	434.87	-53.16

138	45.6667	32	434.73	-52.47
139	46.0000	32	434.60	-52.14
140	46.3333	32	434.47	-52.09
141	46.6667	32	434.33	-52.51
142	47.0000	32	434.20	-52.83
143	47.3333	32	434.07	-52.07
144	47.6667	32	433.93	-50.87
145	48.0000	32	433.80	-50.16
146	48.3333	32	433.67	-49.80
147	48.6667	32	433.53	-49.75
148	49.0000	32	433.40	-50.15
149	49.3333	32	433.27	-50.44
150	49.6667	32	433.13	-49.66
151	50.0000	32	433.00	-48.46
152	50.3333	32	432.87	-47.75
153	50.6667	32	432.73	-47.39
154	51.0000	32	432.60	-47.33
155	51.3333	32	432.47	-47.71
156	51.6667	32	432.33	-47.98
157	52.0000	32	432.20	-47.19
158	52.3333	32	432.07	-45.99
159	52.6667	32	431.93	-45.24
160	53.0000	32	431.80	-44.80
161	53.3333	32	431.67	-44.52
162	53.6667	32	431.53	-44.46
163	54.0000	32	431.40	-44.81
164	54.3333	32	431.27	-45.05
165	54.6667	32	431.13	-44.26
166	55.0000	32	431.00	-43.08
167	55.3333	32	430.87	-42.35
168	55.6667	32	430.73	-41.92
169	56.0000	32	430.60	-41.65
170	56.3333	32	430.47	-41.57
171	56.6667	32	430.33	-41.92
172	57.0000	32	430.20	-42.14
173	57.3333	32	430.07	-41.33
174	57.6667	32	429.93	-40.16
175	58.0000	32	429.80	-39.42
176	58.3333	32	429.67	-38.95
177	58.6667	32	429.53	-38.60
178	59.0000	32	429.40	-38.34
179	59.3333	32	429.27	-38.25
180	59.6667	32	429.13	-38.57
181	60.0000	32	429.00	-38.77
182	60.3333	32	428.87	-37.98
183	60.6667	32	428.73	-36.83
184	61.0000	32	428.60	-36.11
185	61.3333	32	428.47	-35.65
186	61.6667	32	428.33	-35.31
187	62.0000	32	428.20	-35.03

188	62.3333	32	428.07	-34.82
189	62.6667	32	427.93	-34.73
190	63.0000	32	427.80	-34.70
191	63.3333	32	427.67	-34.44
192	63.6667	32	427.53	-33.89
193	64.0000	32	427.40	-33.30
194	64.3333	32	427.27	-32.83
195	64.6667	32	427.13	-32.48
196	65.0000	32	427.00	-32.27
197	65.3333	32	426.87	-32.12
198	65.6667	32	426.73	-31.78
199	66.0000	32	426.60	-31.20
200	66.3333	32	426.47	-30.66
201	66.6667	32	426.33	-30.27
202	67.0000	32	426.20	-29.99
203	67.3333	32	426.07	-29.85
204	67.6667	32	425.93	-29.76
205	68.0000	32	425.80	-29.48
206	68.3333	32	425.67	-28.95
207	68.6667	32	425.53	-28.40
208	69.0000	32	425.40	-27.97
209	69.3333	32	425.27	-27.65
210	69.6667	32	425.13	-27.47
211	70.0000	32	425.00	-27.34
212	70.3333	32	424.87	-27.05
213	70.6667	32	424.73	-26.55
214	71.0000	32	424.60	-26.06
215	71.3333	32	424.47	-25.69
216	71.6667	32	424.33	-25.35
217	72.0000	32	424.20	-25.06
218	72.3333	32	424.07	-24.87
219	72.6667	32	423.93	-24.74
220	73.0000	32	423.80	-24.43
221	73.3333	32	423.67	-23.93
222	73.6667	32	423.53	-23.45
223	74.0000	32	423.40	-23.08
224	74.3333	32	423.27	-22.78
225	74.6667	32	423.13	-22.52
226	75.0000	32	423.00	-22.31
227	75.3333	32	422.87	-22.17
228	75.6667	32	422.73	-22.06
229	76.0000	32	422.60	-21.87
230	76.3333	32	422.47	-21.49
231	76.6667	32	422.33	-21.02
232	77.0000	32	422.20	-20.58
233	77.3333	32	422.07	-20.25
234	77.6667	32	421.93	-20.06
235	78.0000	32	421.80	-19.96
236	78.3333	32	421.67	-19.82
237	78.6667	32	421.53	-19.54

238	79.0000	32	421.40	-19.15
239	79.3333	32	421.27	-18.79
240	79.6667	32	421.13	-18.53
241	80.0000	32	421.00	-18.38
242	80.3333	32	420.87	-18.28
243	80.6667	32	420.73	-18.12
244	81.0000	32	420.60	-17.79
245	81.3333	32	420.47	-17.36
246	81.6667	32	420.33	-16.96
247	82.0000	32	420.20	-16.63
248	82.3333	32	420.07	-16.37
249	82.6667	32	419.93	-16.16
250	83.0000	32	419.80	-16.02
251	83.3333	32	419.67	-15.90
252	83.6667	32	419.53	-15.77
253	84.0000	32	419.40	-15.56
254	84.3333	32	419.27	-15.31
255	84.6667	32	419.13	-15.06
256	85.0000	32	419.00	-14.79
257	85.3333	32	418.87	-14.51
258	85.6667	32	418.73	-14.25
259	86.0000	32	418.60	-14.02
260	86.3333	32	418.47	-13.83
261	86.6667	32	418.33	-13.67
262	87.0000	32	418.20	-13.51
263	87.3333	32	418.07	-13.30
264	87.6667	32	417.93	-13.03
265	88.0000	32	417.80	-12.75
266	88.3333	32	417.67	-12.49
267	88.6667	32	417.53	-12.26
268	89.0000	32	417.40	-12.05
269	89.3333	32	417.27	-11.87
270	89.6667	32	417.13	-11.73
271	90.0000	32	417.00	-11.62
272	90.3333	32	416.87	-11.53
273	90.6667	32	416.73	-11.40
274	91.0000	32	416.60	-11.20
275	91.3333	32	416.47	-10.95
276	91.6667	32	416.33	-10.71
277	92.0000	32	416.20	-10.45
278	92.3333	32	416.07	-10.18
279	92.6667	32	415.93	-9.93
280	93.0000	32	415.80	-9.71
281	93.3333	32	415.67	-9.53
282	93.6667	32	415.53	-9.40
283	94.0000	32	415.40	-9.33
284	94.3333	32	415.27	-9.27
285	94.6667	32	415.13	-9.06
286	95.0000	32	415.00	-8.75
287	95.3333	32	414.87	-8.53

288	95.6667	32	414.73	-8.51
289	96.0000	32	414.60	-8.74
290	96.3333	32	414.47	-9.41
291	96.6667	32	414.33	-8.76
292	97.0000	32	414.20	-7.24
293	97.3333	32	414.07	-6.64
294	97.6667	32	413.93	-6.40
295	98.0000	32	413.80	-6.83
296	98.3333	32	413.67	-6.64
297	98.6667	32	413.53	-5.89
298	99.0000	32	413.40	-6.15
299	99.3333	32	413.27	-7.16
300	99.6667	32	413.13	-6.41
301	100.0000	32	412.93	-4.91
302	101.0000	32	412.60	-4.74
303	102.0000	32	412.20	-4.33
304	103.0000	32	411.80	-3.80
305	104.0000	32	411.40	-3.43
306	105.0000	32	411.00	-2.87
307	106.0000	32	410.60	-2.39
308	107.0000	32	410.20	-2.14
309	108.0000	32	409.80	-1.81
310	109.0000	32	409.40	-1.49
311	110.0000	32	409.00	-1.18
312	111.0000	32	408.60	-0.89
313	112.0000	32	408.20	-0.62
314	113.0000	32	407.80	-0.37
315	114.0000	32	407.40	-0.14
316	115.0000	32	407.00	0.08
317	116.0000	32	406.60	0.28
318	117.0000	32	406.20	0.46
319	118.0000	32	405.80	0.62
320	119.0000	32	405.40	0.78
321	120.0000	32	405.00	0.91
322	121.0000	32	404.60	1.03
323	122.0000	32	404.20	1.14
324	123.0000	32	403.80	1.24
325	124.0000	32	403.40	1.32
326	125.0000	32	403.00	1.40
327	126.0000	32	402.60	1.46
328	127.0000	32	402.20	1.51
329	128.0000	32	401.80	1.56
330	129.0000	32	401.40	1.60
331	130.0000	32	401.00	1.63
332	131.0000	32	400.60	1.65
333	132.0000	32	400.20	1.67
334	133.0000	32	399.80	1.68
335	134.0000	32	399.40	1.69
336	135.0000	32	399.00	1.69
337	136.0000	32	398.60	1.69

338	137.0000	32	398.20	1.68
339	138.0000	32	397.80	1.67
340	139.0000	32	397.40	1.66
341	140.0000	32	397.00	1.65
342	141.0000	32	396.60	1.63
343	142.0000	32	396.20	1.61
344	143.0000	32	395.80	1.59
345	144.0000	32	395.40	1.57
346	145.0000	32	395.00	1.54
347	146.0000	32	394.60	1.52
348	147.0000	32	394.20	1.49
349	148.0000	32	393.80	1.46
350	149.0000	32	393.40	1.44
351	150.0000	32	393.00	1.41
352	151.0000	32	392.60	1.38
353	152.0000	32	392.20	1.35
354	153.0000	32	391.80	1.32
355	154.0000	32	391.40	1.30
356	155.0000	32	391.00	1.27
357	156.0000	32	390.60	1.24
358	157.0000	32	390.20	1.21
359	158.0000	32	389.80	1.18
360	159.0000	32	389.40	1.16
361	160.0000	32	389.00	1.13
362	161.0000	32	388.60	1.10
363	162.0000	32	388.20	1.08
364	163.0000	32	387.80	1.05
365	164.0000	32	387.40	1.03
366	165.0000	32	387.00	1.00
367	166.0000	32	386.60	0.98
368	167.0000	32	386.20	0.96
369	168.0000	32	385.80	0.93
370	169.0000	32	385.40	0.91
371	170.0000	32	385.00	0.89
372	171.0000	32	384.60	0.87
373	172.0000	32	384.20	0.85
374	173.0000	32	383.80	0.83
375	174.0000	32	383.40	0.81
376	175.0000	32	383.00	0.80
377	176.0000	32	382.60	0.78
378	177.0000	32	382.20	0.76
379	178.0000	32	381.80	0.74
380	179.0000	32	381.40	0.73
381	180.0000	32	381.00	0.71
382	181.0000	32	380.60	0.70
383	182.0000	32	380.20	0.69
384	183.0000	32	379.80	0.67
385	184.0000	32	379.40	0.66
386	185.0000	32	379.00	0.65
387	186.0000	32	378.60	0.63

388	187.0000	32	378.20	0.62
389	188.0000	32	377.80	0.61
390	189.0000	32	377.40	0.60
391	190.0000	32	377.00	0.59
392	191.0000	32	376.60	0.58
393	192.0000	32	376.20	0.57
394	193.0000	32	375.80	0.56
395	194.0000	32	375.40	0.56
396	195.0000	32	375.00	0.55
397	196.0000	32	374.60	0.54
398	197.0000	32	374.20	0.53
399	198.0000	32	373.80	0.52
400	199.0000	32	373.40	0.52
401	200.0000	32	373.10	0.51
402	200.0000	32	373.10	0.51
403	201.0000	32	373.00	0.50
404	202.0000	32	373.00	0.50
405	203.0000	32	373.00	0.49
406	204.0000	32	373.00	0.49
407	205.0000	32	373.00	0.48
408	206.0000	32	373.00	0.47
409	207.0000	32	373.00	0.47
410	208.0000	32	373.00	0.46
411	209.0000	32	373.00	0.46
412	210.0000	32	373.00	0.45
413	211.0000	32	373.00	0.45
414	212.0000	32	373.00	0.44
415	213.0000	32	373.00	0.44
416	214.0000	32	373.00	0.43
417	215.0000	32	373.00	0.43
418	216.0000	32	373.00	0.42
419	217.0000	32	373.00	0.42
420	218.0000	32	373.00	0.41
421	219.0000	32	373.00	0.41
422	220.0000	32	373.00	0.40
423	221.0000	32	373.00	0.40
424	222.0000	32	373.00	0.39
425	223.0000	32	373.00	0.39
426	224.0000	32	373.00	0.38
427	225.0000	32	373.00	0.38
428	226.0000	32	373.00	0.37
429	227.0000	32	373.00	0.36
430	228.0000	32	373.00	0.36
431	229.0000	32	373.00	0.35
432	230.0000	32	373.00	0.34
433	231.0000	32	373.00	0.34
434	232.0000	32	373.00	0.33
435	233.0000	32	373.00	0.32
436	234.0000	32	373.00	0.31
437	235.0000	32	373.00	0.31

438	236.0000	32	373.00	0.30
439	237.0000	32	373.00	0.29
440	238.0000	32	373.00	0.28
441	239.0000	32	373.00	0.27
442	240.0000	32	373.00	0.26
443	241.0000	32	373.00	0.25
444	242.0000	32	373.00	0.24
445	243.0000	32	373.00	0.23
446	244.0000	32	373.00	0.22
447	245.0000	32	373.00	0.21
448	246.0000	32	373.00	0.20
449	247.0000	32	373.00	0.19
450	248.0000	32	373.00	0.18
451	249.0000	32	373.00	0.17
452	250.0000	32	373.00	0.16
453	251.0000	32	373.00	0.15
454	252.0000	32	373.00	0.14
455	253.0000	32	373.00	0.13
456	254.0000	32	373.00	0.11
457	255.0000	32	373.00	0.10
458	256.0000	32	373.00	0.09
459	257.0000	32	373.00	0.08
460	258.0000	32	373.00	0.07
461	259.0000	32	373.00	0.06
462	260.0000	32	373.00	0.05
463	261.0000	32	373.00	0.03
464	262.0000	32	373.00	0.02
465	263.0000	32	373.00	0.01
466	264.0000	32	373.00	0.00
467	265.0000	32	373.00	-0.01
468	266.0000	32	373.00	-0.02
469	267.0000	32	373.00	-0.03
470	268.0000	32	373.00	-0.05
471	269.0000	32	373.00	-0.06
472	270.0000	32	373.00	-0.07
473	271.0000	32	373.00	-0.08
474	272.0000	32	373.00	-0.09
475	273.0000	32	373.00	-0.10
476	274.0000	32	373.00	-0.11
477	275.0000	32	373.00	-0.12
478	276.0000	32	373.00	-0.13
479	277.0000	32	373.00	-0.14
480	278.0000	32	373.00	-0.16
481	279.0000	32	373.00	-0.17
482	280.0000	32	373.00	-0.19
483	281.0000	32	373.00	-0.20
484	282.0000	32	373.00	-0.21
485	283.0000	32	373.00	-0.23
486	284.0000	32	373.00	-0.24
487	285.0000	32	373.00	-0.26

488	286.0000	32	373.00	-0.27
489	287.0000	32	373.00	-0.28
490	288.0000	32	373.00	-0.29
491	289.0000	32	373.00	-0.30
492	290.0000	32	373.00	-0.31
493	291.0000	32	373.00	-0.33
494	292.0000	32	373.00	-0.35
495	293.0000	32	373.00	-0.38
496	294.0000	32	373.00	-0.44
497	295.0000	32	373.00	-0.67
498	296.0000	32	373.00	-0.73
499	297.0000	32	373.00	-0.56
500	298.0000	32	373.00	-0.62

Table2 Bubble kinematics for BUR of 3 bubble

Node number	Axial distance (mm)	Radius (mm)	Temperature (K)	Pressure (Pa)
1	0.0000	32.0000	416.69	-46.50
2	0.3333	32.0000	452.87	-46.51
3	0.6667	32.0000	452.73	-46.54
4	1.0000	32.0000	452.60	-46.58
5	1.3333	32.0000	452.47	-46.64
6	1.6667	32.0000	452.33	-46.70
7	2.0000	32.0000	452.20	-46.74
8	2.3333	32.0000	452.07	-46.78
9	2.6667	32.0000	451.93	-46.82
10	3.0000	32.0000	451.80	-46.89
11	3.3333	32.0000	451.67	-46.99
12	3.6667	32.0000	451.53	-47.07
13	4.0000	32.0000	451.40	-47.12
14	4.3333	32.0000	451.27	-48.14
15	4.6667	32.0000	451.13	-49.41
16	5.0000	32.0000	451.00	-50.42
17	5.3333	32.0000	450.87	-51.92
18	5.6667	32.0000	450.73	-53.47
19	6.0000	32.0000	450.60	-54.92
20	6.3333	32.0000	450.47	-56.22
21	6.6667	32.0000	450.33	-57.29
22	7.0000	32.0000	450.20	-58.26
23	7.3333	32.0000	450.07	-59.29
24	7.6667	32.0000	449.93	-60.33
25	8.0000	32.0000	449.80	-61.34
26	8.3333	32.0000	449.67	-62.27
27	8.6667	32.0000	449.53	-63.14
28	9.0000	32.0000	449.40	-63.82
29	9.3333	32.0000	449.27	-64.46
30	9.6667	32.0000	449.13	-65.18
31	10.0000	32.0000	449.00	-65.72

32	10.3333	32.0000	448.87	-66.11
33	10.6667	32.0000	448.73	-66.36
34	11.0000	32.0000	448.60	-66.30
35	11.3333	32.0000	448.47	-65.71
36	11.6667	32.0000	448.33	-64.64
37	12.0000	32.0000	448.20	-63.01
38	12.3333	32.0000	448.07	-60.60
39	12.6667	32.0000	447.93	-57.43
40	13.0000	32.0000	447.80	-53.19
41	13.3333	32.0000	447.67	-47.62
42	13.6667	32.0000	447.53	-40.83
43	14.0000	32.0000	447.40	-33.24
44	14.3333	32.0000	447.27	-25.03
45	14.6667	32.0000	447.13	-16.24
46	15.0000	32.0000	447.00	-7.08
47	15.3333	32.0000	446.87	2.26
48	15.6667	32.0000	446.73	11.28
49	16.0000	32.0000	446.60	19.66
50	16.3333	32.0000	446.47	27.13
51	16.6667	32.0000	446.33	33.95
52	17.0000	32.0000	446.20	39.78
53	17.3333	32.0000	446.07	43.92
54	17.6667	32.0000	445.93	46.69
55	18.0000	32.0000	445.80	47.90
56	18.3333	32.0000	445.67	47.64
57	18.6667	32.0000	445.53	46.29
58	19.0000	32.0000	445.40	43.85
59	19.3333	32.0000	445.27	40.51
60	19.6667	32.0000	445.13	36.39
61	20.0000	32.0000	445.00	31.68
62	20.3333	32.0000	444.87	26.58
63	20.6667	32.0000	444.73	21.32
64	21.0000	32.0000	444.60	15.98
65	21.3333	32.0000	444.47	10.58
66	21.6667	32.0000	444.33	5.17
67	22.0000	32.0000	444.20	-0.13
68	22.3333	32.0000	444.07	-5.27
69	22.6667	32.0000	443.93	-10.20
70	23.0000	32.0000	443.80	-14.85
71	23.3333	32.0000	443.67	-19.18
72	23.6667	32.0000	443.53	-23.23
73	24.0000	32.0000	443.40	-27.06
74	24.3333	32.0000	443.27	-30.63
75	24.6667	32.0000	443.13	-33.87
76	25.0000	32.0000	443.00	-36.79
77	25.3333	32.0000	442.87	-39.47
78	25.6667	32.0000	442.73	-41.96
79	26.0000	32.0000	442.60	-44.29
80	26.3333	32.0000	442.47	-46.39
81	26.6667	32.0000	442.33	-48.20

82	27.0000	32.0000	442.20	-49.75
83	27.3333	32.0000	442.07	-51.16
84	27.6667	32.0000	441.93	-52.51
85	28.0000	32.0000	441.80	-53.79
86	28.3333	32.0000	441.67	-54.91
87	28.6667	32.0000	441.53	-55.77
88	29.0000	32.0000	441.40	-56.44
89	29.3333	32.0000	441.27	-57.05
90	29.6667	32.0000	441.13	-57.67
91	30.0000	32.0000	441.00	-58.30
92	30.3333	32.0000	440.87	-58.85
93	30.6667	32.0000	440.73	-59.23
94	31.0000	32.0000	440.60	-59.48
95	31.3333	32.0000	440.47	-59.73
96	31.6667	32.0000	440.33	-60.04
97	32.0000	32.0000	440.20	-60.37
98	32.3333	32.0000	440.07	-60.61
99	32.6667	32.0000	439.93	-60.65
100	33.0000	32.0000	439.80	-60.58
101	33.3333	32.0000	439.67	-60.54
102	33.6667	32.0000	439.53	-60.59
103	34.0000	32.0000	439.40	-60.69
104	34.3333	32.0000	439.27	-60.74
105	34.6667	32.0000	439.13	-60.63
106	35.0000	32.0000	439.00	-60.43
107	35.3333	32.0000	438.87	-60.27
108	35.6667	32.0000	438.73	-60.19
109	36.0000	32.0000	438.60	-60.20
110	36.3333	32.0000	438.47	-60.23
111	36.6667	32.0000	438.33	-60.17
112	37.0000	32.0000	438.20	-59.93
113	37.3333	32.0000	438.07	-59.58
114	37.6667	32.0000	437.93	-59.27
115	38.0000	32.0000	437.80	-59.08
116	38.3333	32.0000	437.67	-58.98
117	38.6667	32.0000	437.53	-58.92
118	39.0000	32.0000	437.40	-58.78
119	39.3333	32.0000	437.27	-58.46
120	39.6667	32.0000	437.13	-58.03
121	40.0000	32.0000	437.00	-57.68
122	40.3333	32.0000	436.87	-57.44
123	40.6667	32.0000	436.73	-57.29
124	41.0000	32.0000	436.60	-57.20
125	41.3333	32.0000	436.47	-57.01
126	41.6667	32.0000	436.33	-56.64
127	42.0000	32.0000	436.20	-56.15
128	42.3333	32.0000	436.07	-55.74
129	42.6667	32.0000	435.93	-55.45
130	43.0000	32.0000	435.80	-55.27
131	43.3333	32.0000	435.67	-55.13

132	43.6667	32.0000	435.53	-54.91
133	44.0000	32.0000	435.40	-54.48
134	44.3333	32.0000	435.27	-53.94
135	44.6667	32.0000	435.13	-53.47
136	45.0000	32.0000	435.00	-53.11
137	45.3333	32.0000	434.87	-52.86
138	45.6667	32.0000	434.73	-52.68
139	46.0000	32.0000	434.60	-52.53
140	46.3333	32.0000	434.47	-52.29
141	46.6667	32.0000	434.33	-51.83
142	47.0000	32.0000	434.20	-51.26
143	47.3333	32.0000	434.07	-50.76
144	47.6667	32.0000	433.93	-50.39
145	48.0000	32.0000	433.80	-50.13
146	48.3333	32.0000	433.67	-49.96
147	48.6667	32.0000	433.53	-49.86
148	49.0000	32.0000	433.40	-49.71
149	49.3333	32.0000	433.27	-49.41
150	49.6667	32.0000	433.13	-49.03
151	50.0000	32.0000	433.00	-48.65
152	50.3347	31.9963	432.87	-47.81
153	50.6694	31.9930	432.73	-46.81
154	51.0041	31.9901	432.60	-46.14
155	51.3388	31.9876	432.46	-45.50
156	51.6735	31.9855	432.33	-44.82
157	52.0083	31.9838	432.20	-44.11
158	52.3430	31.9824	432.06	-43.50
159	52.6777	31.9815	431.93	-42.95
160	53.0124	31.9809	431.80	-42.42
161	53.3471	31.9807	431.66	-41.88
162	53.6819	31.9810	431.53	-41.40
163	54.0166	31.9816	431.39	-40.99
164	54.3513	31.9826	431.26	-40.55
165	54.6860	31.9840	431.13	-39.98
166	55.0207	31.9857	430.99	-39.35
167	55.3554	31.9879	430.86	-38.80
168	55.6902	31.9905	430.72	-38.35
169	56.0249	31.9934	430.59	-37.99
170	56.3596	31.9968	430.46	-37.71
171	56.6943	32.0005	430.32	-37.47
172	57.0290	32.0046	430.19	-37.14
173	57.3637	32.0091	430.05	-36.63
174	57.6983	32.0140	429.92	-36.03
175	58.0330	32.0193	429.79	-35.49
176	58.3677	32.0250	429.65	-35.05
177	58.7024	32.0311	429.52	-34.72
178	59.0370	32.0375	429.39	-34.45
179	59.3717	32.0444	429.25	-34.22
180	59.7063	32.0516	429.12	-33.92
181	60.0409	32.0593	428.98	-33.45

182	60.3756	32.0673	428.85	-32.91
183	60.7102	32.0757	428.72	-32.42
184	61.0448	32.0845	428.58	-32.05
185	61.3794	32.0937	428.45	-31.77
186	61.7140	32.1033	428.31	-31.55
187	62.0485	32.1133	428.18	-31.27
188	62.3831	32.1236	428.05	-30.85
189	62.7177	32.1344	427.91	-30.34
190	63.0522	32.1455	427.78	-29.87
191	63.3867	32.1571	427.65	-29.48
192	63.7212	32.1690	427.51	-29.17
193	64.0557	32.1813	427.38	-28.90
194	64.3902	32.1940	427.24	-28.59
195	64.7247	32.2071	427.11	-28.18
196	65.0591	32.2206	426.98	-27.73
197	65.3935	32.2345	426.84	-27.33
198	65.7280	32.2487	426.71	-27.03
199	66.0132	32.2566	426.60	-26.89
200	66.4065	32.2715	426.48	-26.70
201	66.7201	32.2899	426.27	-26.59
202	67.0012	32.1450	426.15	-26.50
203	67.3998	32.3259	426.04	-26.41
204	67.7341	32.3425	425.91	-25.27
205	68.0684	32.3595	425.77	-24.59
206	68.4026	32.3769	425.64	-24.07
207	68.7369	32.3946	425.51	-23.59
208	69.0711	32.4128	425.37	-23.17
209	69.4053	32.4314	425.24	-22.82
210	69.7395	32.4503	425.10	-22.51
211	70.0737	32.4696	424.97	-22.23
212	70.4078	32.4893	424.84	-22.00
213	70.7419	32.5095	424.70	-21.84
214	71.0760	32.5299	424.57	-21.71
215	71.4101	32.5508	424.44	-21.50
216	71.7441	32.5721	424.30	-21.13
217	72.0782	32.5938	424.17	-20.66
218	72.4121	32.6158	424.04	-20.24
219	72.7461	32.6383	423.90	-19.94
220	73.0801	32.6611	423.77	-19.78
221	73.4140	32.6843	423.63	-19.66
222	73.7479	32.7080	423.50	-19.35
223	74.0817	32.7320	423.37	-18.79
224	74.4155	32.7564	423.23	-18.24
225	74.7494	32.7811	423.10	-17.79
226	75.0831	32.8063	422.97	-17.44
227	75.4169	32.8319	422.83	-17.14
228	75.7506	32.8578	422.70	-16.89
229	76.0843	32.8842	422.57	-16.73
230	76.4179	32.9109	422.43	-16.63
231	76.7515	32.9380	422.30	-16.38

232	77.0851	32.9655	422.17	-15.97
233	77.4187	32.9934	422.03	-15.59
234	77.7522	33.0217	421.90	-15.29
235	78.0857	33.0504	421.77	-14.98
236	78.4192	33.0794	421.63	-14.64
237	78.7526	33.1089	421.50	-14.31
238	79.0860	33.1387	421.37	-14.02
239	79.4193	33.1689	421.23	-13.80
240	79.7526	33.1995	421.10	-13.65
241	80.0859	33.2306	420.97	-13.56
242	80.4192	33.2619	420.83	-13.40
243	80.7524	33.2937	420.70	-13.09
244	81.0855	33.3259	420.57	-12.69
245	81.4187	33.3585	420.43	-12.31
246	81.7518	33.3914	420.30	-12.01
247	82.0848	33.4247	420.17	-11.78
248	82.4179	33.4585	420.03	-11.63
249	82.7508	33.4926	419.90	-11.64
250	83.0015	33.5205	419.79	-11.55
251	83.4199	33.5700	419.46	-11.41
252	83.8912	33.6015	419.30	-11.34
253	84.0823	33.6329	419.37	-10.21
254	84.4151	33.6689	419.23	-9.46
255	84.7478	33.7054	419.10	-9.11
256	85.0805	33.7422	418.97	-8.99
257	85.4132	33.7794	418.83	-8.86
258	85.7458	33.8170	418.70	-8.71
259	86.0783	33.8550	418.57	-8.54
260	86.4109	33.8934	418.44	-8.36
261	86.7433	33.9322	418.30	-8.18
262	87.0757	33.9713	418.17	-8.00
263	87.4081	34.0109	418.04	-7.84
264	87.7405	34.0508	417.90	-7.69
265	88.0727	34.0911	417.77	-7.55
266	88.4050	34.1318	417.64	-7.44
267	88.7372	34.1729	417.51	-7.32
268	89.0693	34.2144	417.37	-7.16
269	89.4014	34.2562	417.24	-6.95
270	89.7334	34.2985	417.11	-6.73
271	90.0654	34.3411	416.97	-6.53
272	90.3974	34.3842	416.84	-6.36
273	90.7293	34.4276	416.71	-6.21
274	91.0611	34.4714	416.58	-6.05
275	91.3929	34.5156	416.44	-5.88
276	91.7246	34.5601	416.31	-5.73
277	92.0563	34.6051	416.18	-5.54
278	92.3880	34.6504	416.04	-5.30
279	92.7195	34.6962	415.91	-5.04
280	93.0511	34.7423	415.78	-4.84
281	93.3826	34.7888	415.65	-4.71

282	93.7140	34.8357	415.51	-4.65
283	94.0453	34.8830	415.38	-4.62
284	94.3766	34.9306	415.25	-4.54
285	94.7079	34.9787	415.12	-4.41
286	95.0391	35.0271	414.98	-4.23
287	95.3702	35.0760	414.85	-3.93
288	95.7013	35.1252	414.72	-3.60
289	96.0323	35.1748	414.59	-3.50
290	96.3633	35.2247	414.45	-3.43
291	96.6942	35.2751	414.32	-3.08
292	97.0251	35.3259	414.19	-3.30
293	97.3559	35.3770	414.06	-2.85
294	97.7122	36.4122	413.89	-2.64
295	98.0013	36.4757	413.75	-2.53
296	98.3479	35.5327	413.66	-2.46
297	98.7166	35.5846	413.49	-2.40
298	99.0589	35.6100	413.36	-2.35
299	99.3278	35.6924	413.26	-2.31
300	99.6697	35.7458	413.13	-2.30
301	100.0000	35.8000	412.93	-0.95
302	101.0486	35.9688	412.58	0.08
303	102.0966	36.1412	412.16	0.64
304	103.1439	36.3172	411.74	0.51
305	104.1907	36.4969	411.32	0.98
306	105.2369	36.6800	410.91	1.75
307	106.2824	36.8668	410.49	2.20
308	107.3273	37.0572	410.07	2.27
309	108.3715	37.2512	409.65	2.69
310	109.4150	37.4487	409.23	3.11
311	110.4579	37.6498	408.82	3.41
312	111.5000	37.8545	408.40	3.59
313	112.5415	38.0628	407.98	3.87
314	113.5822	38.2747	407.57	4.13
315	114.6222	38.4901	407.15	4.34
316	115.6614	38.7091	406.74	4.53
317	116.6999	38.9316	406.32	4.69
318	117.7376	39.1577	405.91	4.83
319	118.7746	39.3874	405.49	4.95
320	119.8107	39.6207	405.08	5.06
321	120.8461	39.8574	404.66	5.15
322	121.8806	40.0978	404.25	5.23
323	122.9143	40.3417	403.83	5.29
324	123.9471	40.5891	403.42	5.34
325	124.9791	40.8401	403.01	5.38
326	126.0102	41.0946	402.60	5.41
327	127.0405	41.3527	402.18	5.43
328	128.0698	41.6143	401.77	5.44
329	129.0983	41.8794	401.36	5.44
330	130.1258	42.1481	400.95	5.44
331	131.1524	42.4203	400.54	5.43

332	132.1781	42.6960	400.13	5.41
333	133.2028	42.9752	399.72	5.39
334	134.2265	43.2579	399.31	5.36
335	135.2493	43.5442	398.90	5.33
336	136.2710	43.8339	398.49	5.30
337	137.2918	44.1272	398.08	5.26
338	138.3116	44.4240	397.68	5.22
339	139.3303	44.7242	397.27	5.18
340	140.3480	45.0280	396.86	5.14
341	141.3647	45.3352	396.45	5.09
342	142.3803	45.6460	396.05	5.04
343	143.3948	45.9602	395.64	4.99
344	144.4083	46.2779	395.24	4.94
345	145.4206	46.5991	394.83	4.89
346	146.4318	46.9237	394.43	4.84
347	147.4420	47.2519	394.02	4.78
348	148.4509	47.5834	393.62	4.73
349	149.4588	47.9185	393.22	4.67
350	150.4654	48.2570	392.81	4.61
351	151.4710	48.5990	392.41	4.55
352	152.4753	48.9444	392.01	4.50
353	153.4784	49.2932	391.61	4.44
354	154.4804	49.6455	391.21	4.38
355	155.4811	50.0012	390.81	4.33
356	156.4806	50.3604	390.41	4.28
357	157.4789	50.7230	390.01	4.22
358	158.4759	51.0890	389.61	4.17
359	159.4716	51.4585	389.21	4.11
360	160.4661	51.8313	388.81	4.05
361	161.4593	52.2076	388.42	4.00
362	162.4512	52.5872	388.02	3.94
363	163.4417	52.9703	387.62	3.88
364	164.4310	53.3568	387.23	3.83
365	165.4189	53.7467	386.83	3.77
366	166.4055	54.1399	386.44	3.71
367	167.3907	54.5365	386.04	3.65
368	168.3746	54.9366	385.65	3.59
369	169.3571	55.3400	385.26	3.53
370	170.3382	55.7467	384.86	3.47
371	171.3179	56.1568	384.47	3.41
372	172.2961	56.5703	384.08	3.35
373	173.2730	56.9872	383.69	3.28
374	174.2484	57.4074	383.30	3.22
375	175.2224	57.8309	382.91	3.15
376	176.1949	58.2578	382.52	3.08
377	177.1659	58.6880	382.13	3.02
378	178.1355	59.1215	381.75	2.95
379	179.1035	59.5584	381.36	2.88
380	180.0701	59.9986	380.97	2.80
381	181.0351	60.4421	380.59	2.73

382	181.9986	60.8889	380.20	2.65
383	182.9606	61.3390	379.82	2.57
384	183.9210	61.7924	379.43	2.49
385	184.8799	62.2492	379.05	2.40
386	185.8371	62.7092	378.67	2.31
387	186.7929	63.1724	378.28	2.22
388	187.7470	63.6390	377.90	2.11
389	188.6995	64.1088	377.52	2.01
390	189.6503	64.5819	377.14	1.89
391	190.5996	65.0583	376.76	1.77
392	191.5472	65.5379	376.38	1.65
393	192.4932	66.0208	376.00	1.51
394	193.4374	66.5069	375.63	1.36
395	194.3801	66.9962	375.25	1.20
396	195.3210	67.4888	374.87	1.02
397	196.2602	67.9846	374.50	0.82
398	197.1978	68.4837	374.12	0.59
399	198.1336	68.9859	373.75	0.33
400	199.0677	69.4913	373.37	0.01
401	200.0000	70.0000	373.09	-0.40
402	200.0000	70.0000	373.09	-0.40
403	200.9348	70.4780	373.00	-0.63
404	201.8712	70.9527	373.00	-0.73
405	202.8095	71.4238	373.00	-0.87
406	203.7494	71.8916	373.00	-1.00
407	204.6910	72.3559	373.00	-1.13
408	205.6344	72.8167	373.00	-1.26
409	206.5794	73.2741	373.00	-1.37
410	207.5261	73.7280	373.00	-1.48
411	208.4744	74.1785	373.00	-1.58
412	209.4244	74.6255	373.00	-1.68
413	210.3760	75.0690	373.00	-1.77
414	211.3293	75.5090	373.00	-1.85
415	212.2841	75.9455	373.00	-1.93
416	213.2405	76.3785	373.00	-2.01
417	214.1986	76.8080	373.00	-2.07
418	215.1581	77.2340	373.00	-2.13
419	216.1193	77.6565	373.00	-2.19
420	217.0819	78.0754	373.00	-2.24
421	218.0461	78.4908	373.00	-2.29
422	219.0119	78.9027	373.00	-2.34
423	219.9791	79.3111	373.00	-2.38
424	220.9478	79.7159	373.00	-2.41
425	221.9180	80.1172	373.00	-2.45
426	222.8896	80.5149	373.00	-2.48
427	223.8627	80.9090	373.00	-2.50
428	224.8372	81.2996	373.00	-2.52
429	225.8132	81.6866	373.00	-2.54
430	226.7905	82.0700	373.00	-2.56
431	227.7693	82.4499	373.00	-2.58

432	228.7495	82.8261	373.00	-2.59
433	229.7310	83.1988	373.00	-2.60
434	230.7139	83.5679	373.00	-2.61
435	231.6981	83.9333	373.00	-2.61
436	232.6836	84.2952	373.00	-2.62
437	233.6705	84.6534	373.00	-2.62
438	234.6587	85.0081	373.00	-2.62
439	235.6482	85.3591	373.00	-2.62
440	236.6389	85.7065	373.00	-2.62
441	237.6309	86.0502	373.00	-2.61
442	238.6242	86.3903	373.00	-2.61
443	239.6187	86.7268	373.00	-2.60
444	240.6145	87.0597	373.00	-2.60
445	241.6114	87.3888	373.00	-2.59
446	242.6095	87.7144	373.00	-2.58
447	243.6089	88.0363	373.00	-2.57
448	244.6094	88.3545	373.00	-2.56
449	245.6110	88.6690	373.00	-2.55
450	246.6138	88.9799	373.00	-2.53
451	247.6178	89.2871	373.00	-2.52
452	248.6228	89.5906	373.00	-2.51
453	249.6290	89.8904	373.00	-2.50
454	250.6362	90.1866	373.00	-2.48
455	251.6446	90.4791	373.00	-2.47
456	252.6540	90.7678	373.00	-2.45
457	253.6644	91.0529	373.00	-2.44
458	254.6759	91.3343	373.00	-2.42
459	255.6884	91.6119	373.00	-2.41
460	256.7019	91.8859	373.00	-2.39
461	257.7164	92.1561	373.00	-2.38
462	258.7319	92.4227	373.00	-2.36
463	259.7484	92.6855	373.00	-2.34
464	260.7658	92.9445	373.00	-2.32
465	261.7842	93.1999	373.00	-2.31
466	262.8034	93.4515	373.00	-2.29
467	263.8237	93.6994	373.00	-2.27
468	264.8448	93.9435	373.00	-2.26
469	265.8668	94.1839	373.00	-2.24
470	266.8896	94.4206	373.00	-2.22
471	267.9133	94.6535	373.00	-2.20
472	268.9379	94.8827	373.00	-2.18
473	269.9633	95.1081	373.00	-2.16
474	270.9895	95.3297	373.00	-2.14
475	272.0166	95.5476	373.00	-2.11
476	273.0444	95.7617	373.00	-2.09
477	274.0730	95.9721	373.00	-2.07
478	275.1024	96.1787	373.00	-2.04
479	276.1325	96.3815	373.00	-2.02
480	277.1633	96.5806	373.00	-1.99
481	278.1949	96.7758	373.00	-1.97

482	279.2272	96.9673	373.00	-1.94
483	280.2601	97.1550	373.00	-1.91
484	281.2938	97.3390	373.00	-1.87
485	282.3281	97.5191	373.00	-1.84
486	283.3630	97.6955	373.00	-1.81
487	284.3987	97.8680	373.00	-1.78
488	285.4349	98.0368	373.00	-1.75
489	286.4718	98.2018	373.00	-1.72
490	287.5092	98.3629	373.00	-1.70
491	288.5472	98.5203	373.00	-1.68
492	289.5858	98.6739	373.00	-1.68
493	290.6249	98.8236	373.00	-1.66
494	291.6647	98.9696	373.00	-1.60
495	292.7049	99.1117	373.00	-1.55
496	293.7456	99.2501	373.00	-1.51
497	294.7868	99.3846	373.00	-1.43
498	295.8286	99.5153	373.00	-1.39
499	296.8707	99.6422	373.00	-1.29
500	297.9134	99.7653	373.00	-1.29

Figure 1 Heat transfer coefficient and maximum velocity profile at the different BUR (single lip air ring used)

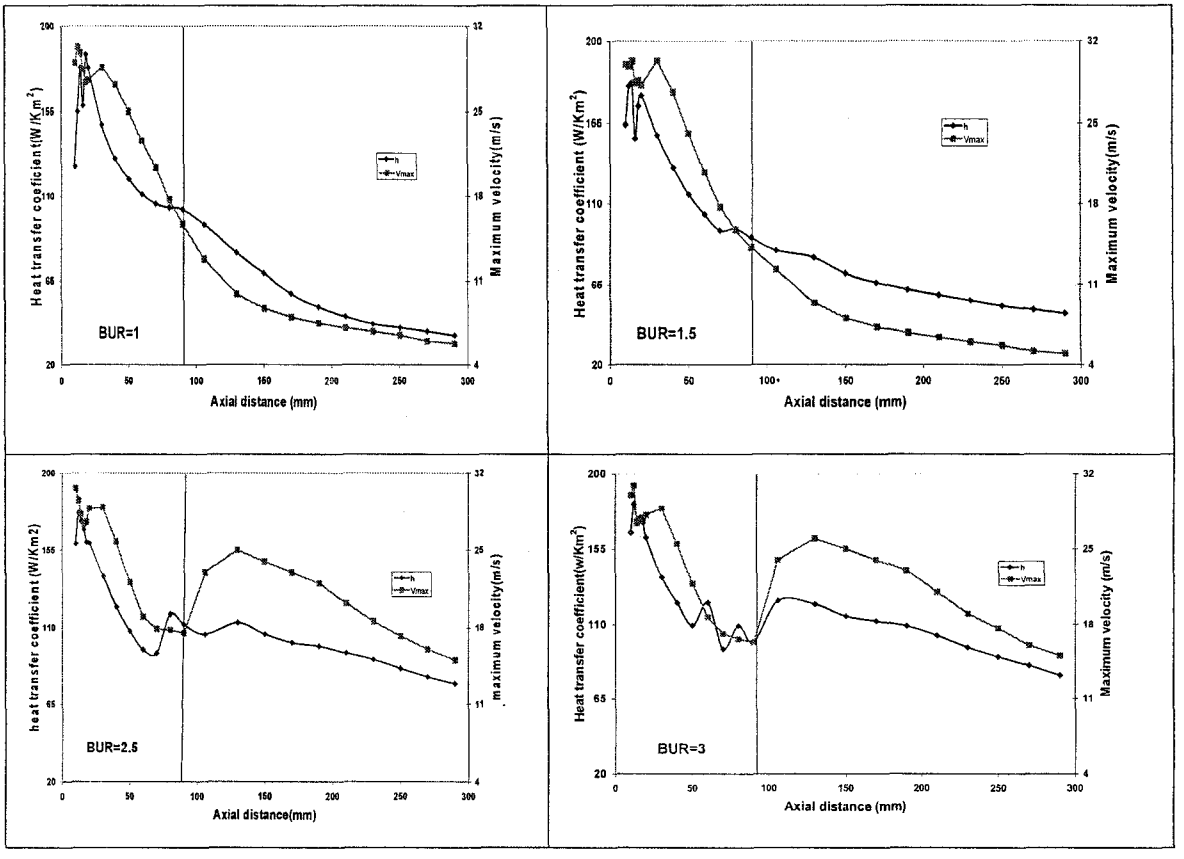

Figure2. Bubble radius variation and corresponding inside the pressure profile at the different bubble stable state (BUR=1)

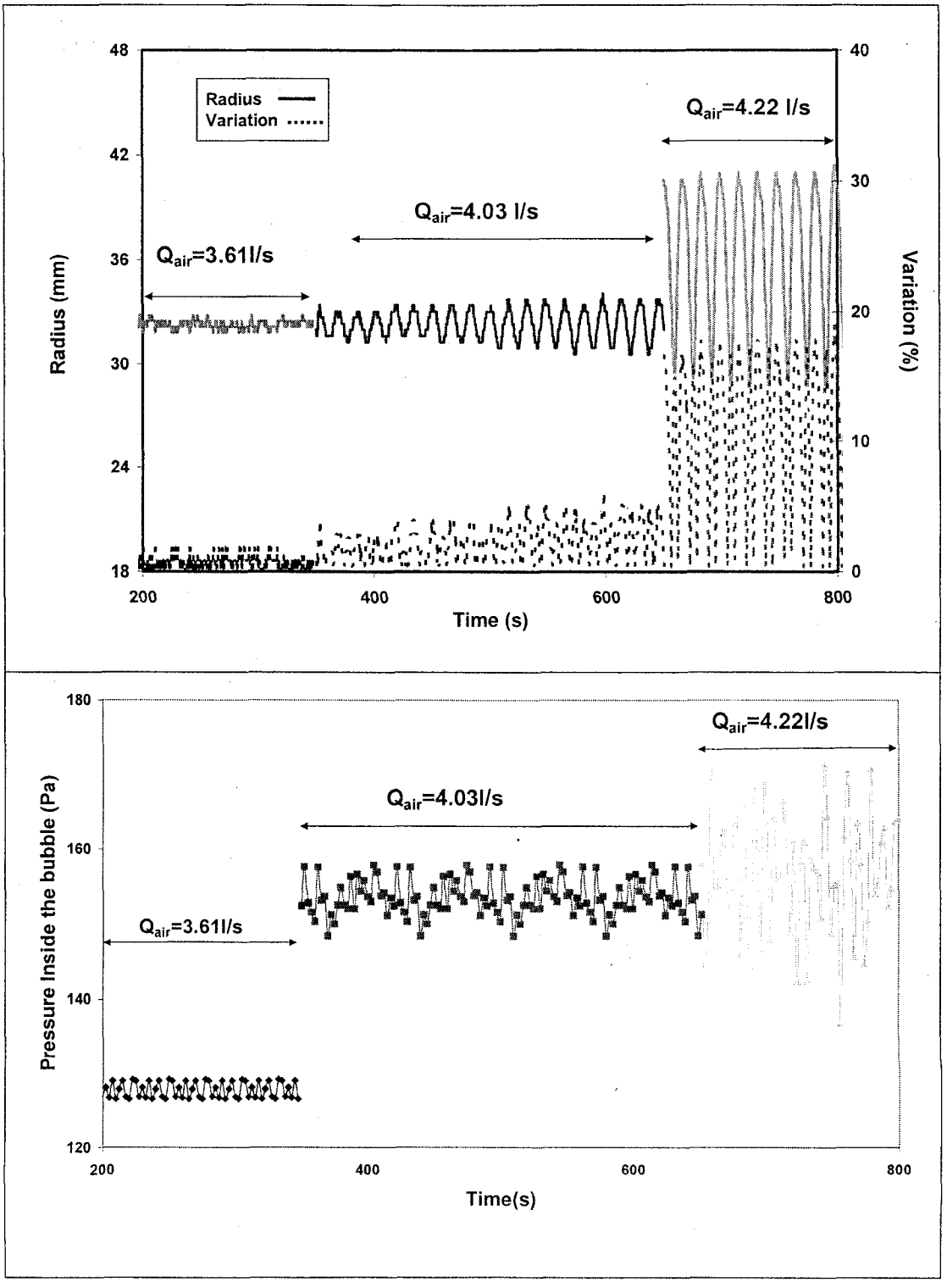

Figure3 Bubble radius variation and corresponding inside the pressure profile at the different bubble stable state (BUR=2)